



VNIVERSITAT
D VALÈNCIA

1

2 **Search for associated production of a Higgs**
3 **boson and a single top quark in $2l + \tau_{had}$**
4 **final state using proton-proton collisions**
5 **at $\sqrt{s} = 13$ TeV with the ATLAS detector**

6

PhD Thesis

7

Pablo Martínez Agulló

8

IFIC - CSIC/Universitat de València
Departament de Física Atòmica, Molecular i Nuclear
Programa de Doctorat en Física

9

10

Under the supervision of

11

Carlos Escobar Ibáñez
and
Susana Cabrera Urbán

12

13

14

15

València, 14 de Marzo

¹⁶ **Carlos Escobar Ibáñez,**
¹⁷ investigador científico del Consejo Superior de Investigaciones Científicas, y
¹⁸

¹⁹ **Susana Cabrera Urbán,**
²⁰ científica titular del Consejo Superior de Investigaciones Científicas,

²¹ **Certifican:**

²² Que la presente memoria, **Search for associated production of a**
Higgs boson and a single top quark in $2l + \tau_{had}$ final state
using proton-proton collisions at $\sqrt{s} = 13$ TeV with the ATLAS
detector, ha sido realizada bajo su dirección en el Instituto de Física
Corpuscular, centro mixto de la Universitat de València y del CSIC, por
Pablo Martínez Agulló, y constituye su Tesis para optar al grado de
Doctor en Física.

²⁹ Y para que así conste, en cumplimiento de la legislación vigente, presenta
³⁰ en el Departamento de Física Atómica, Molecular y Nuclear de la Univer-
³¹ sidad de Valencia la referida Tesis Doctoral, y firman el presente certificado.

³²

³³ València, a DD de MES de 2022,

³⁴

³⁵ Carlos Escobar Ibáñez

Susana Cabrera Urbán

³⁶ Abbreviations

³⁷

Acronym	Meaning
AD	Antiproton Decelerator
ALICE	A Large Ion Collider Experiment
ATLAS	A Toroidal LArge AparatuS
AWAKE	Advanced Proton Driven Plasma Wakefield Acceleration Experiment
CERN	European Organization for Nuclear Research
CMS	Compact Muon Solenoid
CP	Charge conjugation Parity
CSC	Cathode-Strip Chambers
DAQ	Data Acquisition
ECAL	Electromagnetic Calorimeter
EF	Event Filter
EM	Electromagnetic
EW	Electro Weak
EWSB	Electroweak Symmetry Breaking
FASER	ForwArd Search ExpeRiment
FCAL	Forward calorimeter
FTK	Fast TracKer
GR	General Relativity
HCAL	Hadronic Calorimeter
HLT	High Level Trigger
IBL	Insertable B-Layer
IP	Interaction Point

Acronym	Meaning
IR	Insertion Regions
ISOLDE	On-Line Isotope Mass Separator
ITk	Inner Tracker
LAr	Liquid Argon
LCG	LHC Computing Grid
LEIR	Low Energy Ion Ring
LEP	Large Electron-Positron
LHC	Large Hadron Collider
LHCb	The Large Hadron Collider Beauty
LHCf	Large Hadron Collider forward
LINAC2	Linear Accelerator 2
LINAC3	Linear Accelerator 3
LINAC4	Linear Accelerator 4
LO	Leading Order
LVL1	Level-1 Trigger
LVL2	Level-2 Trigger
MATHUSLA	Massive Timing Hodoscope for Ultra Stable neutrAL pArticles
MDT	Monitored Drift Tube
MoEDAL	Monopole and exotic particle detector at the LHC
MS	Muon Spectrometer
NLO	Next-to-Leading Order
NNLO	Next-to-Next-to-Leading Order
PDF	Parton Distribution Function
PS	Proton Synchrotron
PSB	Proton Synchrotron Booster
QCD	Quantum Chromodynamics
QED	Quantum Electrodynamics
QFT	Quantum Field Theory

Acronym	Meaning
RF	Radio Frequency
ROD	ReadOut Drivers
RoI	Regions of interest
ROS	ReadOut Systems
RPC	Resistive Plate Chambers
SCT	Semiconductor Tracker
SFO	Sub-Farm Output
SM	Standar Model
SPS	Super Proton Synchrotron
SSB	Spontaneus Symmetry Breakin
SSC	Superconducting Super Collider
SUSY	Supersimmetry
TGC	Thin Gap Chambers
TI	Transfer Injection

⁴⁰ Preface

⁴¹ **VERSIÓN 14_Marzo**

⁴² **Carlos, Susana**

⁴³ **Como veis, el capítulo 1 aún no está terminado pero ya se puede**
⁴⁴ **empezar a leer y corregir. Hay subsecciones terminadas, otras con**
⁴⁵ **el "Work in Progress" y alguna sin nada prácticamente.**

⁴⁶ The Standard Model of particle physics is both incredibly successful and
⁴⁷ glaringly incomplete. Among the questions left open is the striking imbalance
⁴⁸ of matter and antimatter in our universe, which inspires experiments to
⁴⁹ compare the fundamental properties of matter/antimatter conjugates with
⁵⁰ high precision.

⁵¹ The discovery of a Higgs boson by the ATLAS and CMS experiments in
⁵² 2012 opened a new field for exploration in the realm of particle physics.

- ⁵³ - ttbar sensitive to the yt module
⁵⁴ - th sesntive to the sign

⁵⁵ **Poner algo bonito del top y el Higgs**

⁵⁶ The top quark is the heaviest elementary particle discovered so far, with
⁵⁷ a mass of $m_{top} = 172.76 \pm 0.30$ GeV [1], followed by the Higgs boson, with
⁵⁸ $m_H = 125.25 \pm 0.17$ GeV [2].

⁵⁹ This thesis describes the search for the associated production of a Higgs
⁶⁰ boson and a single top quark (tHq) in the final state with three leptons,
⁶¹ being two of them light leptons (e/μ) and the other one a hadronically-
⁶² decaying tau quark (τ_{had}). This analysis uses an integrated luminosity of
⁶³ 139 fb^{-1} of proton-proton collision data at centre-of-mass energy of 13 TeV
⁶⁴ collected by ATLAS during LHC Run 2. The ATLAS detector is one of
⁶⁵ the four detectors at the Large Hadron Collider (LHC) of the European
⁶⁶ Organization for Nuclear Research (CERN).

⁶⁷ This analysis presents a great challenge due to the extremely small cross
⁶⁸ section of the tHq processes (**cita**) in general and for the two light-leptons
⁶⁹ plus one hadronic tau ($2\ell + 1\tau_{had}$) in particular (**usar los estudios del**

70 **truth para ver qué fracción de los eventos de tH son $2\ell + 1\tau_{\text{had}}$)**
71 The possible observation of a an excess of signal events with respect to the
72 Standard Model predictions, would be a clear evidence of new physics in
73 terms of \mathcal{CP} -violating Yukawa couplings between the top quark and the
74 Higgs boson.

75 For these studies three Higgs decay channels are explored: $H \rightarrow \tau\tau$,
76 $H \rightarrow WW$ and $H \rightarrow ZZ$.

77 Multivariate techniques are used to discriminate the signal from the
78 dominant backgrounds as well as to reconstruct the events.

79 Furthermore, other channels (defined by their final state) are being stud-
80 ied in the context of tHq research

81 During this thesis the “god-given” units are used. In this system (name
82 natural system) the Planck constant and the speed of light have the same
83 magnitude and dimensions ($\hbar = c = 1$), implying that:

84 $[\text{length}] = [\text{time}] = [\text{energy}]^{-1} = [\text{mass}]^{-1}$.

85 In the international system (SI) units, the values are $\hbar = 1.055 \times 10^{-34}$ Js
86 and $c = 2.998 \times 10^8$ m/s. An exception is made for the Chapter 2, where
87 the SI is used for describing the design of the LHC and ATLAS.

88 **Conceptos triviales que también debería introducir en**
89 **algún momento [http://opendata.atlas.cern/books/current/
90 get-started/_book/GLOSSARY.html](http://opendata.atlas.cern/books/current/get-started/_book/GLOSSARY.html)**

⁹¹ Acknowledgements

⁹² This work would not have been possible without the invaluable help of a
⁹³ large number of people, whom I have been fortunate to meet, and to whom
⁹⁴ I would like to thank and dedicate this thesis.

⁹⁵ Gracias gracias

⁹⁶ Contents

⁹⁷	Abbreviations	iv
⁹⁸	Preface	vii
⁹⁹	Acknowledgements	ix
¹⁰⁰	Contents	1
¹⁰¹	1 Theoretical Framework	1
¹⁰²	1.1 The Standard Model of particle physics	1
¹⁰³	1.1.1 Introduction to the SM and its elementary particles .	2
¹⁰⁴	1.1.2 Quantum electrodynamics	6
¹⁰⁵	1.1.3 Electroweak interactions	9
¹⁰⁶	1.1.3.1 Weak interactions and Symmetries	9
¹⁰⁷	1.1.3.2 Electroweak unification	12
¹⁰⁸	1.1.4 Quantum chromodynamics	15
¹⁰⁹	1.1.4.1 Quarks and colour	15
¹¹⁰	1.1.4.2 Gauge invariance for $SU(3)$	16
¹¹¹	1.1.5 Particle masses	19
¹¹²	1.1.5.1 The Higgs mechanism	20
¹¹³	1.1.6 Charge-Parity	26
¹¹⁴	1.1.7 Problems with the Standard Model	26
¹¹⁵	1.2 Top quark	30

116	1.2.1	Top quark discovery	30
117	1.2.2	Top quark production at LHC	32
118	1.2.2.1	Top pairs	32
119	1.2.2.2	Single top	34
120	1.2.3	Top quark decay	37
121	1.2.4	Top quark polarisation	39
122	1.2.5	Top quark physics	39
123	1.3	Higgs boson	39
124	1.3.1	Higgs production and decay at LHC	40
125	1.3.2	Higgs boson discovery	41
126	1.3.3	Higgs boson physics	43
127	1.4	Top quark and Higgs boson interplay	43
128	1.4.1	$t\bar{t}H$	44
129	1.4.1.1	$t\bar{t}H$ Standard Model	45
130	1.4.1.2	$t\bar{t}H$ Charge-Parity	45
131	1.4.2	tH	45
132	1.4.2.1	tH Standard Model	47
133	1.4.2.2	tH Charge-Parity	47
134	1.4.2.3	ATLAS and CMS results	47
135	2	The ATLAS experiment at the Large Hadron Collider of CERN laboratory	49
136	2.1	CERN	49
137	2.2	Large Hadron Collider	51
138	2.2.1	Machine design	51
139	2.2.2	Accelerator complex	55
140	2.2.3	LHC Experiments	56
141	2.2.4	LHC Computing grid	59
142	2.2.5	Energy, Luminosity and Cross section	61
143	2.2.6	The Pile-up effect	66

145	2.2.7 Phenomenology of proton-proton collisions	67
146	2.2.7.1 Proton structure	68
147	2.3 ATLAS	69
148	2.3.1 Objective and physics programme	72
149	2.3.2 Coordinate system	72
150	2.3.3 Inner Detector	74
151	2.3.3.1 Insertable B-Layer	75
152	2.3.3.2 Pixel Detector	76
153	2.3.3.3 Semiconductor Tracker	76
154	2.3.3.4 Transition Radiation Tracker	77
155	2.3.4 Calorimeters	78
156	2.3.4.1 Particle showering	79
157	2.3.4.2 Electric calorimeter	81
158	2.3.4.3 Hadronic calorimeter	81
159	2.3.4.4 Forward calorimeter	82
160	2.3.5 Muon Spectrometer	83
161	2.3.6 Magnet system	85
162	2.3.6.1 Central solenoid magnet	86
163	2.3.6.2 Toroid magnets	86
164	2.3.7 Trigger and Data Acquisition System	88
165	2.3.8 Computing resources	89
166	2.3.9 ATLAS upgrade towards HL-LHC	89
167	2.3.9.1 Performance	94
168	2.3.9.2 Challenges	94
169	2.4 Alignment of the inner detector	94
170	2.4.1 Alignment requirements	94
171	2.4.1.1 Local coordinate frame	94
172	2.4.1.2 Track parameters	94
173	2.4.1.3 Residuals	94

174	2.4.2	Track based alignment	94
175	2.4.2.1	Global χ^2 algorithm	94
176	2.4.2.2	Weak modes	94
177	2.4.2.3	Alignment levels and degrees of freedom	94
178	2.4.3	Alignment results during Run-2	94
179	2.4.4	Alignment towards Run-3	94
180	2.4.4.1	Pseudo-real-time-online monitoring	94
181	3	Data and simulated events and object reconstruction	95
182	3.1	Data	95
183	3.2	Monte Carlo	95
184	3.2.1	MC simulations	96
185	3.2.1.1	Parton shower simulation	96
186	3.2.1.2	Hadronisation simulation	96
187	3.2.1.3	Underlaying decay simulation	96
188	3.2.1.4	Hadron decay simulation	96
189	3.2.1.5	Pile-up simulation	96
190	3.2.2	MC generators	96
191	3.3	Object reconstruction and identification	96
192	3.3.1	Tracking	96
193	3.3.2	Vertices	97
194	3.3.3	Electrons and photons	97
195	3.3.4	Muons	97
196	3.3.5	Jets	97
197	3.3.6	Bottom quark induced jets	97
198	3.3.7	Missing transverse energy	97
199	3.3.8	Overlap removal	97
200	4	Probing the top-quark polarisation in the single-top t-channel production	99

202	4.1	Introduction	99
203	4.2	Top quark polarisation observables	100
204	4.3	Simulated event samples	100
205	4.4	Object reconstruction	100
206	4.5	Trigger requirements and event preselection	100
207	5	Search for rare associate tHq production	101
208	5.1	Introduction	101
209	5.2	Data and simulated events	101
210	5.3	Object definition and reconstruction	102
211	5.4	Signal	102
212	5.4.1	Signal generation and validation	102
213	5.4.2	Parton-level truth validation	102
214	5.4.3	Lepton assignment	102
215	5.5	Background estimation	102
216	5.5.1	Fakes estimation	102
217	5.5.2	Prompt backgrounds	104
218	5.6	Event selection	104
219	5.6.1	Preselection	104
220	5.6.2	BDT	104
221	5.6.2.1	Performance	104
222	5.6.2.2	Ranking of variables	104
223	5.6.2.3	Hyperparameter optimisation	104
224	5.6.2.4	Negative-weights strategy	104
225	5.6.2.5	k-Folding	104
226	5.6.3	Signal Region	104
227	5.6.4	Control Region	104
228	5.7	Systematic uncertainties	104
229	5.7.1	Theoretical uncertainties	106

230	5.7.2 Modelling uncertainties	106
231	5.7.3 Experimental uncertainties	106
232	5.8 Fit results	106
233	5.8.1 Strategy	106
234	5.8.2 Fit with Asimov data	106
235	5.8.2.1 Post-fit	106
236	5.8.2.2 Pruning	106
237	5.8.2.3 Nuisance Parameters	106
238	5.8.2.4 Correlation matrix	106
239	5.8.2.5 Ranking	106
240	5.8.3 Fit to data	106
241	5.8.3.1 Post-fit	106
242	5.8.3.2 Pruning	106
243	5.8.3.3 Nuisance Parameters	106
244	5.8.3.4 Correlation matrix	106
245	5.8.3.5 Ranking	106
246	5.8.4 Results	106
247	5.8.5 Data fit	106
248	5.9 Combination results	106
249	5.10 Conclusions	107
250	6 Conclusion	109
251	Bibliography	111
252	Summary of the results	125
253	Resum de la tesi	127
254	1 Marc teòric	127
255	1.1 El Model Estàndard	127
256	1.2 La física del quark top	127

257	1.3	La física del bosó de Higgs	127
258	2	L'experiment ATLAS del LHC al CERN	127
259	2.1	El gran col·lisionador d'hadrons	127
260	2.2	El detector ATLAS	127
261	3	Mesura de la polarització del quark top al canal- <i>t</i>	127
262	3.1	Selecció d'esdeveniments	128
263	3.2	Estimació del fons	128
264	3.3	Fonts d'incertesa	128
265	3.4	Resultats	128
266	4	Recerca de processos <i>tH</i> amb un estat final $2\ell + 1\tau_{\text{had}}$	128
267	4.1	Selecció d'esdeveniments	128
268	4.2	Estimació del fons	128
269	4.3	Fonts d'incertesa	128
270	4.4	Resultats	128
271	5	Conclusions	128

²⁷² **Chapter 1**

²⁷³ **Theoretical Framework**

²⁷⁴ **1.1 The Standard Model of particle physics**

²⁷⁵ Since the very first moment of our history, the humankind has pursued
²⁷⁶ the knowledge of nature, has tried to understand and describe how the
²⁷⁷ universe works at a fundamental level. In fact, the word physics comes
²⁷⁸ from the Greek “*φυσική*” which means “nature” [3][4]. Most of the enquires
²⁷⁹ regarding this, can be boiled down to two basic questions: What are the
²⁸⁰ ultimate building blocks of reality? and which are the rules that govern
²⁸¹ them?

²⁸² In the 7th century BCE, the pre-Socratic philosopher Thales of Miletus
²⁸³ already proclaimed that every event had a natural cause [5]. Later, to un-
²⁸⁴ derstand how the basic components of the matter were formed, the ancient
²⁸⁵ Indian philosophers such as Kanada and Dignaga on the 6th century BCE
²⁸⁶ and Greeks Democritus and Leucippus on the 5th century BCE, developed
²⁸⁷ the atomism, which comes from “*ατομον*” meaning uncuttable or indivisible
²⁸⁸ [6][7].

²⁸⁹ From then to our days, the search for the minute fragments that comprise
²⁹⁰ the matter and its interactions has led us to the Standard Model (SM) of
²⁹¹ particle physics, one of the most successful scientific theories cultivated
²⁹² so far. This understanding of the universe can explain phenomena from
²⁹³ behaviour of atoms to how stars burn.

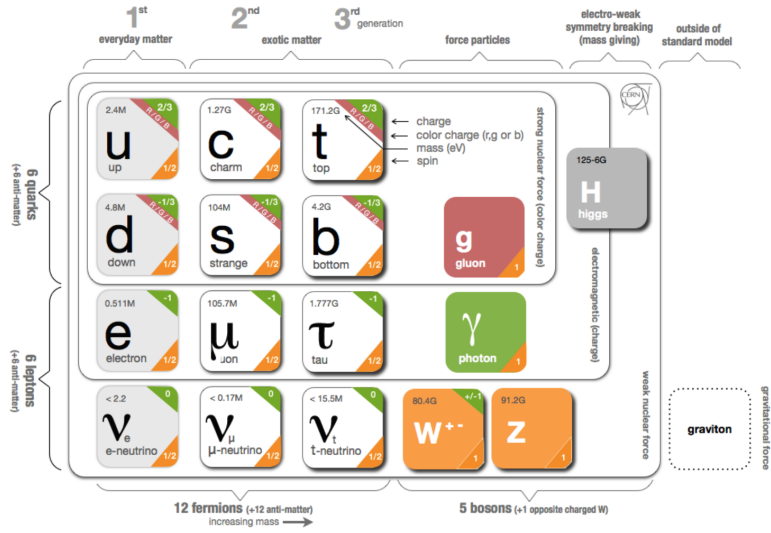


Figure 1.1: Fundamental particles of the Standard Model.

294 1.1.1 Introduction to the SM and its elementary 295 particles

296 Based on Quantum Field Theory (QFT), the SM of particle physics
297 provides the theoretical framework that constitutes what is currently ac-
298 cepted as the best description of particles physics. It aims to explain both
299 all particles of matter and their interactions. The completion of the SM
300 was a collaborative effort of several scientists during the second half of the
301 20th, being the current formulation finalised in the decade of 1970. A rep-
302 resentation of the fundamental particles, i. e. particles that are not made
303 of anything else, that compose the SM is presented in Figure 1.1. Most of
304 these particles are unstable and decay to lighter particles within fractions
305 of a second. As the scheme in Figure 1.1 indicates, the 12 fermions have
306 their corresponding 12 anti-fermions and the quarks and gluons carry colour
307 charge.

308 The SM is a gauge theory based on the symmetry group
309 $SU(3)_C \otimes SU(2)_L \otimes U(1)_Y$, which describes all fundamental interactions
310 except from the gravitational force¹. This theory provides an explana-
311 tion to strong, weak and electromagnetic interactions via the exchange of
312 the corresponding vector² bosons (spin-1 gauge fields). The mediation for
313 the electromagnetic interaction (explicated in 1.1.2) is done by one mass-
314 less photon (γ), this force is invariant under the $U(1)$ symmetry group.

¹The gravitational interaction is described by Einstein's General Relativity (GR) [8].

²“Vector bosons” refer to all bosons that have spin 1 in contrast to the “scalar boson’s” which have spin 0.

Interaction	Theory	Mediator	Relative strength	Range (m)
Strong	QCD	g	1	10^{-15}
Electromagnetic	QED/EW	γ	$1/137$	∞
Weak	EW	W^\pm, Z	10^{-6}	10^{18}
Gravitational	GR	-	6×10^{-39}	∞

Table 1.1: Typical strength of the fundamental interactions with respect to the strong interaction. Here the strength is understood as the coupling constant. In GR the gravitational interaction is not a force but the effect of the four-dimensional spacetime curvature and, hence, it has no mediator in this formalism.

315 While for the weak interactions, guided by $SU(2)$, three massive bosons,
 316 W^+ , W^- and Z , act as mediators ($m_{W^\pm} = 80.385 \pm 0.015$ GeV and
 317 $m_Z = 91.1876 \pm 0.02$ GeV). Although the electromagnetic and weak in-
 318 teractions seem completely different at low energies, they are two aspects of
 319 the same force and can be described simultaneously by the $SU(2)_L \otimes U(1)_Y$
 320 symmetry group, which represents the so called Electro-Weak (EW) sector
 321 (detailed in Section 1.1.3). The strong force, with its 8 massless gluons
 322 (g), is described by the $SU(3)_C$ colour group (see Section 1.1.4). All these
 323 interactions differ in their magnitude, range and the physical phenomena
 324 that describe. These features are summarised in Table 1.1, where not only
 325 the interactions of the SM are included but the gravitation is as well.

326 Apart from the vector bosons, there is one massive scalar boson, the
 327 Higgs boson ($m_H = 125.25 \pm 0.17$ GeV). Through the interaction with this
 328 particle, all massive particles of Figure 1.1 gain their mass via the EW
 329 spontaneous symmetry breaking. This mechanism is described in Section
 330 1.1.5.1.

331 Before describing the fundamental interactions of the SM in the QFT
 332 formalism, let's introduce the main two types of particles according to their
 333 spin, i.e. intrinsic angular momentum: fermions and bosons.

334 **Fermions**

335 The fermions are the particles that follow the Fermi-Dirac statistics, i.e.
 336 obey the Pauli exclusion principle [9], resulting in a distribution of particles
 337 over energy levels in which two elements with the same quantum numbers
 338 cannot occupy the same states. The fermions include all particles with half-
 339 integer spin: quarks, leptons and baryons. A baryon is a non-fundamental

340 particle composed of an odd number of valence quarks³ (consequently having
 341 half-integer spin) and nearly all matter that may be encountered or
 342 experienced in everyday life is baryonic matter. Some examples of baryons
 343 are⁴ the proton ($u u d$), the neutron ($d d u$), Λ ($u d s$), Λ_c^+ ($u d c$) and Σ^+
 344 ($u u s$). Apart from the 3-quark baryons, an exotic pentaquark state has
 345 been observed at LHCb experiment of the LHC [10].

346 The fundamental fermionic matter (Table 1.2) is organised in the three
 347 families of leptons and quarks:

$$348 \quad \begin{bmatrix} \nu_e & u \\ e^- & d \end{bmatrix}, \begin{bmatrix} \nu_\mu & c \\ \mu^- & s \end{bmatrix}, \begin{bmatrix} \nu_\tau & t \\ \tau^- & b \end{bmatrix}$$

349 .

350 These three generations, which are defined as the columns in Figure 1.1,
 351 exhibit the same kind of gauge interactions and they only differ in their
 352 mass [11]. According to the EW symmetry, each family can be classified as:

$$353 \quad \begin{bmatrix} \nu_\ell & q_u \\ \ell^- & q_d \end{bmatrix} \equiv \begin{pmatrix} \nu_\ell \\ \ell^- \end{pmatrix}_L, \begin{pmatrix} q_u \\ q_d \end{pmatrix}_L, \ell^-_R, q_{uR}, q_{dR}$$

354 (plus the corresponding antiparticles) where the subindices L and R stand
 355 from left and right handed particles respectively. This structure responds to
 356 the fact that left-handed particles convert different than right-handed ones
 357 under $SU(2)$ transformations. The left-handed fields are $SU(2)_L$ doublets
 358 and the right-handed ones $SU(2)_R$ singlets. This difference is explained
 359 with more detail in Section 1.1.3.

360 The fundamental representation of $SU(3)$ is a triplet, this is why each
 361 quark can appear in three different colours, whereas each antiquark can
 362 exhibit one of the corresponding “anticolours”.

363 The SM fermions properties are summarised in Table 1.2. As can be seen
 364 in its last rows, the neutrino flavour states do no correspond to the mass
 365 states (ν_1, ν_2, ν_3). What happens is that each flavour state is a quantum
 366 mechanical combination of neutrinos of different masses and viceversa. More
 367 details about the neutrino masses can be found in a dedicated text in Section
 368 1.1.7

³The hadrons (baryons are mesons) are understood as a sea of partons being the valence quarks those which are more probable to be found in the hadron according to the parton distribution functions.

⁴Between round brackets, the valence quarks are shown.

Family	Name	Mass	Q
Quarks	Up (u)	$2.16^{+0.49}_{-0.26}$ MeV	$2/3$
	Down (d)	$4.67^{+0.48}_{-0.17}$ MeV	$-1/3$
	Charm (c)	1.27 ± 0.02 GeV	$2/3$
	Strange (s)	93^{+11}_{-5} MeV	$-1/3$
	Top (t)	172.76 ± 0.30 GeV	$2/3$
	Bottom (b)	$4.18^{+0.03}_{-0.02}$ GeV	$-1/3$
Leptons	Electron (e^-)	$0.5109989461 \pm 0.0000000031$ MeV	-1
	Muon (μ)	$105.6583745 \pm 0.0000024$ MeV	-1
	Tau (τ)	776.86 ± 0.12 MeV	-1
	Electron neutrino (ν_e)	ν_e, ν_μ, ν_τ	0
	Muon neutrino (ν_μ)	\neq	0
	Tau neutrino (ν_τ)	ν_1, ν_2, ν_3	0

Table 1.2: Properties of the quarks and leptons. The electric charge is represented here by Q. The ν_1, ν_2, ν_3 are the neutrino mass eigenstates.

369 The fundamental fermions are usually understood as the fundamental
 370 building blocks of matter. However, while the building blocks are important,
 371 there is a point that also has to be taken into account, the force. Without
 372 force these fermions would not interact with each other. The particles that
 373 mediate these interactions are the gauge bosons.

374 **Bosons**

375 Bosons differ from fermions by obeying the Bose-Einstein statistics, thus,
 376 bosons are not limited to single occupancy for a determined state. In other
 377 words, the Pauli exclusion principle is not applied. All particles with integer
 378 spin are bosons; from the particles shown on the right columns of Figure 1.1
 379 to the mesons. Mesons, along with baryons, are part of the hadron family,
 380 i.e. particles composed of quarks (see Section 1.1.4). The particularity
 381 of mesons is that they are formed from an equal number of quarks and
 382 antiquarks (usually one of each) bound together by strong interactions.
 383 Some examples of mesons are π^+ ($u \bar{d}$), π^0 ($\frac{u\bar{u}-d\bar{d}}{\sqrt{2}}$), K^+ ($u \bar{s}$) and J/ψ
 384 ($c \bar{c}$).

385 The elementary vector bosons are the force carriers and presented in
386 Table 1.1 while Higgs boson is a fundamental particle as well.

387 **Gauge Invariance**

388 Constituting one of the most successful theories of Physics, the SM is able
389 to provide an elegant mathematical framework to describe the experimental
390 physics results with great precision. Another key element to understand the
391 SM is the concept of gauge invariance. As it is illustrated during the rest of
392 the Section 1.1, by demanding that the Lagrangian remains invariant under
393 local gauge transformations, the existence of the SM force-carrier bosons
394 (γ , W^+ , W^- , Z and g).

395 **1.1.2 Quantum electrodynamics**

396 The gauge invariance refers to the invariance of a theory under trans-
397 formations which the theory is said to posses internal symmetry. The trans-
398 formations which are applied in all space-time locations simultaneously are
399 known as “global” transformations while the ones that vary from one point
400 to another are “local”. Each local symmetry is the basis of a gauge theory
401 and requires the introduction of its own gauge bosons as it is discussed in
402 the following pages.

In QFT, particles are described as excitations of quantum fields that satisfy the corresponding mechanical field equations. The Lagrangians in QFT are used analogous to those of classical mechanics, where the equation of motion can be derived from the Lagrangian density function (\mathcal{L}) and the Euler-Lagrange equations for fields:

$$\frac{\partial \mathcal{L}}{\partial \phi} - \partial_\mu \frac{\partial \mathcal{L}}{\partial (\partial_\mu \phi)} = 0$$

403 , where $\partial_\mu = \frac{\partial}{\partial x^\mu}$ denotes the partial derivatives with respect to the four-
404 vector x^μ and $\phi = \phi(\vec{x}, t)$ is the quantum field of a fermion or boson. The
405 Lagrangian density (or just Lagrangian, for simplicity) is used to express
406 the dynamics of the quantum field. In QFT, Noether’s theorem [12] relates
407 a symmetry in the \mathcal{L} to a conserved current.

408 The Dirac equation, $(i\gamma^\mu \partial_\mu - m)\Psi(x) = 0$, is one of the simplest relativ-
409 istic field equations. Its Lagrangian describes a free Dirac fermion:

$$\mathcal{L}_0 = i\bar{\Psi}(x)\gamma^\mu \partial_\mu \Psi(x) - m\bar{\Psi}(x)\Psi(x) \quad (1.1)$$

410 , being Ψ the wave function (spinor represented by four complex-valued
411 components) of the particle, γ^μ are the Dirac or gamma matrices,

⁴¹² $\{\gamma^0, \gamma^1, \gamma^2, \gamma^3\}$, m the mass of the fermion and $\bar{\Psi} = \Psi^\dagger \gamma^0$, the hermitic
⁴¹³ conjugate of the wave function. The gamma matrices build a set of ortho-
⁴¹⁴ gonal basis vectors for covariant vectors in a Minkowski space. The first
⁴¹⁵ term of \mathcal{L}_0 is the kinetic term while the second is the mass term.

This Lagrangian is invariant under $U(1)$ global transformations such as:

$$\Psi(x) \xrightarrow{U(1)} \Psi'(x) \equiv \exp\{iQ\theta\}\Psi(x) \quad (1.2)$$

⁴¹⁶ , where $Q\theta$ is a real constant. The phase of $\Psi(x)$ is a pure convention-
⁴¹⁷ dependent quantity without a physical meaning since the observables de-
⁴¹⁸ pend on $|\Psi(x)|^2$.

However, if θ was x dependent, the transformation 1.2 would be:

$$\Psi(x) \xrightarrow{U(1)} \Psi'(x) \equiv \exp\{iQ\theta(x)\}\Psi(x) \quad (1.3)$$

, which is not longer a global transformation but a local transformation instead. The transformation in 1.3 would not let the \mathcal{L}_0 in 1.1 invariant because the derivative in the kinetic term would go as:

$$\partial_\mu \Psi(x) \xrightarrow{U(1)} \exp\{iQ\theta\}(\partial_\mu + iQ\partial_\mu\theta)\Psi(x) \quad (1.4)$$

⁴¹⁹ .

The gauge principle is the requirement that the $U(1)$ phase invariance should hold locally. In order to do so, it is necessary to introduce an additional term to the Lagrangian so that when one applies $\Psi'(x) \equiv \exp\{iQ\theta(x)\}\Psi(x)$, the $\partial_\mu\theta$ term is canceled in 1.4. To achieve this invariance, a term with the vector gauge field A_μ is inserted. This field transforms as

$$A_\mu(x) \xrightarrow{U(1)} A'_\mu(x) \equiv A_\mu(x) + \frac{1}{e}\partial_\mu\theta \quad (1.5)$$

with a new covariant derivative:

$$D_\mu\Psi(x) \equiv [\partial_\mu + ieQA_\mu(x)]\Psi(x) \quad (1.6)$$

which transforms like the field:

$$D_\mu\Psi(x) \xrightarrow{U(1)} (D_\mu\Psi)'(x) \equiv \exp\{iQ\theta\}D_\mu\Psi(x)$$

⁴²⁰ .

The Lagrangian density can be defined by replacing the partial derivatives in \mathcal{L}_0 (1.1) by the covariant derivative in 1.6:

$$\begin{aligned} \mathcal{L}_{QED} &\equiv i\bar{\Psi}(x)\gamma^\mu D_\mu\Psi(x) - m\bar{\Psi}(x)\Psi(x) \\ &= i\bar{\Psi}(x)\gamma^\mu[\partial_\mu + ieQA_\mu(x)]\Psi(x) - m\bar{\Psi}(x)\Psi(x) \\ &= i\bar{\Psi}(x)\gamma^\mu\partial_\mu\Psi(x) - \bar{\Psi}(x)\gamma^\mu eQA_\mu\Psi(x) - m\bar{\Psi}(x)\Psi(x) \\ &= \mathcal{L}_0 - eQA_\mu\bar{\Psi}(x)\gamma^\mu\Psi(x) \end{aligned} \quad (1.7)$$

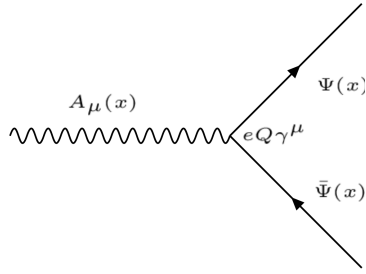


Figure 1.2: Three-point interaction vertex of QED.

421 .

422 The resulting Lagrangian is invariant under $U(1)$ local transformation.
 423 When the conversions 1.3 and 1.5 take place, the effects of the transformation
 424 are canceled out. Along with the original Lagrangian (\mathcal{L}_0), the \mathcal{L}_{QED}
 425 has an additional term describing the interaction between the fermion Ψ
 426 and the gauge field A_μ with a strength proportional to the charge eQ . This
 427 term, $eQA_\mu\bar{\Psi}\gamma^\mu\Psi$, that has been generated only by demanding the gauge
 428 invariance under $U(1)$, is not other than the vertex of Quantum Electro-
 429 dynamics (QED) (Figure 1.2).

This new A_μ term is the electromagnetic field and its quanta is the photon. A mass term containing $A^\mu A_\mu$ is forbidden because it would violate the $U(1)$ local invariance. In consequence, the mediator of the new A_μ field, the photon, is predicted to be a massless particle. To make A_μ a propagating field it is necessary to add the kinetic term of the field A_μ :

$$\mathcal{L}_{kin} \equiv -\frac{1}{4}F_{\mu\nu}(x)F^{\mu\nu}(x) \quad (1.8)$$

, where $F^{\mu\nu} \equiv \partial_\mu A_\nu - \partial_\nu A_\mu$. The kinetic term $F_{\mu\nu}F_{\mu\nu}F^{\mu\nu}$ is already invariant under local $U(1)$ phase transformations. From the QED Lagrangian in 1.7 and the kinetic term in 1.8, the Maxwell equations can be derived to describe electromagnetism, the infinite range⁵ interaction that occurs between particles with electrical charge. The \mathcal{L}_{QED} with this kinetic term is written as:

$$\mathcal{L}_{QED} = \bar{\Psi}(x)(i\gamma^\mu\partial_\mu - m)\Psi(x) - eQ\bar{\Psi}(x)\gamma^\mu A_\mu\Psi(x) - \frac{1}{4}F_{\mu\nu}(x)F^{\mu\nu}(x) \quad (1.9)$$

⁵Since the photon is (predicted to be) massless, the electromagnetic interaction has an infinite range.

430 **1.1.3 Electroweak interactions**

431 **1.1.3.1 Weak interactions and Symmetries**

432 The weak interaction is mediated by the W^+ , W^- and Z massive gauge
 433 bosons. Due their large mass ($m_{W^\pm} = 80.4$ GeV and $m_Z = 91.2$ GeV), the
 434 range of the interactions is restricted to $\sim 10^{-18}$ m. It is responsible for
 435 radioactive decays, nuclear fusions and flavour changing⁶ decays of fermions
 436 such as the decay of the muon ($\mu^- \rightarrow e^- \bar{\nu}_e \nu_\mu$).

437 Another particularity of this interaction is that it is the only interaction
 438 that violates several fundamental symmetries. There is a relation between
 439 symmetries and conservations laws which is known as Noether's theorem.
 440 Classical physics examples of how the symmetries leads to conserved quanti-
 441 ties are:

- 442 • Invariance under change of time \rightarrow Conservation of energy
- 443 • Invariance under translation in space \rightarrow Conservation of momentum
- 444 • Invariance under rotation \rightarrow Conservation of angular momentum

445 The three discrete symmetries that are fundamental for the SM formu-
 446 lation and are always hold for electromagnetic and strong interactions are:

- **Charge conjugation (\mathcal{C}):** Replace positive quantum charges by neg-
 ative charges and vice versa. It does not affect mass, energy, mo-
 mentum or spin. Essentially, it is a transformation that switches all
 particles with their corresponding antiparticles.

$$\mathcal{C}\Psi(\vec{r}, t) = \bar{\Psi}(\vec{r}, t)$$

- **Parity (\mathcal{P}):** Parity involves a transformation that changes the alge-
 braic sign of the spatial coordinate system. It does not reverse time,
 mass, energy or other scalar quantities.

$$\mathcal{P} : \begin{pmatrix} x \\ y \\ z \end{pmatrix} \rightarrow \begin{pmatrix} -x \\ -y \\ -z \end{pmatrix} \quad \mathcal{P}\Psi(\vec{r}, t) = \Psi(-\vec{r}, t)$$

- **Time reversal (\mathcal{T}):** Consists in flipping the sign of the time

$$\mathcal{T} : t \rightarrow -t \quad \mathcal{T}\Psi(\vec{r}, t) = \Psi(\vec{r}, -t)$$

⁶The leptonic charges are conserved.

The simultaneous combination of this three symmetries mentioned above results in the \mathcal{CPT} symmetry, a profound symmetry of QFT which is consistent through all experimental observations [13]. Meanwhile, the \mathcal{P} -symmetry and the \mathcal{C} -symmetry can be combined to create the \mathcal{CP} -symmetry, the product of the two transformations. The weak interaction violates \mathcal{P} and \mathcal{C} symmetries. It also violates the combined \mathcal{CP} -symmetry. Therefore, through the CPT theorem [14], if the \mathcal{CP} is violated, \mathcal{T} is violated as well to preserve the \mathcal{CPT} invariance [15].

455 Parity and Charge conjugation violation

456 Previously theorised by Lee and Yang [16], the confirmation of the non-
 457 conservation of \mathcal{P} in weak interactions arrived with the Wu experiment in
 458 1957 [17]. Studying the beta decay of the Cobalt-60, Wu and collaborators
 459 found that the neutrino and the antineutrino have the relative orientations
 460 of spin and linear momentum fixed. The neutrino spin is always opposite
 461 to the linear momentum, this is called left-handed particles. Meanwhile, for
 462 the antineutrinos, the momentum is always aligned in the same direction as
 463 the spin (right-handed particles). This causes the weak interactions which
 464 emit neutrinos or antineutrinos to violate the conservation of parity.

Only left-handed particles and right-handed antiparticles are sensitive to the weak force. Dirac fermion fields, ψ , exhibit chiral symmetry and the right and left handed chiral states can be expressed as:

$$\psi_L(x) = \frac{1}{2}(1 - \gamma_5)\psi(x) \equiv P_L\psi(x) \quad (1.10)$$

$$\psi_R(x) = \frac{1}{2}(1 + \gamma_5)\psi(x) \equiv P_R\psi(x) \quad (1.11)$$

with

$$\gamma^5 \equiv \gamma_5 \equiv \gamma^0\gamma^1\gamma^2\gamma^3 = \begin{pmatrix} 1 & 0 \\ 0 & 1 \end{pmatrix}$$

465 where P_L and P_R are known as projection operators. The last equality is
 466 valid in the Dirac representation.

467 In the same year, the \mathcal{C} violation was found too [18]. **Describe how**
 468 **the \mathcal{C} violation was discovered**

469 \mathcal{CP} violation

470 While \mathcal{P} and \mathcal{C} are violated in a maximal way by the weak interactions, the
 471 product of these two discrete transformations, \mathcal{CP} , is still a good symmetry
 472 (left-handed fermions \leftrightarrow right-handed fermions). Experiences such as the

473 Wu experiment respect the \mathcal{CP} symmetry and, in fact, in the \mathcal{CP} is a sym-
 474 metry of nealy all the observed phenomena. However, in 1964 Cronin and
 475 Fitch discovered a slight (2%) violation of the \mathcal{CP} symmetry in the decays
 476 of neutral kaons [19]. The \mathcal{CP} violation plays a fundamental role to explain
 477 the dominance of matter over antimatter in the present universe.

478 Direct \mathcal{CP} violation is allowed in the SM if a complex phase is present
 479 in the CKM matrix (described below) **Work in progress**

CKM matrix

The Cabibbo-Kobayashi-Maskawa (CKM) matrix describes the mixing between the three families or generations of quarks in the SM.

$$\begin{pmatrix} d' \\ s' \\ u' \end{pmatrix} = \begin{pmatrix} V_{ud} & V_{us} & V_{ub} \\ V_{cd} & V_{cs} & V_{cb} \\ V_{td} & V_{ts} & V_{tb} \end{pmatrix} = \begin{pmatrix} d \\ s \\ u \end{pmatrix} \quad (1.12)$$

480 It is a 3×3 unitary matrix described by four independent parameters:
 481 three angles (θ_{ij}) and one phase (δ_{13}). Different equivalent representations
 482 of the CKM matrix can be found in literature but the Particle Data Group
 483 recommends the standard CKM parameterisation:

$$V_{CKM} = \begin{pmatrix} c_{12}c_{13} & -s_{12}c_{13} & s_{13}e^{-i\delta_{13}} \\ -s_{12}c_{23} - c_{12}s_{23}s_{13}e^{i\delta_{13}} & -c_{12}c_{23} - s_{12}s_{23}s_{13}e^{i\delta_{13}} & s_{23}c_{13} \\ s_{12}s_{23} - c_{12}c_{23}s_{13}e^{i\delta_{13}} & -c_{12}s_{23} - s_{12}c_{23}s_{13}e^{i\delta_{13}} & c_{23}c_{13} \end{pmatrix} \quad (1.13)$$

484 where $c_{ij} \equiv \cos\theta_{ij}$ and $s_{ij} \equiv \sin\theta_{ij}$, with i and j labelling the generations
 485 ($i, j \in \{1, 2, 3\}$). The angles θ_{12} , θ_{23} and θ_{13} are known as Euler angles.
 486 The complex phase δ_{13} allows the \mathcal{CP} violation [20] There are other popular
 487 parameterisations such as the Kobayashi-Maskawa one or the Wolfenstein
 488 one.

489 The different elements of the CKM matrix are summarised in Table 1.3
 490 . As can be seen in this table, the largest values correspond to the diagonal
 491 elements of the CKM matrix. This implies that the processes that do not
 492 change the flavour are preferred over the flavour-changing charged currents.

493 **Work in progress**

494 The \mathcal{CP} violation reflects the asymmetry between matter and antimatter. **\mathcal{CP} violation was found with kaon oscillations <- Cite this**
 495 **discovery**

CKM element	Value
V_{ud}	0.97370 ± 0.00014 [21] [22]
V_{us}	0.2245 ± 0.0008 [23] [24]
V_{cd}	0.221 ± 0.004 [25] [26] [27]
V_{cs}	0.984 ± 0.011 [28][29] [30]
V_{cb}	0.0410 ± 0.0014 [31][32]
V_{ub}	0.0038 ± 0.00024 [33] [34][35]
V_{td}	0.0080 ± 0.0003 [36][37]
V_{ts}	0.0380 ± 0.0011 [36][37]
V_{tb}	1.013 ± 0.030 [38][39][40]

Table 1.3: Magnitude of the nine elements of the CKM matrix. The mean for the different measurements has been done by [41]. **Igual me he venido arriba con las referencias. Son las que daba el Particle Data Group**

497 La violacion cp se debe a que hay tres familias -> la fase compleja de la
 498 matriz CKM es la única fuente de violación cp

499 **check:** [42]

500 1.1.3.2 Electroweak unification

501 At energies above the scale of the mass of the weak vector bosons
 502 ($E_{EW} \sim m_Z \sim m_W \sim 100$ GeV), the electromagnetic and weak interactions
 503 are unified into the Electroweak (EW) force. In other words, electromagnetism
 504 and weak interactions are simultaneously described by the symmetry
 505 group $SU(2)_L \times U(1)_Y$. The subindex L refers to left-handed fields and Y
 506 to the weak hypercharge. In contrast, at low energies, these interactions are
 507 treated as independent phenomena, the electromagnetism is described QED
 508 and the weak interaction by Fermi's theory.

In the EW model (Glashow-Salam-Weinberg model), two new quantum numbers are assigned to the particles of the SM: the weak isospin (\vec{T}) and Y . Here, the left-handed chiral states of fermions form isospin doublets (χ_L) with $T_3 = \pm 1/2$ and the right-handed form chiral states are composed of isospin singlets (χ_R) with $T_3 = 0$. For a particle, T_3 is the third component of the \vec{T} , which is related to the electric charge (Q) and the $U(1)$ hypercharge

by Gell-Mann-Nishijima relation:

$$Q = T_3 + \frac{1}{2}Y \quad (1.14)$$

- With this expression, the electromagnetic coupling and the electroweak couplings are connected. Having χ_L with $T_3 = \pm 1/2$ and χ_R with $T_3 = 0$ implies that a $SU(2)$ weak interaction can rotate left-handed particles (i.e. convert a left-handed e^- into a left-handed ν_e emitting a W^-) but cannot do the same with right-handed.

Using the gauge invariance principle it is possible to find the QED and QCD Lagrangians, as it is described in Sections 1.1.2 and 1.1.4 respectively.

The free Lagrangian, as in the case of QED and QCD is:

$$\begin{aligned} \mathcal{L} &= i \sum_{j=1}^3 \bar{\Psi}(x) \gamma^\mu \partial_\mu \Psi(x) \\ &= i \sum_{j=1}^3 \bar{\chi}_L(x) \gamma^\mu \partial_\mu \chi_L(x) + i \sum_{k=1}^3 \bar{\chi}_R(x) \gamma^\mu \partial_\mu \chi_R(x) \end{aligned} \quad (1.15)$$

where the wave function Ψ has been spited into the left isospin doublets χ_L and and right isospin singlets χ_R . The indices j and k run over the three generations of the SM. This Lagrangian should be invariant when a gauge transformation under the $SU(2)_L \times U(1)_Y$ symmetry group in the flavour space is applied:

$$\chi_L(x) \xrightarrow{SU(2)_L \times U(1)_Y} \chi'_L(x) = \exp\{i\alpha^n \tau_n\} \exp\{i\beta y\} \chi_L(x) \quad (1.16)$$

$$\chi_R(x) \xrightarrow{SU(2)_L \times U(1)_Y} \chi'_R(x) = \exp\{i\beta y\} \chi_R(x) \quad (1.17)$$

- with $\alpha, \beta \in \mathbb{R}$ and $n \in \{1, 2, 3\}$. This transformation is given by the generators of $SU(2)_L \times U(1)_Y$, i. e. the Pauli matrices (τ_n) and the weak hypercharge y . Note that $SU(2)_L$ transformation, $\exp\{i\alpha^n \tau_n\}$, only acts on the doublet fields. This term containing the Pauli matrices is non-abelian like in QCD and, like in QCD, this leads to self-interacting terms.

To ensure invariance under $SU(2)_L \times U(1)_Y$, four different gauge fields have to be added (three from $SU(2)$ and one from $U(1)$). Four is also the correct number of gauge bosons needed to describe EW interactions: W^+ , W^- , Z and Pgamma. While the three week isospin currents couple to the triplet of vector bosons W_μ^n with $n \in \{1, 2, 3\}$, the weak hypercharge couples to an isosinglet B_μ . The fields W_μ^1 and W_μ^2 are electrically charged whereas W_μ^3 and B_μ are neutral fields. The EW covariant derivative is defined as:

$$D^\mu \chi_{L_j}(x) = [\partial_\mu - ig \frac{\tau_i}{2} W_\mu^i(x) - ig' \frac{y_j}{2} B_\mu(x)] \chi_{L_j}(x) \quad i \in [1, 2, 3] \quad (1.18)$$

$$D^\mu \chi_{R_j}(x) = [\partial_\mu - ig' \frac{y_j}{2} B_\mu(x)] \chi_{R_j}(x) \quad (1.19)$$

521 where g and g' are the interaction couplings to W_μ^i isotriplet and the B_μ
 522 isosinglet.

Using the derivatives in equations 1.18 and 1.19, the Lagrangian in 1.20 is already invariant under local $SU(2)_L \times U(1)_Y$ transformations:

$$\mathcal{L} = i \sum_{j=1}^3 \bar{\chi}_L^j(x) \gamma^\mu D_\mu \chi_L^j(x) + i \sum_{k=1}^3 \bar{\chi}_R^k(x) \gamma^\mu D_\mu \chi_R^k(x) \quad (1.20)$$

Finally, if kinetic terms for the gauge bosons are included in 1.20, the EW SM Lagrangian is obtained:

$$\begin{aligned} \mathcal{L}_{EW} = & i \sum_{j=1}^3 \bar{\chi}_L^j(x) \gamma^\mu D_\mu \chi_L^j(x) + i \sum_{k=1}^3 \bar{\chi}_R^k(x) \gamma^\mu D_\mu \chi_R^k(x) \\ & - \frac{1}{4} W_{\mu\nu}^n(x) W_n^{\mu\nu}(x) - \frac{1}{4} B_{\mu\nu}(x) B^{\mu\nu}(x) \end{aligned} \quad (1.21)$$

523 Where the addition of kinetic terms gives rise to cubic and quadratic self-
 524 interactions among the gauge fields. Note that the mass terms of the fields
 525 are forbidden in order to ensure local gauge invariance.

This Lagrangian describes the interactions between gauge vector bosons and fermions below

$$\begin{array}{lll} \chi_L & = \begin{pmatrix} \nu_e \\ e \end{pmatrix}_L \begin{pmatrix} \nu_\mu \\ \mu \end{pmatrix}_L & \begin{pmatrix} \nu_\tau \\ \tau \end{pmatrix}_L \begin{pmatrix} u \\ d \end{pmatrix}_L \quad \begin{pmatrix} c \\ s \end{pmatrix}_L \begin{pmatrix} t \\ b \end{pmatrix}_L \\ \chi_R & = e_R \mu_R & \tau_R u_R d_R \quad c_R s_R t_R b_R \end{array}$$

526 **Esto se ve muy feo: Editar χ_L y χ_R .**

527 The in \mathcal{L}_{EW} in 1.21 can be divided in two different parts according to
 528 the charge of the bosons: charged currents and neutral currents. Relating
 529 the charged currents (W_μ^1 and W_μ^2) to the W^+ and W^- bosons of the SM
 530 and the neutral (W_μ^3 and B_μ) ones with the Z and γ , it is possible to build
 531 linear combinations fo the original gauge fields that define the SM bosons.

Reescribir a partir de aquí para que quede más bonito

For the charged-current interactions:

$$W^\pm \equiv \frac{1}{\sqrt{2}} (W_\mu^1 \mp i W_\mu^2) \quad (1.22)$$

While for the neutral-current this combinations are a rotation of the so called Weinberg (or weak mixing) angle θ_W :

$$\begin{pmatrix} W_\mu^3 \\ B_\mu \end{pmatrix} \equiv \begin{pmatrix} \cos\theta_W & \sin\theta_W \\ -\sin\theta_W & \cos\theta_W \end{pmatrix} \begin{pmatrix} Z_\mu \\ A_\mu \end{pmatrix} \quad (1.23)$$

532 Measurements of θ_W give a value of $\sin^2\theta_W = 0.2310 \pm 0.0005$ [43].

In order to ensure that this A_μ is the one of QED, apart from the Gell-Mann-Nishijima relation (equation 1.14), it has to be satisfied that:

$$g \sin\theta_W = g' \cos\theta_W = e \quad (1.24)$$

533 .

534 Comentar algo el GIM mechanism y las FCNC

535 There is no mass term for the bosons in the EW Lagrangian that has
 536 been obtained in 1.21 by demanding the $SU(2)_L \times U(1)_Y$ local invariance,
 537 which enters in contradiction with the experimental observations for the
 538 W and Z bosons ($m_{Z,W} \sim 80$ GeV). The introduction of such a mass term
 539 would break the symmetry, however, the it is possible to add the mass for
 540 the W and Z bosons without loosing the properties of the symmetry. The
 541 method to do so is known as Englert–Brout–Higgs–Guralnik–Hagen–Kibble
 542 mechanism or, more commonly, just as Higgs mechanism and is described
 543 in Section 1.1.5.

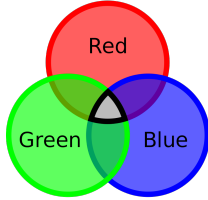
544 1.1.4 Quantum chromodynamics

545 1.1.4.1 Quarks and colour

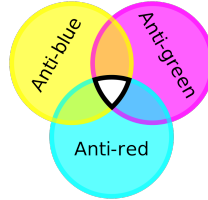
546 Quantum chromodynamics (QCD) is QFT-based theory for describing
 547 the strong interactions between quarks and gluons (partons). This type of
 548 interaction is the responsible of the nuclear force, the one that acts between
 549 the protons and neutrons of atoms binding them together. Without the
 550 strong force, the protons inside the nucleus would push each other apart
 551 due to the electromagnetic repulsion. It also holds the quarks within a
 552 hadron together.

QCD is based in the $SU(3)$ symmetry group and its name derives from the “colour” charge, an analogous to the electric charge of QED but for strong interactions. The colour charge was introduced in 1964 [44] to explain how quarks could coexist within some hadrons apparently having the same quantum state without violating the Pauli exclusion principle. To satisfy the Fermi-Dirac statistics it is necessary to add an additional quantum number, the colour, to the theory. Each specie of quark (q) may have three different colours (q^α , $\alpha = 1, 2, 3$): red, green, blue. Baryons and mesons are described then by the colour singlet combinations:

$$B = \frac{1}{\sqrt{6}} \epsilon^{\alpha\beta\gamma} |q_\alpha q_\beta q_\gamma\rangle \quad M = \frac{1}{\sqrt{3}} \epsilon^{\alpha\beta} |q_\alpha \bar{q}_\beta\rangle$$



(a) Quark colours combine to be colourless.



(b) Antiquark colours also combine to be colourless.

Figure 1.3: Colour charge combinations for quarks and antiquarks

553 .

554 Additionally, it is postulated that all hadrons must have a global neut-
 555 ral colour charge, i. e. the hadrons must be “colourless”. This assumption
 556 is known as confinement hypothesis and it is made to avoid the existence
 557 of non-observed extra states with non-zero colour. It is called colour con-
 558 finement because it implies that it is not possible to observe free quarks
 559 since they carry colour charge and, hence, they have to be confined within
 560 colour-singlet combinations. Figure 1.3 depicts how different colours and
 561 anticolours combine to create the “colourless” state.

562 1.1.4.2 Gauge invariance for $SU(3)$

The dynamics of the quarks and gluons are controlled by the QCD Lagrangian. Using the power of the gauge invariance principle it is possible to deduce \mathcal{L}_{QCD} similarly to the reasoning developed in Section 1.1.2. Firstly, let's denote a quark field of colour α and flavour f by q_f^α . The vector $q_f^T \equiv (q_f^1, q_f^2, q_f^3)$ is defined under the $SU(3)$ colour space, meaning that each dimension corresponds to a colour. The Lagrangian

$$\mathcal{L}_0 = \sum_f \bar{q}_f (i\gamma^\mu \partial_\mu - m_f) q_f \quad (1.25)$$

is invariant under global $SU(3)$ transformation in the colour space,

$$q_f^\alpha \rightarrow (q_f^\alpha)' = U_\beta^\alpha q_\beta^\alpha, \quad UU^\dagger = U^\dagger U = 1, \quad \det U = 1 \quad (1.26)$$

563 .

In the $SU(N)$ algebra, $SU(N)$ is the group of $N \times N$ unitary matrices (U) which can be written in the form $U = \exp\{i(\lambda^a/2)\theta_a\}$ with $a = 1, 2, \dots, N^2 - 1$. Therefore, the $SU(3)$ matrices can be written as

$$U = \exp\left\{i\frac{\lambda^a}{2}\theta_a\right\} \quad (1.27)$$

where the index a goes from 1 to 8 for the arbitrary parameter θ_a and $\frac{\lambda^a}{2}$, which denotes the fundamental representation of the $SU(3)$ algebra.

The Einstein notation for summation over repeated indices is implied. The matrices λ^a are traceless and satisfy the commutation relations [11]:

$$\left[\frac{\lambda^a}{2}, \frac{\lambda^b}{2} \right] = i f^{abc} \frac{\lambda^c}{2}$$

564, being f^{abc} the $SU(3)_C$ structure constants, which are real and totally
565 antisymmetric.

To satisfy the gauge invariance requirement, the Lagrangian has to be invariant under $SU(3)$ local transformations, i.e, transformations in which the phase is dependent of the space time location, $\theta_a = \theta_a(x)$. To fulfil the condition, the quark derivatives in the Lagrangian in 1.25 have to be substituted by covariant objects. Since there are eight independent gauge parameters, eight different gauge bosons $G_a^\mu(x)$ are needed⁷. These bosons are the eight gluons and the new covariant objects are:

$$D^\mu q_f \equiv \left[\partial_\mu + ig_s \frac{\lambda^a}{2} G_a^\mu(x) \right] q_f \equiv [\partial_\mu + ig_s G^\mu(x)] q_f$$

566 The compact matrix notation is used $[G^\mu(x)]_{\alpha\beta} \equiv \left(\frac{\lambda^a}{2} \right)_{\alpha\beta} G_a^\mu(x)$.

To ensure that the covariant derivative ($D^\mu q_f$) transforms like the q_f , the transformation of the gauge fields are:

$$D^\mu \rightarrow (D^\mu)' = U D^\mu U^\dagger \quad G^\mu \rightarrow (G^\mu)' = U G^\mu U^\dagger + \frac{i}{g_s} (\partial_\mu U) U^\dagger \quad (1.28)$$

. The quark and gluon fields transform under an infinitesimal local transformation, i.e. $\theta_a(x) = \delta\theta_a(x) \approx 0$, the $SU(3)_C$ unitary matrices (eq. 1.27) can be expressed as their first order expansion:

$$U = \exp \left\{ i \frac{\lambda^a}{2} \theta_a(x) \right\} \approx 1 + i \left(\frac{\lambda^a}{2} \right) \delta\theta_a(x)$$

and, consequently, the transformations for the colour-vector field (eq. 1.26) and gluon field (eq. 1.28) become:

$$\begin{aligned} q_f^\alpha &\rightarrow (q_f^\alpha)' = q_f^\alpha + \left(\frac{\lambda^a}{2} \right)_{\alpha\beta} \delta\theta_a q_f^\beta \\ G_a^\mu &\rightarrow (G_a^\mu)' = G_a^\mu - i \frac{i}{g_s} \partial_\mu (\delta\theta_a) - f^{abc} \delta\theta_b G_c^\mu \end{aligned}$$

567 .

⁷The eightfold multiplicity of gluons is labeled by a combination of color and anticolor charge (e.g. red–antigreen)

In contrast to the transformation for the photon field in QED (equation 1.5), the non-commutativity⁸ of the $SU(3)_C$ matrices give rise to an additional term involving the gluon fields themselves ($-f^{abc}\delta\theta_b G_c^\mu$), as the relation 1.1.4.2 expresses. For constant $\delta\theta_a$, the transformation rule for the gauge fields is expressed in terms of the structure constants f^{abc} ; thus, the gluon fields belong to the adjoint representation for the colour group. There is a unique coupling at $SU(3)_C$, g_s . All the colour-triplet flavours couple to the gluon fields with exactly the same interaction strength.

It is necessary to introduce the corresponding fields strengths to build a gauge-invariant kinetic terms for the gluon fields.

$$G^{\mu\nu} \equiv -i\frac{-i}{g_s}[D^\mu, D^\nu] = \partial_\mu G^\nu - \partial_\nu G^\mu + ig_s[G^\mu, G^\nu] \equiv \frac{\lambda^a}{2}G_a^{\mu\nu}(x)$$

$$G_a^{\mu\nu} \equiv \partial_\mu G_a^\nu - \partial_\nu G_a^\mu - g_s f^{abc} G_b^\mu G_c^\nu$$

Under a $SU(3)_C$ transformation,

$$G^{\mu\nu} \rightarrow (G^{\mu\nu})' = U G^{\mu\nu} U^\dagger \quad (1.29)$$

and the colour trace $\text{Tr}(G^{\mu\nu}G_{\mu\nu}) = \frac{1}{2}G^{\mu\nu}G_{\mu\nu}$ remains invariant. Normalising the gluon kinetic term, the $SU(3)_C$ invariant QCD Lagrangian is obtained:

$$\mathcal{L}_{QCD} \equiv -\frac{1}{4}G_a^{\mu\nu}G_{\mu\nu}^a + \sum_f \bar{q}_f(i\gamma^\mu D_\mu - m_f)q_f \quad (1.30)$$

Note how the gluon-gluon vertex is find by demanding the gauge invariance under local $SU(3)_C$ transformation. A mass term is forbidden for the gluon fields by the $SU(3)_C$ gauge symmetry because something of the form $\frac{1}{2}m_G^2 G_a^\mu G_\mu^a$ would not be invariant under the transformation in 1.28. The gluons are, then, predicted by the theory to be spin-1 massless particles.

Thanks to the colour symmetry properties this Lagrangian looks very simple, with all the interactions depend on the strong coupling constant, g_s . In contrast to the Lagrangian derived for QED (eq 1.7), in \mathcal{L}_{QCD} the boson field have a self-interacting term. This gluon self-interactions give rise to the triple and quadratic gluon vertex (Figure 1.4). This self-interactions among the gluon fields can explain features the asymptotic freedom and confinement, properties that were not present in QED. The asymptotic freedom causes interactions between particles to become asymptotically weaker as the energy scale increases and the corresponding length scale decreases. The confinement implies that the strong forces increase with the distance,

⁸Because the generators of $SU(3)$ do not commute, QCD is known as non-Abelian gauge theory.

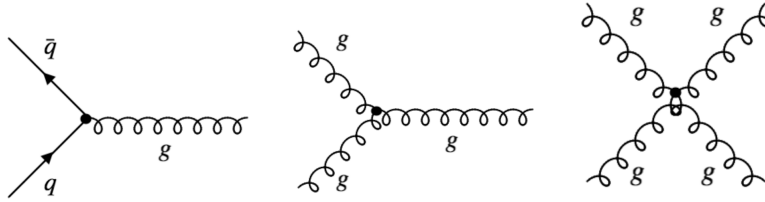


Figure 1.4: The predicted QCD interaction vertices arising from the requirement of $SU(3)_C$ local gauge invariance. The presence of the triples and quadruple gluon vertices is possible to the Non-Abelian nature of $SU(3)_C$.

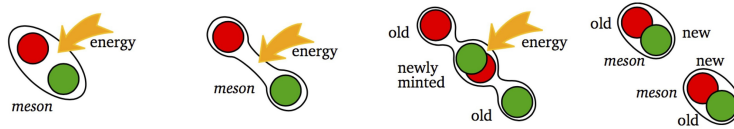


Figure 1.5: The QCD colour confinement explains the inseparability of quarks inside a hadron in spite of investing ever more energy. In this example, the mechanism is shown for a meson.

591 therefore, as two colour charges are separated, at some point it becomes en-
 592 ergetically favorable for a new quark-antiquark pair to appear rather than
 593 keep getting further. This new quarks bond with the previous two, pre-
 594 venting single quarks to be isolated. This mechanism is depicted in Figure
 595 1.5. This explains why the strong interaction is responsible for keeping the
 596 quarks together forming hadrons.

597 **Maybe, expand the QCD Lagrangian in 1.30 and explain its
 598 different elements.**

599 1.1.5 Particle masses

For the QED Lagrangian, \mathcal{L}_{QED} (eq. 1.9), it is clear how the mass of the photon must be zero in order to satisfy the $U(1)$ local gauge symmetry because, if a mass term for the vector gauge field A_μ is included, the \mathcal{L}_{QED} would be:

$$\mathcal{L}_{QED} = \bar{\Psi}(x)(i\gamma^\mu\partial_\mu - m)\Psi(x) - eQ\bar{\Psi}(x)\gamma^\mu A_\mu\Psi(x) - \frac{1}{4}F_{\mu\nu}(x)F^{\mu\nu}(x) + \frac{1}{2}m_\gamma^2 A_\mu A^\mu$$

and, with the $U(1)$ transformation in equation 1.5, the new mass term becomes:

$$\frac{1}{2}m_\gamma^2 A_\mu A^\mu \rightarrow \frac{1}{2}m_\gamma^2 (A_\mu + \frac{1}{e}\partial_\mu\theta)(A^\mu + \frac{1}{e}\partial^\mu\theta) \neq \frac{1}{2}m_\gamma^2 A_\mu A^\mu$$

600 Confirming that the photon mass term is not invariant under local $U(1)$
 601 and, consequently, that the photon must be massless to satisfy the gauge

invariance. Experimental efforts to measure the mass of the photon have set an upper limit of $m_\gamma \leq 1 \times 10^{-18}$ eV [45].

With the Lagrangian of QCD in equation 1.30 happens the same, the mass term for the gluon fields are forbidden by the $SU(3)_C$ gauge symmetry. Therefore, the mediating bosons for the strong interactions are massless as well (experimentally, a mass as large as upper limits of a few MeV have been seted, see [46]).

While the prohibition of mass terms for the bosons of QED and QCD is not a problem, this requirement also applies to the $SU(2)_L$. This condition enters into open contradiction with the measurements of large masses for the W ($m_W = 80.370 \pm 0.007$ (stat.) ± 0.017 (syst.) MeV[47]) and Z ($m_Z = 91.1852 \pm 0.0030$ GeV [48]) bosons of weak interactions. *<- to do: Aquí no estoy utilizando las mismas medidas de la masa de m_W y m_Z que antes. He de escoger una and stick to it.*

For weak interactions, the problem of massless particles do not only affect the bosons. Since under the $SU(2)_L$ transformations left-handed particles transform as weak isospin doubles and right-handed particles as isospin singlets, the mass term of a spinor field Ψ written as chiral states also breaks the required gauge invariance: $-m\bar{\Psi}(x)\Psi(x) = -m\bar{\Psi}(x)(P_R + P_L)\Psi(x) = -m(\bar{\Psi}_R(x)\Psi_L(x) + \bar{\Psi}_L(x)\Psi_R(x))$

The Higgs mechanism describes how both the W and Z bosons and the fermions acquire mass without breaking the local gauge symmetry of the SM.

1.1.5.1 The Higgs mechanism

Goldstone theorem and spontaneous symmetry breaking

For a scalar field ϕ with a Lagrangian of the form:

$$\mathcal{L} = \frac{1}{2}\partial_\mu\phi_i\partial^\mu\phi_i - V(\phi) \text{ where } V(\phi) = \frac{1}{2}\mu^2\phi_i\phi_i + \frac{1}{4}\lambda(\phi_i\phi_i)^2 \quad (1.31)$$

This Lagrangian is invariant under $\phi_i \rightarrow \phi'_i = R_{ij}\phi_j$, where R_{ij} are rotational matrices in 4-dimensions. The mass term is the one with $\phi_i\phi_i$ and the parameter λ has to be positive for \mathcal{L} to describe a physical system, if $\lambda < 0$ the potential is unbounded from below. Contrary, the parameter μ^2 can be either positive or negative. As depicted in Figure 1.6a, if $\mu^2 > 0$, the vacuum expectation value (i.e. minimum of potential) is located at the origin ϕ_0 and this \mathcal{L} would describe a spin-0 particle of mass μ . However, if $\mu^2 < 0$, the potential $V(\phi)$ has the form of Figure 1.6a and \mathcal{L} would not represent anymore the Lagrangian of a particle of mass μ . The vacuum

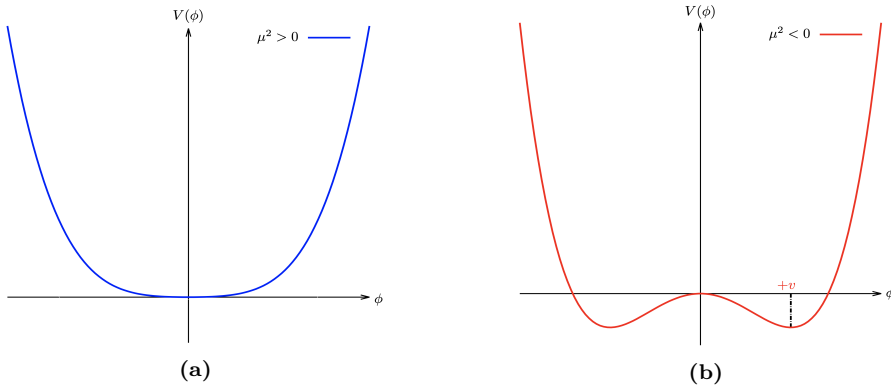


Figure 1.6: The potential $V(\phi)$ of Lagrangian 1.31 for (a) μ^2 positive and (b) negative.

expectation value is now multivalued:

$$\phi_0 = \pm \sqrt{-\frac{\mu^2}{\lambda}} \equiv \pm v \quad (1.32)$$

Expanding the field around the minima at $\phi_i = (0, 0, 0, v)$, the \mathcal{L} becomes:

$$\begin{aligned} \mathcal{L} = & \frac{1}{2} \partial_\mu \sigma \partial^\mu \sigma + \mu^2 \sigma^2 - \sqrt{\mu^2 \lambda} \sigma^3 - \frac{1}{4} \lambda^4 \\ & + \frac{1}{2} \partial_\mu \pi_i \partial^\mu \pi_i - \frac{1}{4} \lambda (\pi_i \pi_i)^4 - \lambda v \pi_i \pi_i \sigma - \frac{1}{2} \pi_i \pi_i \sigma^2 \end{aligned} \quad (1.33)$$

where i runs from 1 to 3. Here $\sigma = \phi_4 - v$ and $\pi_i = \phi_i$ are new boson fields, being the latter massless and the with a mass of $m_\sigma^2 = -2\mu^2$. The new terms break the original symmetry because the symmetry of the Lagrangian is not longer a symmetry of the vacuum, it has been spontaneously broken. One massive σ boson and three massless π_i bosons with a residual $O(3)$ symmetry have appeared. This is a consequence of the Goldstone theorem which states that “for a continuous symmetry group \mathcal{G} spontaneously broken down to a subgroup \mathcal{H} , the number of broken generators is equal to the number of massless scalars that appear in the theory” [49]. Therefore, since the $O(N)$ group has $N(N-1)/2$ generators, the $O(N-1)$ has $(N-1)(N-2)/2$ and, hence, $N-1$ Goldstone bosons appear. The example shown is for $N=4$

The Higgs mechanism in the SM - Bosons

To apply this mechanism to the SM, it is necessary to generate mass for the W^+ , W^- and Z bosons while keeping the photon massless. In order to do so, the EW symmetry group $SU(2)_L \times U(1)_Y$ has to be broken to a $U(1)$ subgroup describing electromagnetism. A gauge-invariant interaction that gives masses to fermions without mixing chiral components is introduced by

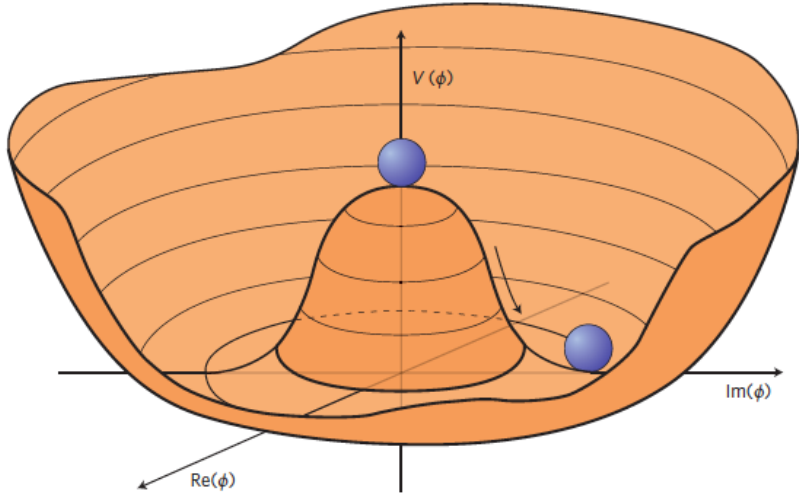


Figure 1.7: An illustration of the Higgs potential $V(\Phi)$ in the case of $\mu^2 < 0$. Choosing any particular point in the circle defined by v spontaneously breaks the $U(1)$ rotational symmetry. This type of potential is frequently called “Mexican hat”.

defining a $SU(2)$ isospin doublet of complex scalar field with hypercharge $Y = 1$:

$$\Phi = \begin{pmatrix} \phi^+ \\ \phi_0 \end{pmatrix}$$

Being ϕ^+ positively charged and ϕ^0 neutral. The Lagrangian \mathcal{L}_{Higgs} has to be added to the \mathcal{L}_{EW} in 1.21.

$$\mathcal{L}_{Higgs} = (D_\mu \Phi)^\dagger (D^\mu \Phi) - V(\Phi) \text{ where } V(\Phi) = \mu^2 \Phi^\dagger \Phi + \lambda (\Phi^\dagger \Phi)^2$$

with $\lambda > 0$ required for vacuum stability. When $\mu^2 > 0$, the minimum of the potential occurs when both fields (ϕ^+ and ϕ^0) are at zero. If $\mu^2 < 0$, the minimum of the potential has an infinite number of degenerate states that satisfy $\Phi^\dagger \Phi = \mu^2 / 2\lambda$ and the physical vacuum state will correspond to any particular point on the circle of Figure 1.7. Having to chose a particular point breaks the global $U(1)$ symmetry of the Lagrangian. Without loss of generality, in this scenario, the ground state Φ_0 can be chosen to be:

$$\Phi_0 = \frac{1}{\sqrt{2}} \begin{pmatrix} 0 \\ v \end{pmatrix} \text{ where } v = 2\sqrt{\frac{\mu^2}{\lambda}}$$

⁶³⁷ being v the vacuum expectation value and defines the before mentioned
⁶³⁸ circle in the minimum of $V(\Phi)$ in the $\mu^2 < 0$ scenario.

The Lagrange density must be formulated in terms of deviations from one of these ground states. This can be done by introducing an excitation

$(h(x))$ that can be understood as a small deviation of the field from the ground state. Accordingly, the fields can be expanded around the minimum as:

$$\Phi = \frac{1}{\sqrt{2}} \begin{pmatrix} 0 \\ v + h(x) \end{pmatrix} \exp\{i\chi(x)\}$$

The new field $\chi(x)$ can be set to zero in the so called “unitary gauge”.

$$\Phi = \frac{1}{\sqrt{2}} \begin{pmatrix} 0 \\ v + h(x) \end{pmatrix} \quad (1.34)$$

Expanding the covariant derivative of the \mathcal{L}_{Higgs} :

$$\begin{aligned} (D_\mu \Phi)^\dagger (D^\mu \Phi) &= \left| \left(\partial_\mu + ig \frac{\tau^k}{2} W_\mu^k(x) + ig' \frac{y}{2} B_\mu \right) \right|^2 \\ &= \frac{1}{2} \left| \begin{pmatrix} \partial_\mu + i\frac{1}{2}(gW_\mu^3 + g'\frac{y}{2}B_\mu) & i\frac{g}{2}(W_\mu^1 - iW_\mu^2) \\ i\frac{g}{2}(W_\mu^1 - iW_\mu^2) & \partial_\mu - i\frac{1}{2}(gW_\mu^3 - g'\frac{y}{2}B_\mu) \end{pmatrix} \begin{pmatrix} 0 \\ v + h \end{pmatrix} \right|^2 \\ &= \frac{1}{2}(\partial_\mu h)^2 + \frac{1}{8}(v + h)^2 |W_\mu^1 - iW_\mu^2|^2 \\ &\quad + \frac{1}{8}(v + h)^2 |gW_\mu^3 - g'B_\mu| + (\text{interaction terms}) \end{aligned}$$

Where the τ_k with $k = 1, 2, 3$ are the already introduced Pauli Matrices. In this equation there are terms mixing the W^3 and the B_μ fields that, by using the physical fields defined in equation 1.23, should disappear since the physical bosons don't mix. Applying the relation 1.23 into the covariant derivative,

$$(D_\mu \Phi)^\dagger (D^\mu \Phi) = \frac{1}{2} + \frac{g^2 v^2}{4} W_\mu^+ W^{-\mu} + \frac{g^2 v^2}{8 \cos^2 \theta_W} Z_\mu Z^\mu + 0 A_\mu A^\mu$$

, the W^+ , W^- and Z bosons have finally acquired mass. Through to the Higgs mechanism, their masses within the SM are:

$$M_W = \frac{1}{2} g v \quad M_Z = \frac{1}{2} \frac{g v}{\cos \theta_W}$$

639 Additionally, a new scalar field $h(x)$ has appeared with its correspondent
 640 mass term, the Higgs field. Note that the $h(x)$ was introduced as a perturba-
 641 tion from the ground state of the Higgs potential $V(\Phi)$, so the Higgs boson
 642 can be understood as an excitation of the Higgs potential. Apart from cou-
 643 plings to the electroweak gauge fields, the Higgs field has also self-interaction
 644 vertices. The mass of this boson is $m_H = \sqrt{2}\mu$.

With this covariant term, the Higgs Lagrangian density of the system is obtained:

$$\begin{aligned}\mathcal{L}_{Higgs} = & \frac{1}{2}(\partial_\mu h)(\partial^\mu h) + \frac{g}{4}(v+h)^4 W_\mu W^\mu + \frac{g^2}{8\cos^2\theta_W}(v+h)^2 Z_\mu Z^\mu \\ & + \frac{\mu^2}{2}(v+h)^2 - \frac{\lambda}{16}(v+h)^4\end{aligned}$$

and expressing it in terms of the boson masses and coupling parameters, it can be written as:

$$\begin{aligned}\mathcal{L}_{Higgs} = & \frac{1}{2}(\partial_\mu h)(\partial^\mu h) - \frac{1}{2}m_H^2 h^2 + \frac{1}{2}m_W W_\mu W^\mu + \frac{1}{2}m_Z Z_\mu Z^\mu + gm_W h W_\mu W^\mu \\ & + \frac{g^2}{4}W_\mu W^\mu + g\frac{m_Z}{2\cos\theta_W}hZ_\mu Z^\mu - g^2\frac{1}{4\cos^2\theta_W}h^2 Z_\mu Z^\mu - g\frac{m_H^2}{4m_W}h^3 \\ & - g^2\frac{m_H^2}{32m_W^2}h^4 + \text{const.}\end{aligned}\tag{1.35}$$

As can be seen in the Lagrangian 1.35, the coupling strengths of the W and Z fields to the Higgs are proportional to m_W and m_Z respectively. This why it is said that the more a fundamental particle interacts with the Higgs boson, the more massive it is.

The Higgs mechanism in the SM - Fermions

The Higgs mechanism for spontaneous symmetry breaking of the $SU(2)_L \times U(1)_Y$ gauge group of the SM generates the masses of the W^\pm and Z bosons. For originating the mass of the fermions without violating the EW gauge symmetry a similar procedure is carried but taking into account that the left-handed particles transform different than the right-handed. To do so, additional terms including the Yukawa couplings are added into the Lagrangian. These terms are of the form:

$$-y_f(\bar{\chi}_L^f \Phi \chi_R^f + \bar{\chi}_R^f \Phi^\dagger \chi_L^f)$$

where the f superindex runs over all quarks and charged leptons. It is usual to express the second part of the sum just as “plus hermitic conjugate” (“+ h.c.”). Note that the hermitic conjugate part is necessary to ensure that expression fulfills the requirement for a hermitian operator to be self-adjoint in a complex Hilbert space. The different y_f constants are known as Yukawa couplings of the particle f to the Higgs field. The Higgs doublet is denoted by Φ . For the electron $SU(2)$ doublet, the element with this coupling can be written as:

$$\mathcal{L}_e = -y_e \left[(\bar{\nu}_e \bar{e})_L \begin{pmatrix} \phi^+ \\ \phi^0 \end{pmatrix} e_R + \bar{e}_R (\phi^{+*} \phi^{0*}) \begin{pmatrix} \nu_e \\ e \end{pmatrix}_L \right]\tag{1.36}$$

Here, y_e is the Yukawa coupling of the electron to the Higgs boson. After spontaneously breaking the symmetry as it is done in eq. 1.34, the Lagrangian in 1.36 becomes:

$$\mathcal{L}_e = \frac{-y_e}{\sqrt{2}}v(\bar{e}_L e_R + \bar{e}_R e_L) + \frac{-y_e}{\sqrt{2}}h(\bar{e}_L e_R + \bar{e}_R e_L) \quad (1.37)$$

The y_e is not predicted by the Higgs mechanism, but can be chosen to be consistent with the observed electron mass (m_e) so that $y_e = \sqrt{2}m_e/v$. Using this relation, the Lagrangian in 1.37 becomes:

$$\mathcal{L}_e = -m_e \bar{e}e - \frac{m_e}{v} \bar{e}eh \quad (1.38)$$

649 The first element of the Lagrangian in 1.38 gives mass to the electron and
 650 gives rise to the coupling of the electron to the Higgs fields in its non-
 651 zero vacuum expectation. The second term represents the coupling of the
 652 electron and the Higgs boson itself.

653 The non-zero vacuum expectation value occurs only in the neutral part
 654 of the Higgs doublet (the lower in $\Phi = \begin{pmatrix} \phi^+ \\ \phi_0 \end{pmatrix}$) due to the form in the
 655 ground state in 1.34. This implies that the combination $\bar{\chi}_L^f \Phi \chi_R^f + \bar{\chi}_R^f \Phi^\dagger \chi_L^f$
 656 can only generate masses for the fermions in the lower component of an
 657 $SU(2)$ doublet, i.e. the charged leptons and the down type quarks. Putting
 658 aside the procedure to give mass to the up-type quarks, this explains why
 659 the neutrinos do not get mass through the Higgs mechanism.

For the up-type quarks, a gauge invariant term can be constructed from $\bar{\chi}_L^f \Phi_c \chi_R^f + \bar{\chi}_R^f \Phi_c^\dagger \chi_L^f$:

$$\mathcal{L}_u = y_u (\bar{u} \bar{d})_L \begin{pmatrix} -\phi^{0*} \\ \phi^- \end{pmatrix} u_R + \text{h.c.}$$

Applying the symmetry breaking:

$$\mathcal{L}_u = \frac{-y_u}{\sqrt{2}}v(\bar{u}_L u_R + \bar{u}_R u_L) + \frac{-y_u}{\sqrt{2}}h(\bar{u}_L u_R + \bar{u}_R u_L)$$

with a Yukawa coupling between the up quark and the boson $y_u = \sqrt{2}m_u/v$, resulting in:

$$\mathcal{L}_u = -m_u \bar{u}u - \frac{m_u}{v} \bar{u}uh$$

Therefore, for Dirac fermions, mass terms that let the Lagrangian invariant under local gauge transformations can be constructed from

$$\mathcal{L} = -y_f \left[\bar{\chi}_L^f \Phi \chi_R^f + (\bar{\chi}_R^f \Phi \chi_L^f)^\dagger \right] \quad \text{or} \quad \mathcal{L} = y_f \left[\bar{\chi}_L^f \Phi_c \chi_R^f + (\bar{\chi}_R^f \Phi_c \chi_L^f)^\dagger \right]$$

. The left Lagrangian is used for the leptons and down-type quarks, while the right one is used for the up-type quarks. These elements give rise not only to the mass of the fermions but also to the interaction strengths between these fermions and the Higgs boson. The Yukawa coupling of the fermions to the Higgs field is given by:

$$y_f = \sqrt{2} \frac{m_f}{v} \tag{1.39}$$

661 where the Higgs vacuum expectation value is fixed by the Fermi coupling
 662 G_F and is measured to be $v = \sqrt{2} G_F \approx 246.22 \text{ GeV}$. The G_F is measured
 663 from the μ^+ lifetime [50]. The G_F is also used to determine the magnitude
 664 of the elements in the CKM matrix.

665 The value of fermionic masses is not predicted by the SM but obtained
 666 through experimental observations. Given the $m_{top} = 172.76 \pm 0.30 \text{ GeV}$,
 667 it is of particular interest the Yukawa coupling of the top quark to the
 668 Higgs field, y_t , which is almost exactly equal to one. It is important to
 669 verify this because deviation of the measured y_t from the SM prediction
 670 would be a proof of new phenomena beyond the SM that could provide an
 671 answer to several open questions concerning the fundamental interactions
 672 of elementary particles.

673 1.1.6 Charge-Parity

674 **Probably, this section is gonna be absorbed by 1.1.3**

675 1.1.7 Problems with the Standard Model

676 While the SM is very good theory that has passed rigorous testing, this
 677 is not the ending of the story, there are several limitations of the SM and
 678 phenomena that it does not explain. The SM does not cover all questions
 679 in the universe and, hence, physicist continue looking for better theories to
 680 explain more. There is a long list of small and minor issues with the SM
 681 but lets focus on the most relevant ones.

682 **Section under development**

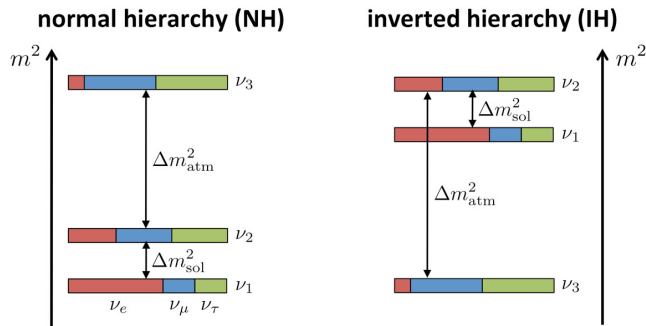


Figure 1.8: Two potential mass orderings of neutrinos are the normal ordering (normal hierarchy) and the inverted ordering (inverted hierarchy)

683 Gravity

684 Gravity is the first force that any person learns about and the one known
 685 by the humankind for the most time. The SM describes all the other funda-
 686 mental interactions but this one. Some of the suggested solutions to this
 687 problem consist in postulating a new force carrier particle, the “graviton”,
 688 that mediates this interaction in a similar way to how the gauge bosons were
 689 proposed. Other explanations state that the gravity can only be described
 690 by a deeper theory in which the time-space structure is not flat like it is in
 691 the SM but dynamic.

692 Neutrino masses

693 According to the SM the neutrinos are massless, nevertheless, many ex-
 694 periments confirm that this is not true [citas citas](#). This known due to a
 695 property of neutrinos that allows them to change their flavour while trav-
 696 eling through the space, this feature is known as “neutrino oscillations”.
 697 The tree flavours of neutrinos is a linear combination of three discrete mass
 698 eigenstates (ν_i with $i \in \{1, 2, 3\}$) with mass eigenvalues (m_i). While the
 699 neutrino oscillation experiments could probe the squared neutrino-mass ei-
 700 genvalues (Δm_{ij}^2), both the total scale of the masses and the sign of Δm_{ij}
 701 remains as some the most relevant open questions in particle physics. Re-
 702 garding to the sign of Δm_{ij} , it is known that the mass of ν_2 is slightly higher
 703 than ν_1 ($\Delta m_{21}^2 \equiv m_2^2 - m_1^2 \sim 10^{-4}$ eV) but for the third mass eigenstate
 704 it has not been measured yet whether it is greater (normal ordering) or
 705 lower (inverted ordering) than the other two. This is known as “hierarchy
 706 problem” and is depicted in Figure 1.8. Nevertheless, the absolute square
 707 difference is known ($\Delta m_{31}^2 \equiv |m_3^2 - m_1^2| \sim 10^{-3}$ eV).

708 Regarding to the nature of this mass, one could add mass terms to the
 709 SM as it is done in Section 1.1.5.1 for the up-type quarks but the origin of

710 the neutrino masses is still not known. It is possible that this mass comes
711 from the Higgs mechanism, however, this is not clear. Also, if neutrinos
712 gained mass through Yukawa interaction, it would imply the presence of
713 right-handed neutrinos, which has not been observed.

714 **Matter-antimatter asymmetry**

715 By looking at the CMB radiation, which contain the residual photons of the
716 Big Ban, researchers have determined that there was a symmetry between
717 the matter and antimatter content in the early universe. For every 3×10^9
718 antimatter particles, there were 3×10^9 and 1 matter particles. The matter
719 and antimatter annihilate and produced the CMB and the remaining 1 part
720 turned into all the stars and galaxies that are seen.

721 So, what is the physical phenomena that generated this asymmetry? To
722 solve this the \mathcal{CP} violation is needed

723 - Leptogenesis - The SM has too little \mathcal{CP} violation to account for the
724 matter-antimatter asymmetry in the universe

725 **Strong \mathcal{CP} problem**

726

727 **Dark energy**

728 According to cosmological observations, the matter described by the SM
729 only makes up around 5% of the universe. It turns out that roughly 68%
730 of the universe is dark energy, which is not considered by the SM. Dark
731 energy is an unknown type of energy postulated to explain the observed
732 accelerated expansion of the universe. This expansion is dominated by
733 a spatially smooth component with negative pressure called dark energy.
734 Modern cosmological measurements are based in supernovae, cosmic
735 microwave background fluctuations, galaxy clustering and weak gravitational
736 lensing, and methods agree with a spatially flat universe with about 30%
737 matter (visible and dark) and 70% dark energy [51].

738 **Dark matter**

739 The rest of the energy content (27%) in the universe is the dark matter
740 (DM), which adds up for approximately 85% of all matter. This matter is
741 called dark because it does not interact with the electromagnetic field, so
742 maybe a name such us invisible matter would have been more appropriate.
743 The only way to interact with DM is via gravitational interaction, which is
744 bout 25 orders of magnitud weaker than the weak force. This is why DM

745 is so difficult to detect. The SM does not provide a proper candidate but
746 searches are being carried.

747 The existence of DM has been inferred through gravitational effects in
748 astrophysical and cosmological observations. The rotational speed of the
749 galaxies, the gravitational lensing and the CMB angular spectrum are some
750 examples of phenomena that cannot be explained with general relativity
751 unless there is more present matter what it is seen.

752 **Naturalness**

753

754 **Hierarchy problem**

755

756 **Unification of the strong interaction**

757 There are unification attempts to treat all interactions as one, with the same
758 coupling constant and the same symmetry group ⁹. In the same way the EW
759 unifies QED and Weak forces, the grand unified theories (GUT) unifies all
760 three interactions (QED, Weak and QCD) of the SM at high energies, where
761 the coupling constants approach each other. Note that gravity is still left
762 out, because it is much weaker than the other interactions.

763 **Supersymmetry**

764 Originally motivated by the hierarchy problem, supersymmetry (SUSY) is
765 an extension to the SM. In SUSY the equations for force and the equations
766 for matter are identical and each SM particle has its supersymmetric partner
767 “sparticle” from which differs by half spin unit. Therefore, for each SM
768 fermion, the corresponding sfermion is a spin-0 scalar and hence a boson.
769 Identically, there is a super-partner for each of the SM bosons. The gluons
770 have the spin-half gauginos. The Higgs have a weak isospin doublet os spin-
771 half Higgsinos ($\tilde{H}_{1,2}^0$ and \tilde{H}^\pm). The new particles interact through the forces
772 of the SM but would have different masses

773 SUSY is not a theory but a principle and any theory with that property
774 is said to be supersymmetric. So, there is not one but dozens of supersym-
775 metric theories. A lot of focus has been put searching for supersymmetric
776 particles but so far the supersymmetric partners have not been found, which
777 is a good reason to be skeptical about SUSY.

⁹The most popular symmetry group for unification is $SU(5)$.

778 1.2 Top quark

779 The top¹⁰ quark (t) or, for simplicity, just top is the up-type quark of
 780 the third generation of fermions. Sometimes called truth quark, its most
 781 distinctive feature is its huge mass, which is the largest among all fundamental
 782 particle particles. Due to being so massive, its life time is very
 783 short ($\tau_t = 5 \times 10^{-25}$ s) and this represents a unique opportunity to study
 784 quarks in free state, something that is very rare due to colour confinement,
 785 as explained in Section 1.1.4.

786 The left-handed top is the $Q = 2/3$ and $T_3 = +1/2$ member of the weak
 787 isospin doublet that also contains the bottom quark. The right-handed top
 788 quark is the $SU(2)_L$ weak isospin singlet ($Q = 2/3$ and $T_3 = 0$).

- 789 - Window for new physics
- 790 - <https://twiki.cern.ch/twiki/bin/view/AtlasPublic/TopPublicResults>
- 791 - <https://pdg.lbl.gov/2020/reviews/rpp2020-rev-top-quark.pdf>

792 Work in progress

793 The most recent results for the top quark mass measurements result in $m_{top} = 172.76 \pm 0.30$ GeV [1]. This number is an average of
 794 the measurements at LHC with ATLAS (172.69 ± 66 GeV [52]) and CMS
 795 (172.6 ± 3.5 GeV at CMS [53]) and at Tevatron with CDF and D $\bar{\theta}$ (combined
 796 result: 174.30 ± 0.89 GeV [54]). These values are measured from the kin-
 797 ematics of $t\bar{t}$ events¹¹. Figure 1.9 summarises the measurements of ATLAS
 798 and CMS for m_{top} from direct top quark decay. Figure 1.10 presents the
 799 results for m_{top} measurements from $t\bar{t}$ observables.
 800

801 1.2.1 Top quark discovery

802 The existence of a third generation of quarks was proposed in 1973 by
 803 Kobayashi and Maskawa [55] to explain the \mathcal{CP} violations in kaon decays.
 804 The quarks of the new generation were named top and bottom to match
 805 the names of the up and down quarks. This prediction was based on the
 806 GIM mechanism, which predicted the existence of the yet unobserved charm
 807 quark. When the charm was observed [56], the GIM was accepted into the
 808 SM and the postulation of the third family and thus the top quark gained
 809 credibility. Shortly after the charm, the bottom quark was discovered in
 810 the E288 experiment at Fermilab [57], reinforcing the idea of the existence

¹⁰Here and in the following, the usage of the term top quark includes the top antiquark.

¹¹This m_{top} results are sensitive to the top quark mass used in the MC generator that is usually interpreted as the pole mass.

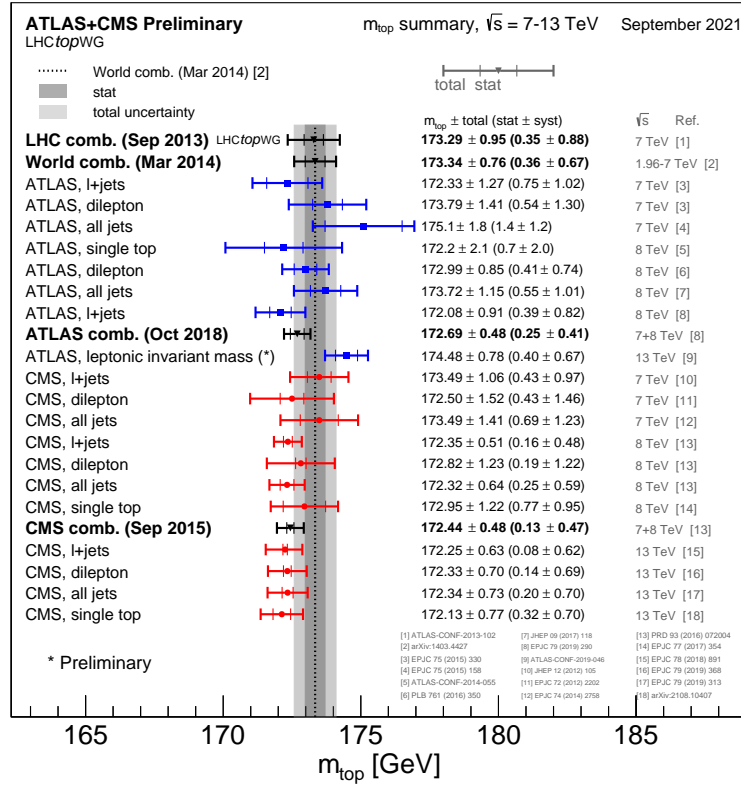


Figure 1.9: Summary of the ATLAS and CMS measurements from top quark decay. Results compared to LHC m_{top} combination.

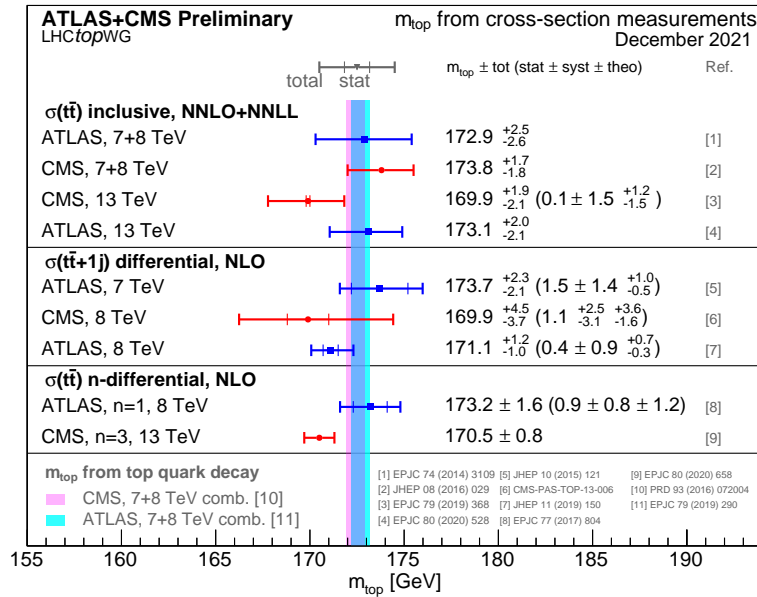


Figure 1.10: Summary of the ATLAS and CMS measurements from $t\bar{t}$ observables. Results compared to measurements from direct top quark decay.

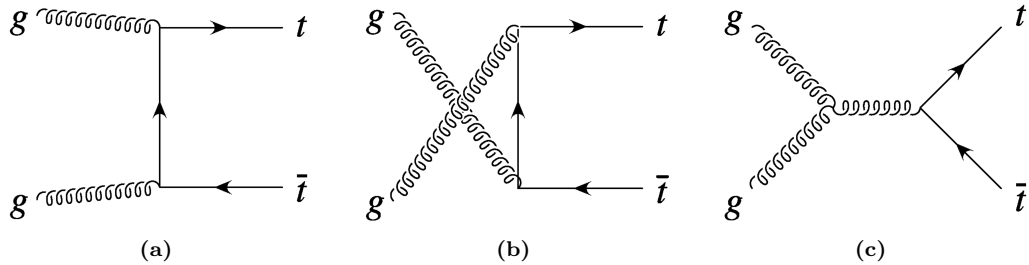


Figure 1.11: Representative Feynman diagrams of the LO processes contributing to the $t\bar{t}$ production via gluon fusion at LHC

of the top quark. However, due to its large mass, it took 18 years to confirm the existence of the top.

The top quark was observed for the first time at Tevatron with the CDF [58] and D \emptyset [59] detectors via flavour-conserving strong interaction in 1995. Back then and until the start of LHC Run-1, Tevatron was the only accelerator powerful enough to produce top quarks.

1.2.2 Top quark production at LHC

The LHC is sometimes referred as a top factory due to its ability to produce such a particle. In this collider, at pp collisions, the top quark is produced via two mechanisms: through QCD in top and anti-top pairs ($t\bar{t}$), and by means of the Wtb vertex of EW in single-top quarks associated with other particles.

1.2.2.1 Top pairs

The production top and anti.top pair of quarks is the largest source of production of top quarks in hadron collisions. This process is one of the most important at LHC because it allows to precisely study the properties of the top quark. Furthermore, the top quark pair production is also a major background in many searches for rare processes.

At LHC, the gluon fusion (Figure 1.11) dominates the $t\bar{t}$ production followed by the quark and anti-quark annihilation (Figure 1.12). Due to its primordial importance for the physics programme of LHC, the theoretical calculations for the $t\bar{t}$ production are done to an accuracy of next-to-next-to-leading order (NNLO) in QCD [60] and measured by ATLAS and CMS. Figure 1.13 shows the measurements for the $t\bar{t}$ production cross section ($\sigma_{t\bar{t}}$). The measurements and the theory calculations are quoted at $m_{top} = 172.5$ GeV.

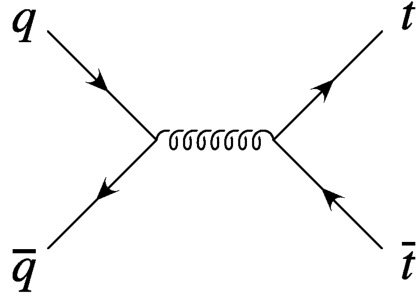


Figure 1.12: Representative Feynman diagrams of the LO processes contributing to the $t\bar{t}$ production at LHC through quark and anti-quark annihilation.

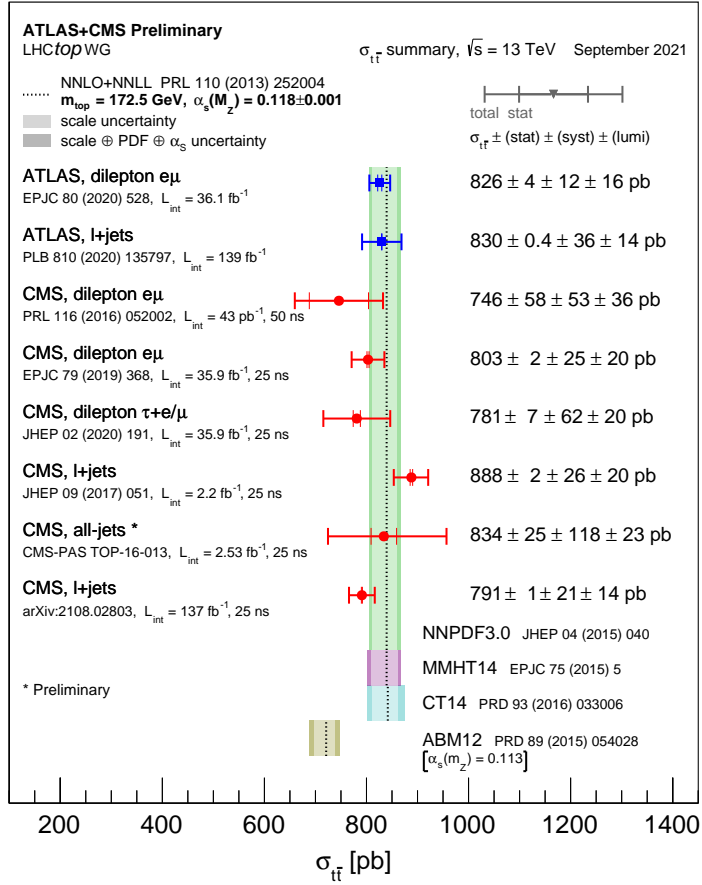


Figure 1.13: Summary of measurements $\sigma_{t\bar{t}}$ at 13 TeV compared to the exact NNLO QCD calculation complemented with NNLL resummation.

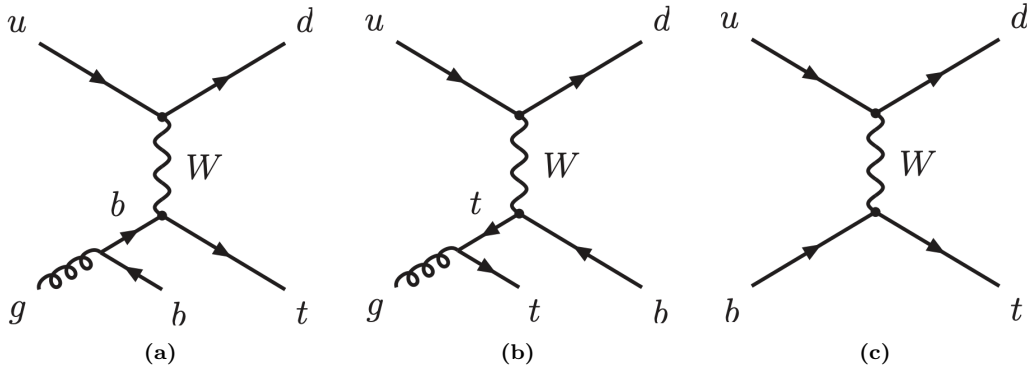


Figure 1.14: Representative Feynman diagrams for the single-top-quark production in the t -channel process.

837 1.2.2.2 Single top

838 In addition to the top pair production, the single-top-quark processes
 839 are of great importance to the study of the top quark properties at the LHC.
 840 This mechanism has a cross section three times smaller than that of $t\bar{t}$ and
 841 are almost exclusively produced through the electroweak Wtb vertex.
 842 This is precisely the reason why single-top-quark production is essential
 843 to gather information the Wtb interaction. The reason to decay and be
 844 produced from the bottom quark and not from strange or down quarks is
 845 because the CKM elements V_{ts} and V_{td} are much more smaller than V_{tb}
 846 being $|V_{tb}| = 0.99915$, $|V_{ts}| = 0.0403$ and $|V_{td}| = 0.00875$.

847 At LO, there are three production modes for single top, being the t -
 848 channel the dominant mechanism at the LHC with, approximately 70% of
 849 the single top quark cross section ($\sigma_{Single-t}$) at a $\sqrt{s} = 13$ TeV. The other
 850 processes are the s -channel and the associated production tW production.

851 **t -channel**

852 This production mode, involves the scattering of a light quark and a gluon
 853 from the proton sea as shown in Figure 1.14. Note that additional dia-
 854 grams to those in Figure 1.14 are obtained by either replacing the u and d
 855 by a c and s quarks or by switching the light quarks in the fermion line.
 856 The diagrams for antitop production are the charge conjugate of the ones
 857 presented.

The measurements cross sections at 13 TeV for single-top ($\sigma_{t-channel,t}$) and single-anti-top ($\sigma_{t-channel,\bar{t}}$) quarks in the t -channel production are shown in Figure 1.15. The theoretical calculations at NLO for $\sigma_{t-channel,t+\bar{t}}$

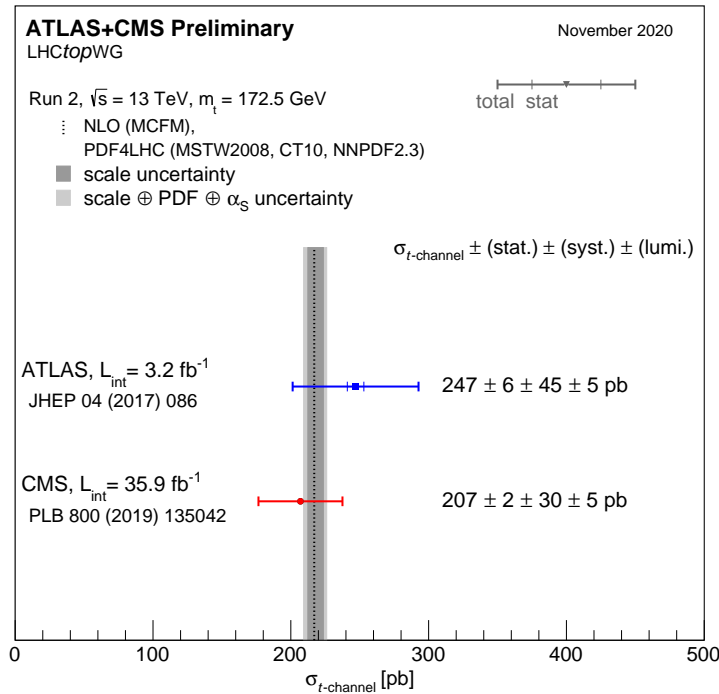


Figure 1.15: Summary of the ATLAS and CMS Collaboration measurements of the single top production cross-sections in the t -channel at 13 TeV.

at 13 TeV are:

$$\begin{aligned}\sigma_{t\text{-channel},t} &= 136^{+4.1}_{-2.9}(\text{scale}) \pm 3.5(\text{PDF} + \alpha_s) \text{ pb}, \\ \sigma_{t\text{-channel},\bar{t}} &= 81.0^{+2.5}_{-1.7}(\text{scale}) \pm 3.2(\text{PDF} + \alpha_s) \text{ pb}, \\ \sigma_{t\text{-channel},t+\bar{t}} &= 217^{+6.6}_{-4.6}(\text{scale}) \pm 6.5(\text{PDF} + \alpha_s) \text{ pb}.\end{aligned}$$

858 These numbers have been obtained using HATHOR 2.1 [61][62].

859 The dominant process in the SM is the one in diagram 1.14a, while
 860 the one in 1.14b is included in order to form a gauge invariant set but its
 861 contribution is not very significative since for the gluon is easier to decay to
 862 a $b\bar{b}$ pair than to a $t\bar{t}$ pair. These two $3 \rightarrow 2$ production modes are known as
 863 4 Flavour Scheme (FS) because the proton is considered to be composed by
 864 five quark flavours (u, d, c and s) and is characterised by having a b quark
 865 in the final state. This final state b quark is sometimes referred as second
 866 b and it has a transverse momentum (p_T) distribution peaking around 2 or
 867 3 GeV as can be seen in Figure 1.16. This is the reason why the final b
 868 quark from the gluon splitting frequently goes undetected, because it does
 869 not pass the p_T threshold of the detector.

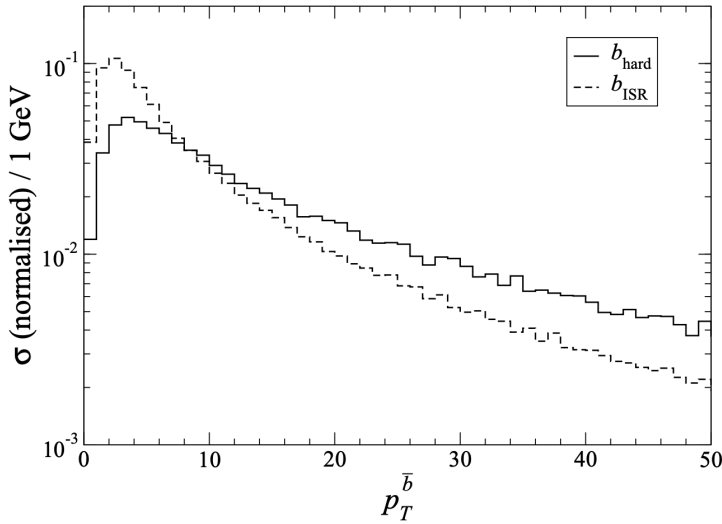


Figure 1.16: Normalised p_T distribution of the second b quark in the t -channel process, generated by Monte Carlo (MC) simulation [63].

870 The $2 \rightarrow 2$ process in 1.14c is known as 5FS because the proton is
 871 considered to be composed by five flavours of quarks (u, d, c and s) and it
 872 is characterised by having a b quark in the initial state. The simulations for
 873 the 4FS and 5FS diagrams are produced separately and merged afterwards.
 874 When adding the two contributions, some double-counting may appear due
 875 to the overlap in the phase space so one has to be careful.

s-channel

The s -channel process for single-top is the one with less impact among single-top production channels. It is depicted in Figure 1.17. According to the LHC cross section group, at 13 TeV of center-of-mass energy, the cross sections for the single top and single anti-top production in the s -channel ($\sigma_{s\text{-channel}}$) are:

$$\begin{aligned}\sigma_{s\text{-channel},t} &= 6.35^{+0.18}_{-0.15}(\text{scale}) \pm 0.9(\text{PDF} + \alpha_s) \text{ pb}, \\ \sigma_{s\text{-channel},\bar{t}} &= 3.97^{+0.11}_{-0.09}(\text{scale}) \pm 0.15(\text{PDF} + \alpha_s) \text{ pb}, \\ \sigma_{s\text{-channel},t+\bar{t}} &= 10.32^{+0.29}_{-0.34}(\text{scale}) \pm 0.27(\text{PDF} + \alpha_s) \text{ pb}.\end{aligned}$$

Associated tW

Finally, the associated production of a single top quark with a W boson (sometimes referred as tW -channel) is represented by two the Feynman diagrams in Figure 1.19. To these two diagrams, the charge conjugate processes could be added to complete the tW mechanisms. The cross section

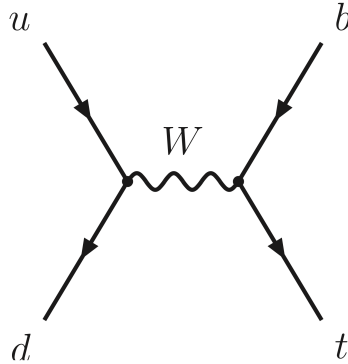


Figure 1.17: Representative Feynman diagram for the single-top-quark production in the s -channel.

for the associated tW signals:

$$\sigma_{tW,t+\bar{t}} = 71.7 \pm 1.80(\text{scale}) \pm 3.40(\text{PDF} + \alpha_s) \text{ pb.}$$

This and all σ in the section are calculated for a top mass of $m_{top} = 172.5 \text{ GeV}$ and NLO in QCD with HATHOR v.2.1. The PDF and α_s uncertainties are calculated using the PDF4LHC prescription [64] with the MSTW2008 68% CL NLO [65][66], CT10 NLO [67] and NNPDF2.3 [68] PDF sets, added in quadrature to the scale uncertainty.

1.2.3 Top quark decay

As advanced in the Section 1.2.2.2, due to the large V_{tb} element of the CKM matrix, the top quark decays almost entirely ($\sim 99.8\%$) through the medium of the Wtb vertex to a b quark and a W boson. The final state decay is classified according to the subsequent decay of the W boson. As W are massive vector bosons, its lifetime is very short ($\tau_W \approx 3 \times 10^{-25} \text{ s}$). For the W^+ , the decay modes are:

$W^+ \rightarrow e^+ \nu_e$	$(10.71 \pm 0.16)\%$
$W^+ \rightarrow \mu^+ \nu_\mu$	$(10.63 \pm 0.15)\%$
$W^+ \rightarrow \tau^+ \nu_\tau$	$(11.38 \pm 0.21)\%$
$W^+ \rightarrow q\bar{q}$ (hadrons)	$(67.41 \pm 0.27)\%$
$W^+ \rightarrow \text{invisible}$	$(1.4 \pm 2.9)\%$

For the conjugate processes involving the W^- , the branching ratios are the same. Therefore, the W decay and consequently the t decay can be classified either as leptonic or hadronic. The decay chain of the top quark is represented in Figure 1.20 Due to its large mass, the W can decay to any quark except the top quark.

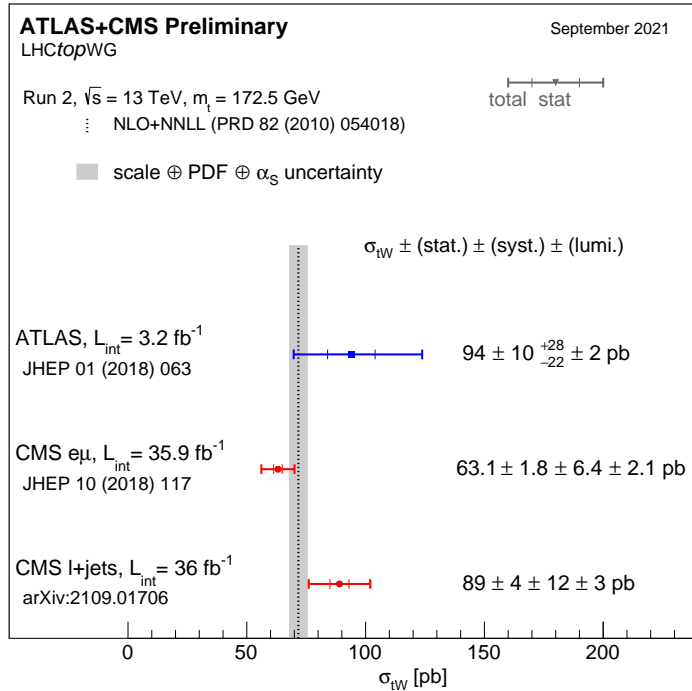


Figure 1.18: Cross-section measurements for the associated tW production boson performed by ATLAS and CMS at 13 TeV, and combined result compared with the NLO+NNLL prediction.

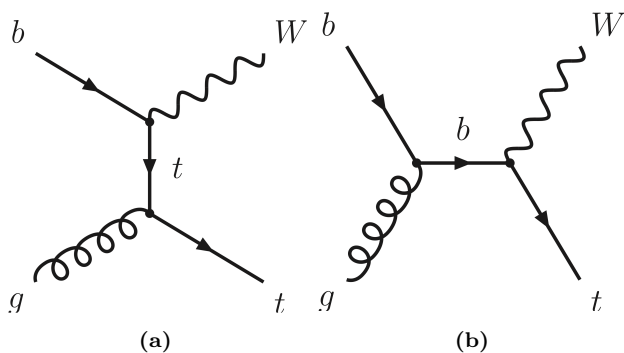


Figure 1.19: Representative Feynman diagrams for the single-top-quark production in association with a W boson.

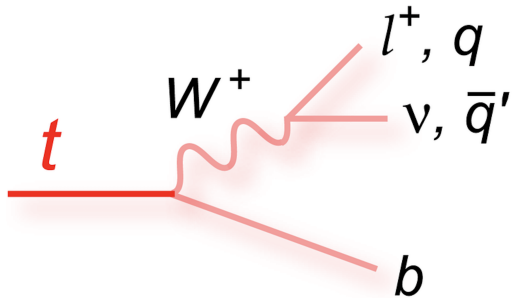


Figure 1.20: Decay of a top quark to a b quark and a W boson. The W boson can decay to two other quarks, making a jet triplet along with the b .

887 1.2.4 Top quark polarisation

888 1.2.5 Top quark physics

889 Probably this section is not necessary since the physics are
 890 gonna be explained above.

891 1.3 Higgs boson

892 Any particle physicist enthusiast remembers July 4th of 2012 pretty well,
 893 it was LHC experiments ATLAS and CMS who announced the discovery of
 894 new particle compatible with the SM Higgs boson. This discovery of the
 895 Higgs boson and, by extension, the Higgs field completed the SM.

896 Following the top quark, the Englert-Brout-Higgs-Guralnik-Hagen-
 897 Kibble-Higgs boson or, for simplicity, Higgs boson (H) or just Higgs is
 898 the most massive particle in the SM with a mass of $m_H = 125.25 \pm 0.17$
 899 GeV [2]. The value provided by [2] is an average of the ATLAS com-
 900 bined measurement ($m_H = 124.86 \pm 0.27$ GeV[69]) and the CMS results
 901 ($m_H = 125.46 \pm 0.16$ [70]).

902 The Higgs boson was the final piece in the SM puzzle. Its existence
 903 was theorised in 1964 by three independent groups: Englert-Brout [71],
 904 Higgs [72] and Guralnik-Hagen-Kibble [73], and its discovery meant one of
 905 the greatest successes of the SM. This theory was not only able to calculate
 906 with great precision the physics but also predicted the existence of a particle
 907 that was find later (see 1.3.2).

908 In the SM, fundamental particles acquire mass through their interactions
 909 with the Higgs fields. It is important to note that not all mass is related
 910 to the Higgs mechanism but, for instance, the mass of the proton does not

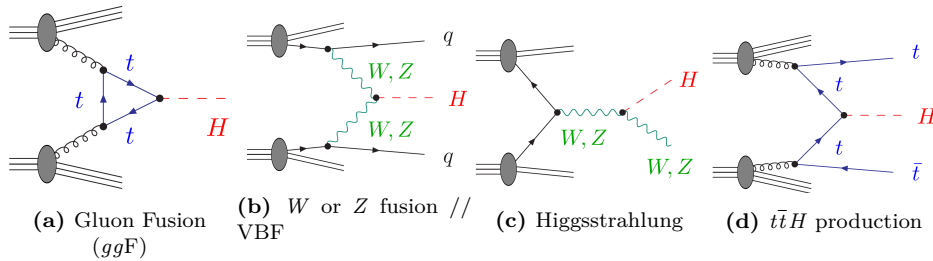


Figure 1.21: Lowest-order Feynman diagrams for the dominant production mechanisms of a Higgs boson at hadron colliders.

came from the interaction of its components with the Higgs but from the kinetic energy of the particles that compose the proton.

1.3.1 Higgs production and decay at LHC

H production

One of the reasons why the Higgs boson was found the latest among SM fundamental particles is because it is a fairly heavy particle and, hence, it was necessary a lot of energy to produce it. Even though that colliders such us SLAC or LEP had enough energy, they were colliding electrons and positrons and, since the coupling of the Higgs to fermions is proportional to the fermions mass, the process $e^- e^+ \rightarrow H$ processes is highly suppressed¹² and, for this reason, there were not enough statistics of events with a Higgs boson. The most favoured way of producing a Higgs boson is trough the mediation of the heaviest fundamental particles in the SM because these have the strongest couplings with the Higgs and, consequently, the greater cross section. Figure 1.21 shows the dominant mechanisms for Higgs boson production at the LHC.

Due to the abundance of gluons in pp collisions, the most dominant one, i.e. the one with largest cross-section, is the Higgs production via gluon fusion mediated by top quarks (Figure 1.21a). The second most important is the radiation by the incoming quarks of a W or Z vector bosons that fuse to from a Higgs (Figure 1.21b). There is another significant contribution involving the W or Z bosons, the Higgsstrahlung or associated WH or ZH production, a process in which the W or Z (formed from the annihilation of two quarks) radiate a Higgs boson(Figure 1.21c. The last major contribution to the Higgs production at the LHC is its productions in association with a pair of top and anti-top quarks (Figure 1.21d).

¹²The dominant Higgs production in $e^- e^+$ annihilation is the so called Higgsstrahlung, an s -channel process in which the H is produced in association to a Z boson similarly to Figure 1.21c.

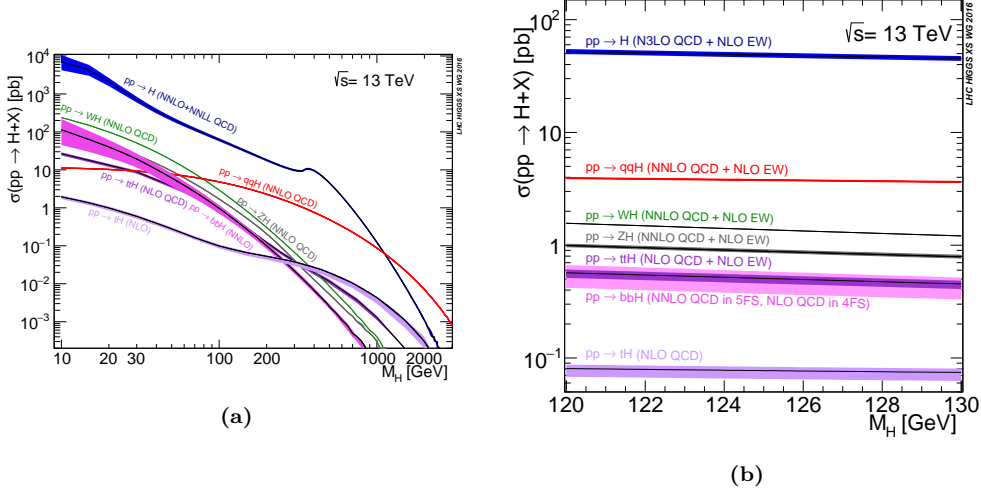


Figure 1.22: Higgs boson production cross sections as function of m_H at $\sqrt{s} = 13$ TeV.

937 The cross section of the different procedures for Higgs boson production
 938 at $\sqrt{s} = 13$ TeV are shown in Figure 1.22 as a function of m_H . For Figure
 939 1.22a, the σ_{tH} accounts for the t -channel and s -channel but not the tW -
 940 channel.

941 **H decay**

942 The Higgs boson have a very short lifetime ($\tau_H = 1.6 \times 10^{-22}$ s [74]) and,
 943 hence, is always detected through its decay products. The branching ratio
 944 (BR) is the fraction of particles which decay by an individual decay mode
 945 with respect to the total number of particles which decay and for the Higgs
 946 is shown in Figure 1.23.

947 The most prominent decay mode is the $H \rightarrow b\bar{b}$, which has a BR=58%,
 948 followed by the $H \rightarrow W^+ W^-$ with BR=21%. The relevance of each pro-
 949 duction and decay mode is portrayed in the pie charts of Figure 1.24.

950 1.3.2 Higgs boson discovery

951 The LHC experiments ATLAS [75] and CMS [76] discovered in 2012 a
 952 massive state H with the properties expected for the Higgs boson.

953 Both the ATLAS and CMS Collaborations reported excesses of events
 954 for 2011 ($\sqrt{s} = 7$ TeV and $\mathcal{L} = 4.8 \text{ fb}^{-1}$) and 2012 ($\sqrt{s} = 8$ TeV and $\mathcal{L} = 458 \text{ fb}^{-1}$)
 955 datasets of proton-proton collisions. This surplus of events was compatible
 956 in its production and decay with the SM Higgs boson in the mass region
 957 $m_H \in [124, 135]$ GeV with significances of 2.9σ for ATLAS and 3.1σ for
 958 CMS. At Tevatron (circular proton-antiproton collider at Fermilab), the

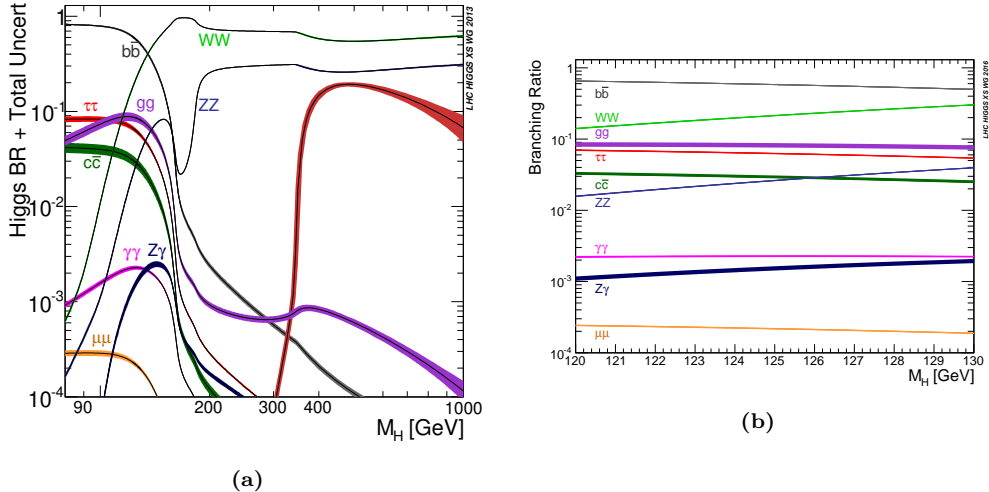


Figure 1.23: Standard Model Higgs boson decay branching ratios as function of m_H at $\sqrt{s} = 13$ TeV.

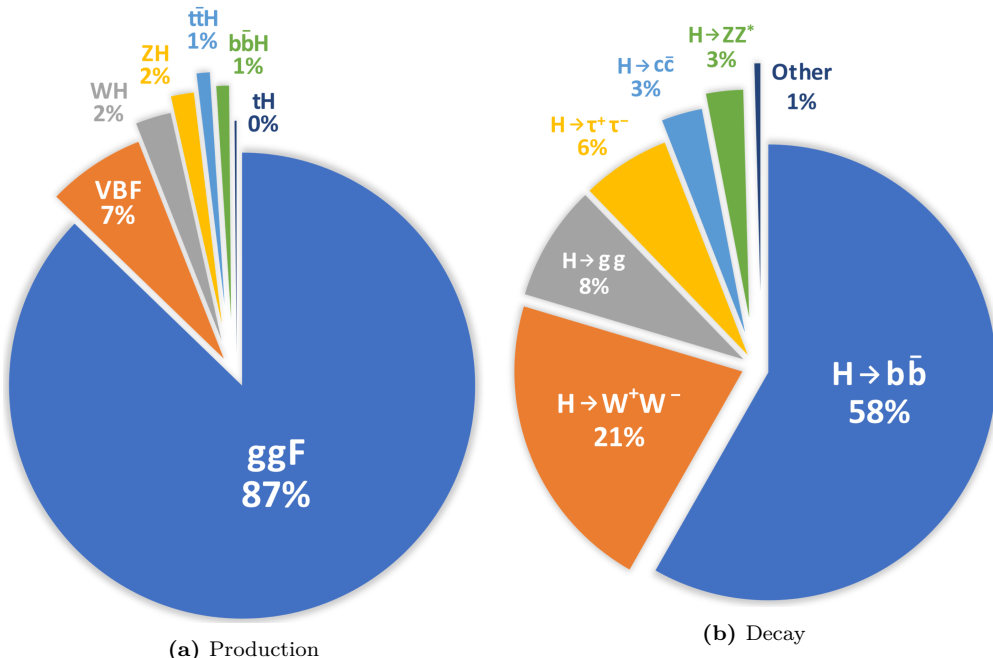


Figure 1.24: Percentage fractions for Higgs boson (a) production at $\sqrt{s} = 13$ TeV for pp collisions and (b) BR fraction for different decay channels [74].

959 experiments CDF [77] and D \emptyset [78] also reported an excess in the mass
 960 region $m_H \in [120, 135]$ GeV.

961 1.3.3 Higgs boson physics

962 Work in progress

963 The gauge symmetry is broken by the vacuum, triggering the
 964 EW Spontaneous Symmetry Breaking (SSB). This means that the sym-
 965 metry group of the EW sector, $U(2)_L \otimes U(1)_Y$.

$$966 \quad SU(3)_C \otimes SU(2)_L \otimes U(1)_Y \xrightarrow{\text{SSB}} SU(3)_C \otimes U(1)_{QED}$$

967 Production and decay rates, constrains on its couplings: [968 https://arxiv.org/abs/1606.02266](https://arxiv.org/abs/1606.02266)

969 The Higgs mass is given by $m_H = \sqrt{\lambda/2v}$, being v the vacuum expecta-
 970 tion value of the Higgs field and λ the Higgs self-coupling.

971 Electro weak symmetry breaking [79]: [972 https://arxiv.org/pdf/1512.08749.pdf](https://arxiv.org/pdf/1512.08749.pdf) In this paper the Yukawa coupling of the top is introduced, link
 973 it with the tHq paper.

974 Work in progress

975 1.4 Top quark and Higgs boson interplay

976 So far, the couplings of the Higgs boson to the SM particles have been
 977 found to be proportional to the mass of these particles. Since the top quark
 978 is the most massive particle and the coupling of Higgs to SM particles is
 979 uniquely determined by the mass of these particles, the Yukawa coupling
 980 between the top quark and the Higgs boson (y_t) is expected to be the
 981 greatest among all fermions and, hence, its study is of crucial importance,
 982 as it is discussed in references [80] [81] and developed in the succeeding
 983 sections.

984 The production of a pair or top quarks along with a Higgs boson ($t\bar{t}H$)
 985 it is possible to measure the absolute value of y_t . This process has the
 986 advantage of being the leading mechanism to produce the Higgs together
 987 with the quark top. At $\sqrt{s} = 13$ TeV it has a cross section of **poner cálculos**
 988 **del SM para $\sigma_{t\bar{t}H}$** (the definition of cross section can be found in Section
 989 2.2.5).

Despite having a very much lower cross section than $t\bar{t}H$ (**poner números**), the Higgs boson production alongside a single top quark (tHq or tH) brings valuable information, specially regarding the sign of the Yukawa coupling. Note that the sign of y_t is not physical by itself but the relative sign compared to the coupling of the Higgs to weak¹³ boson is, in deed, physical [80]. This is explored with more detail in 1.4.2.

A change in the Yukawa sign and/or absolute value with respect to its SM value would signal an origin of the fermion masses different from the described by the EWSB because the relative sign of the Higgs coupling to fermions and gauge vector bosons is crucial for recovering the unitarity and renormalizability of the theory s[82].

1001 All section 1.4 is work in progress

1002 $\rightarrow \mathcal{CP}$ Properties of Higgs Boson Interactions with Top Quarks in the
 1003 tH and $t\bar{t}H$ processes at ATLAS: <https://inspirehep.net/literature/1790698>

1005

1006 Only 1% of all Higgs bosons are produced in association with top quarks,
 1007 the observation of such processes is very challenging. Notably, it is a im-
 1008 mensely ambitious task to measure the associated production of a Higgs
 1009 with a single top which has an extremely low cross section as can be seen
 1010 in Figure 1.22b.

1011 1.4.1 $t\bar{t}H$

1012 The first associated production of a Higgs boson with a pair of top
 1013 quarks was observed in 2008 by ATLAS [83] and CMS [84]. This process
 1014 marked a significant milestone for the field of high-energy physics because
 1015 it helped establishing the first direct measurement of the tree-level coupling
 1016 of the Higgs boson to the top quark, which interacted with the predicted
 1017 strength.

1018 The associated production of H with top quark pair has been studied by
 1019 ATLAS and CMS previously during Run-1 at $\sqrt{s} = 7$ TeV and 8 TeV [85]
 1020 [86] and Run-2 [**buscar $t\bar{t}H$ en Run-2**]

¹³The coupling of the Higgs to the gauge bosons is taken as positive.

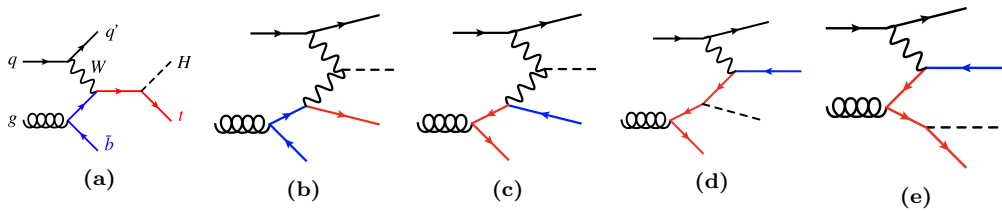


Figure 1.25: LO Feynman diagrams for t -channel tH production in the 4FS.

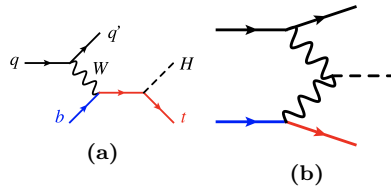


Figure 1.26: LO Feynman diagrams for t -channel tH production in the 5FS.

1.4.1.1 $t\bar{t}H$ Standard Model

1.4.1.2 $t\bar{t}H$ Charge-Parity

1.4.2 tH

tHq production modes

At LO, the production of a Higgs boson in association with a single top quark (tHq) in pp collisions is classified in three groups according to the virtuality of the W boson. These groups are: t -channel production, s -channel production and associated production with an on-shell W boson. This categorisation is the same as for the single-top-quark (Section 1.2.2.2), which makes sense since the tH associated production is, basically, a single-top-quark process in which a Higgs boson is radiated either from the W or the top.

In the t -channel production modes are classified in 4FS and 5FS as it is done for the single-top case. The 4FS and the 5FS modes are shown in Figures 1.25 and 1.26 respectively. For the 4FS modes, the diagrams in which the gluon decays to a top pair (1.25c, 1.25d and 1.25e) contribute less than the ones in which it does to a $b\bar{b}$ (1.25a and 1.25b).

Poner las tablas para las cross section de Demartin [87] para t -channel y s -channel

Since the s -channel contribution is so small to the total cross section of the tHq process,

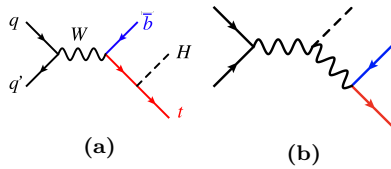


Figure 1.27: LO Feynman diagrams for s -channel tH production in the 5FS.

For tH and single-top-quark production at colliders, the 5FS calculations are easier than the 4FS due to the lesser final state-multiplicity and simpler phase space. This is why in the 5FS the single-top production is known at NNLO while the 4FS this is done only for NLO. Another advantage of the 5FS is that the t -channel, s -channel and associated tWH production do not interfere until NNLO. Contrary, the in 4FS, the t -channel at NLO and s -channel at NNLO can interfere. Nevertheless, this interferences are very small and can be neglected [87].

Poner algo in información del tWH prouduction mode para tH
y The tWH production is a background in the tHq analysis.

In reference 1.28 is shown that the shapes of the distributions of most observables in the s -channel differ significantly from those of the t -channel. So, even though the total cross section of the tHq production with the s -channel is much more smaller than the one for t -channel, one could think that including the s -channel in the analysis would increase the precision. This is not the case because the LHC is not sensible for to the tHq production via s -channel. In fact, not event the s -channel-single-top production (without any associated Higgs boson) has been found at LHC.

Summarise production modes described in [87]

tHq sensibility to y_t

As already commented in the introduction of the Section 1.4, the main interest of the tHq process is that it is among the few processes in the LHC that are sensible to the relative size and phase between the couplings of the Higgs top and the Higgs to the gauge bosons. The other mechanisms to determine this relative sign are $H \rightarrow \gamma\gamma$ and $gg \rightarrow ZZ$. This is due to the fact that in the SM the tHq production of the where the H couples to the W (Figure 1.28 right) interfere destructively with those in which the H is radiated from the top (Figure 1.28 left). As it is later explained in Section 2.2.5, the cross section is proportional to the square of the matrix element, \mathcal{M} and if there are several diagrams for a same process, the matrix elements have to be summed before squaring leading to interference terms. For the

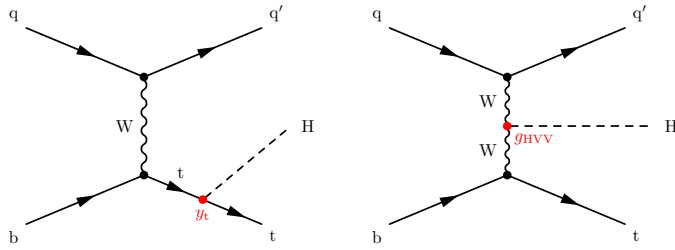


Figure 1.28: Representative LO Feynman diagrams for the t -channel tHq associated production, where the Higgs boson couples either to the top quark (left) or the W boson (right)

tHq production

$$\sigma_{tHq} \propto |\mathcal{M}_{qq \rightarrow tHq}|^2 = |\mathcal{M}_{qq \rightarrow tHq_{WH}} + \mathcal{M}_{qq \rightarrow tHq_{tH}}|^2 \quad (1.40)$$

When squaring the scattering amplitude, the destructive interference¹⁴ term decreases the σ_{tHq} . This behaviour makes the tHq cross section exceptionally sensible to the departures of y_t from the SM predictions. Typically, the destructive interference yields a reduction in the rate as compared to the contribution from each individual diagram by about an order of magnitude [88]. Therefore, in the presence of non-SM new physics, a positive relative sign between the tH and the WH couplings would imply that the amount of tHq events recorded should increase a factor of ~ 13 over the SM expectations, surpassing the $t\bar{t}H$ production [89].

The tHq production has been studied at LHC Run-1 by CMS [39]

Usar los papers the tHq de CMS la sección 5 de Demartin [87]

1.4.2.1 tH Standard Model

1.4.2.2 tH Charge-Parity

1.4.2.3 ATLAS and CMS results

In order to gather the necessary information, the widest possible campaign of measurements has to be undertaken, including all the different Higgs decay modes. In this context, the scope of this thesis is the study of the production tH with a final state characterised by two light leptons (ℓ), i.e. electrons (e^\pm) or muons (μ^\pm), and one hadronically decaying tau lepton (τ_{had}). This signature is usually referred as dileptau or lep-had channel and is denoted by $2\ell + 1\tau_{\text{had}}$.

¹⁴By destructive interference is meant that the relative sign between $\mathcal{M}_{qq \rightarrow tHq_{WH}}$ and $\mathcal{M}_{qq \rightarrow tHq_{tH}}$ is negative.

1082 **Chapter 2**

1083 **The ATLAS experiment at the
1084 Large Hadron Collider of
1085 CERN laboratory**

1086 The work developed in this thesis is framed in the context of the ATLAS
1087 detector, a general-purpose particle physics detector registering the events
1088 originated from the collisions produced by the largest and most powerful
1089 particle accelerator built up to this date, the LHC. This experimental setup
1090 is located in one of the largest and most renowned centres for scientific
1091 research in the world, the CERN.

1092 This chapter is devoted to the introduction of the CERN laboratory and
1093 a description of the technical design of LHC and ATLAS. The CERN or-
1094 ganisation is presented through an overview of its history, its achievements
1095 and some of the most relevant research projects carried out currently. The
1096 essential technical aspects of the LHC machine design are covered. The
1097 distribution and functioning of the accelerator complex and the main exper-
1098 iments conducted at LHC are summarised as well. Finally, a full overview
1099 of the different components of the ATLAS detector is exposed, presenting
1100 the specific features of each of its parts.

1101 **2.1 CERN**

1102 The European Organization for Nuclear Research, known as CERN, is
1103 the largest particle physics laboratory in the world. The convention estab-
1104 lishing CERN was ratified in 1954. Its name is derived from the French
1105 acronym *Conseil Européen pour la Recherche Nucléaire*, which was the pro-
1106 visional body designated in 1952 to foster the fundamental physics research

1107 in Europe, and the acronym has been maintained until CERN’s foundation.
1108 Initially formed by 12 member states, now it has 23 member states and
1109 many non-European countries involved in different ways such as associate
1110 members, partners and observers [90].

1111 The main site of the laboratory is located at Meyrin, a municipality of
1112 the Canton of Geneva (Switzerland), at the Franco–Swiss border. There
1113 are other sites in the vicinity of the Meyrin site, being the most relevant the
1114 Prévessin Site, the CERN’s second-largest site, straddling the communes of
1115 Prévessin-Moën (France).

1116 Since its beginning, CERN’s objective has been helping to uncover what
1117 the universe is made of and how it works. CERN started its first accelerator,
1118 the Synchrocyclotron, on 1957 and rapidly observed the electron decay of
1119 the pion for the very first time [91]. Thereafter, the laboratory has con-
1120 tinued contributing to not only particle and nuclear physics but also more
1121 technical fields. For instance, one of the most important achievements made
1122 through CERN experiments is the discovery in 1973 of neutral currents in
1123 the Gargamelle bubble chamber installed in the Proton Synchrotron (PS)
1124 [92]. This observation was an indirect evidence for the existence of the Z
1125 boson and ten years later, in 1983, CERN announced the discovery of the
1126 Z and W bosons [93]. This finding was done at the UA1 and UA2 ex-
1127 periments, located within the Super Proton Synchrotron (SPS), and it was
1128 awarded with the laboratory first Nobel Prize in 1984. Other major suc-
1129 cesses of CERN were the determination of the number of light neutrino
1130 families at the Large Electron-Positron Collider (LEP) on 1995 [94] and the
1131 creation for the very first time of antihydrogen atoms in 1995 at the PS210
1132 experiment [95]. More crucial accomplishment followed such as the discov-
1133 ery during the 1990’s of \mathcal{CP} violation by NA31 [96] and NA48 experiments
1134 [97]. And, in 2012, the Higgs boson discovery by ATLAS and CMS[75] [76],
1135 a fundamental test for the robustness of the SM as described in Section
1136 1.3.2. More recently, in 2015, a state consistent with a pentaquark was
1137 observed at LHCb [98].

1138 Currently, a wide diversity of projects are carried at CERN being the
1139 most renowned of them the LHC and its experiments which are described in
1140 more detail in Section 2.2. In addition, fixed-target experiments, antimatter
1141 experiments and experimental facilities make use of the LHC injector chain.
1142 The main fixed-target experiments at CERN are the Antiproton Decelerator
1143 (AD) [99] for slowing antiprotons for the antimatter factory [100] and the
1144 On-Line Isotope Mass Separator (ISOLDE) facility for short-lived ions [101].
1145 The world’s first proton-driven plasma wakefield acceleration experiment is
1146 also at CERN, the Advanced Proton Driven Plasma Wakefield Acceleration
1147 Experiment (AWAKE) [102]. In the International Space Station (ISS), the

1148 Alpha Magnetic Spectrometer (AMS) tries to observe dark matter [103].
1149 The research programme at CERN covers topics from the basic structure
1150 of matter to cosmic rays, and from the Standard Model to supersymmetry.

1151 Important breakthroughs and advances have been done by CERN on
1152 three main technical fields: accelerators, detectors and computing. Behind
1153 these three areas of technology, lies a great number of topics of expertise:
1154 cryogenics, ultra-high vacuums, particle tracking, radiation monitoring, su-
1155 perconductivity, plasma-physics and many more. Probably, the most pop-
1156 ular of the contributions is the invention of the World Wide Web (WWW)
1157 in 1989 at CERN facilities [104]. All of this proves the versatility and cap-
1158 ability of CERN as a contributor to science, technology and society.

1159 2.2 Large Hadron Collider

1160 In the mid of the decade of 1980, the plans for building the Large Hadron
1161 Collider (LHC) were started. At several high-energy physics workshops
1162 and conferences, the idea of assembling a machine able to reach multi-TeV
1163 energies was discussed. This instrument would allow physicists to search for
1164 the Higgs boson at all possible masses. In 1991 the Long-Range Planning
1165 Committee of CERN proposed the construction of the LHC as the best step
1166 forward in CERN's future [105]. The approval of the LHC project arrived
1167 in 1994 and in 1995 the Conceptual Design Report was published [106].
1168 Finally, on 10 September 2008, a beam of protons was successfully directed
1169 into the LHC pipes for the first time.

1170 A summary of the main parameters of LHC for pp collisions is pre-
1171 sented in Table 2.1. These parameters are shown for how the machine was
1172 designed, for Run-1 (2011-2012) and Run-2 (2015-2018) as well as the ex-
1173 pected parameters for Run-3 (2025-2027). The forecasted values for the
1174 High Luminosity (HL) LHC upgrade (after 2027) are exposed too.

1175 2.2.1 Machine design

1176 The LHC is a circular hadron accelerator with a circumference of 27 km.
1177 Located where once was the LEP collider, the accelerator used by CERN
1178 from 1999 to 2000 [107], the LHC tunnels are almost entirely outside the
1179 main site, being mainly on french territory. An overall schematic view of
1180 the LHC is shown in Figure 2.1.

1181 The LHC has two rings with ultra-high vacuum (to prevent collisions
1182 with gas molecules while moving through the accelerator) inside of which

Parameter	Design	Run-1	Run-2	Run-3	HL-LHC
Beam energy	7	3.5 - 4	6.5	7	7
Center-of-mass energy (\sqrt{s}) [TeV]	14	7 - 8	13	14	14
Bunch spacing [ns]	25	50	25	25	25
Bunch Intensity [10^{11} ppb]	1.15	1.6	1.2	up to 1.8	2.2
Number of bunches (n_b)	2800	1400	2500	2800	2800
Transverse emittance (ϵ) [μm]	3.5	2.2	2.2	2.5	2.5
Amplitude function at the interaction point (β^*)[cm]	55	80	30→25	30→25	dowm to 15
Crossing angle [μrad]	285	-	300→260	300→260	TBD
Peak Luminosity [$10^{34} \text{ cm}^2 \text{ s}^{-1}$]	1.0	0.8	2.0	2.0	5.0
Peak pileup	25	45	60	55	150
Nominal magnetic field (B) [T]	8.73	4.16 - 7.76	7.73	8.73	8.73
Injection energy [GeV]				450	
Circunference length [km]				26.7	
Radius [km]				4.24	
Number of dipole magnets				1232	
Length of dipole magnets [m]				14.3	
Number of quadripole magnets				395	
Total mass [tons]				27.5	

Table 2.1: Summary of main accelerator parameters for the LHC, showing the design values, and those used during Run-1 and Run-2, as well as the expected parameters for Run-3 and the HL-LHC.

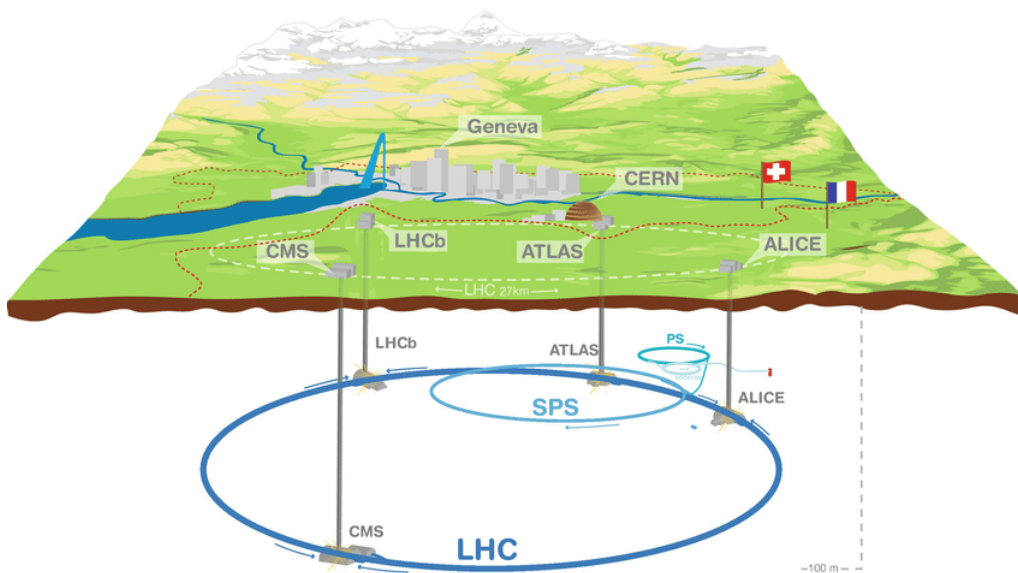


Figure 2.1: Overall view of the LHC including the ATLAS, CMS, ALICE and LHCb experiments.

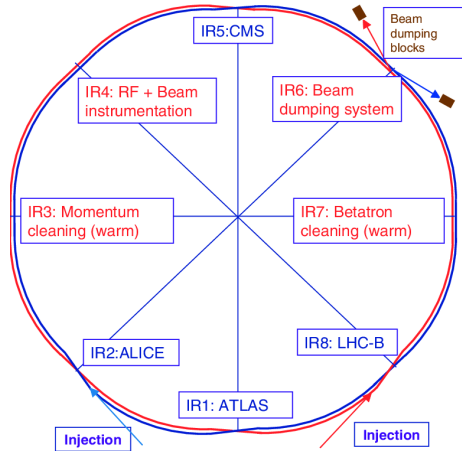


Figure 2.2: Schematic layout of the LHC (Beam 1 clockwise, Beam 2 anti-clockwise).

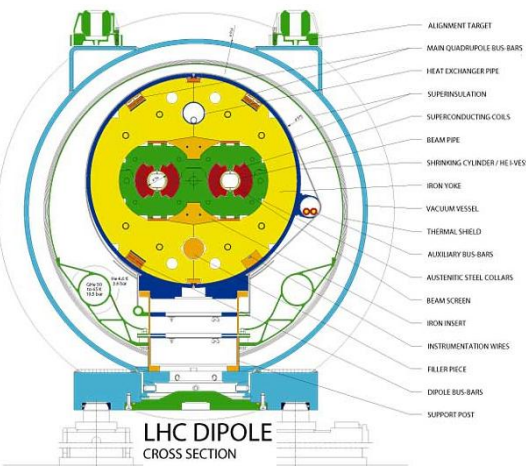


Figure 2.3: LHC dipole cross section.

1183 particle beams travelling in opposite directions. It was designed to accelerate and collide proton beams with a center-of-mass energy (\sqrt{s}) up to
 1184 14 TeV at a luminosity (\mathcal{L}) of $10^{34} \text{ cm}^2 \text{ s}^{-1}$ (see Section 2.2.5 for details
 1185 about luminosity). As well as protons, it can collide heavy ions, in partic-
 1186 ular lead nuclei, at $\sqrt{s} = 2.3 \text{ TeV}$ per nucleon and a peak luminosity of $\mathcal{L} = 10^{27} \text{ cm}^2 \text{ s}^{-1}$ [108]. These specifications make the LHC the accelerator
 1187 with higher collision energy [109].
 1188

1189
 1190 The beams in the LHC are made up of bunches of protons that are
 1191 spaced 7 m apart and collide every 25 ns. Each bunch contains 1.1×10^{11}
 1192 hadrons, being 2556 the maximum possible number of bunches that can be
 1193 reached with the beam preparation method currently used [110]. The size
 1194 of each bunch is 25 cm [111].
 1195

The LEP tunnel lies between 45 m and 170 m below the surface on a plane inclined at 1.4% sloping towards the Léman lake. The underground construction adds some shielding from outside interferences that could interact with the detectors and cause anomalous readings. Even 100 m underground, the cosmic rays can reach the detectors, so these are used to help to calibrate them. The tunnel has an internal diameter of 3.7 m, which makes it extremely difficult to install two completely separate proton rings [112] as in the Superconducting Super Collider (SSC). Therefore, the counter-rotating rings are built under the *two-in-one* twin-bore superconducting magnet design. These twin bore configurations have the disadvantage of having the rings magnetically coupled, which adversely affects flexibility [113]. Figure 2.3 shows an example of the LHC twin-bore dipole magnet.
 1196
 1197
 1198
 1199
 1200
 1201
 1202
 1203
 1204
 1205
 1206

The LHC is not a perfect circle. Approximately 22 km of the LHC ring consists of 8 curved sections. The remaining 5 km of the tunnel are made of 8 straight sections, denominated insertion regions (IR), that provide space for the experiments. Figure 2.2 shows the distribution of IR and crossing points for the LHC. This layout follows that of the LEP tunnel. The number of crossing points where the beams pass from one ring to the other for colliding was decreased from the original 8 at LEP to 4 in the LHC in order to reduce costs and optimise the utility insertions containing Radio Frequency (RF), the collimation and the beam dump systems [106].

The arcs contain the dipole bending magnets, which are shown in Section 2.3. The 1232 twin-bore magnets curve the trajectory of the particle beam that would, otherwise, follow a straight line. Dipoles are also equipped with additional multipole lattice magnets (sextupole, octupole and decapole), which correct for small imperfections in the magnetic field at the extremities of the dipoles.

Each of the 8 straight sections is approximately 528 m long. The RF cavities delivering 2 MV (an accelerating field of 5 MV/m) at 400 MHz are located in the IR4. The 16 RF cavities compensate the synchrotron radiation losses (the electromagnetic radiation emitted when charged particles travel in curved paths) that take place at the arcs of LHC. The energy radiated per particle by synchrotron radiation is proportional to the inverse of the mass of the particle: $\Delta E \propto 1/m^4$. This radiation is, thus, smaller for protons than for electrons. That is why the LHC machine has much less synchrotron radiation losses than LEP and its design would ideally have longer arcs and shorter straight sections for the same circumference. But using the tunnel as built for LEP was the cost-effective solution. During the 20 minutes that are needed to reach the beams maximum energy, the bunches have passed the RF cavities more than 10 million times [106].

The RF cavities (also known as resonators) are metallic chambers spaced at intervals along the accelerator shaped to resonate at specific frequencies, allowing radio waves to interact with passing particle bunches. The main role of the RF cavities is to keep the proton bunches tightly packed to ensure the required luminosity at the interaction point. They also transfer RF power to the beam to accelerate it to the top energy [114].

At the insertion of the arc and straight sections, quadrupole magnets are installed to suppress the dispersion of particles. Acting as focal lenses, quadrupole magnets gather the particles together. This system not only cancels the horizontal dispersion arising in the arc but also adapts the LHC reference orbit to the geometry of the LEP tunnel. Before entering the detectors, the inner triplets (which are made mostly from quadrupoles)

1247 tighten the beam, from 0.2×10^{-3} m down to 16×10^{-6} m. These are known
 1248 as insertion magnets.

1249 In total there are more than 9000 magnets all over the LHC and more
 1250 than 50 types of magnets are needed to make the particles circulate in
 1251 their path without losing speed. The coils are made of niobium-titanium
 1252 (NbTi) which is cooled to less than 2 K with superfluid helium to reach
 1253 superconductivity.

Of course, only stable charge particles¹ such as electrons, positrons, protons, antiprotons and some ions, can be accelerated by the magnetic fields described. The force that experiments a charged particle with charge q moving under a magnetic field B at a speed v is given by Lorentz law

$$\vec{F} = q \vec{v} \times \vec{B} \quad (2.1)$$

1254 and, since \vec{B} is perpendicular to \vec{v} , this force is always directed to the
 1255 center of the circle of radius r : $F = Bqv = m\frac{v^2}{r}$.

1256 2.2.2 Accelerator complex

1257 To accelerate the proton beams, the existing CERN accelerator complex
 1258 is used. These accelerators were, back in the day, the state of the art
 1259 colliders and now they serve as injection system for the LHC. The path
 1260 followed by the particle beams is presented in Figure 2.4. The accelerator
 1261 complex consists in several machines interconnected with higher and higher
 1262 capabilities, i.e. the beams are injected from one accelerator to the next in
 1263 sequence, boosting the particles to higher energies in each step until they
 1264 enter into the LHC.

1265 The proton bunches are produced ionising a gas of hydrogen atoms and
 1266 then they are accelerated to a momentum of 50 MeV by the linear accelerator
 1267 (LINAC2). Starting from Run-3, the LINAC2 is being replaced by the
 1268 LINAC4. After being produced, the beams enter into the first circular
 1269 accelerator, the Proton Synchrotron Booster (PSB) which has 630 m radius
 1270 and increases the energy of the protons until 1.4 GeV.

1271 The main advantage of circular accelerators compared to linear ones is
 1272 that they can speed up particles with much less physical space. Circular
 1273 accelerators ramp up two different beams with opposite charges at the same
 1274 time with a single magnetic field. The maximum energy transferred to the
 1275 beams in a circular accelerator is given by p_T [GeV] = $0.3qB[T]r[m]$, being

¹Long-lived particles such as the muon ($\tau \approx 2 \times 10^{-6}$ s) are discussed to be used on a muon collider [115].

1276 p_T the transverse momentum of the particles, q the charge of the particles
1277 ($q = 1$ for protons), B the magnetic field applied and r the radius of the
1278 circular accelerator.

1279 Right after the PSB, the Proton Synchrotron brings the particles 25
1280 GeV. The next step in the chain raises the energy to 450 GeV. This is done
1281 by the SPS, which is 6.9 km long. Once the protons have 450 GeV, the
1282 minimum energy at which the LHC can maintain a stable beam, they are
1283 injected into the LHC by two different 2 km-long Transfer Injection (TI)
1284 lines [116]. Protons will circulate in the LHC for 20 minutes until reaching
1285 the maximum speed and energy (650 GeV per beam) [113].

1286 Heavy-ion collisions were included in the conceptual design of the LHC
1287 from an early stage. Lead ions for the LHC are extracted from a source
1288 of vaporised lead and enter LINAC3 before being collected and accelerated
1289 in the Low Energy Ion Ring (LEIR). They, then, follow the same route to
1290 maximum acceleration as the protons [113].

1291 **2.2.3 LHC Experiments**

1292 In the LHC four major experiments are carried, each of them with its own
1293 detector (Figure 2.5). These particle detectors measure particles produced
1294 as debris from the pp collisions through the interaction with the material
1295 of the sub-detectors. Distributed along the collider as is shown in Figures
1296 2.1, 2.2 and 2.4, these highly sophisticated experiments are:

- 1297 • **A Toroidal LHC ApparatuS (ATLAS)** [117]: Located in the IR1,
1298 it is a generic multi-purpose experiment for high luminosity (up to
1299 $\mathcal{L} = 10^{34} \text{ cm}^2 \text{s}^{-1}$). It studies proton-proton collisions and investiga-
1300 tes a wide range of physics, from the search for extra dimensions
1301 to dark matter. It has the dimensions of a cylinder, 46 m long, 25
1302 m in diameter. The ATLAS detector weighs 7×10^3 tonnes. The
1303 design of the ALTAS detector features excellent jet and E_T^{miss} resolu-
1304 tion, particle identification and flavour tagging and standalone muon
1305 measurements. ATLAS will be covered in detail in Section 2.3.
- 1306 • **Compact Muon Solenoid (CMS)** [118]: Built inside the IR5, it's
1307 the other general-purpose experiment for high luminosity (same \mathcal{L} as
1308 ATLAS). CMS has the same objectives and goals as ATLAS but both
1309 its hardware and software designs are different. Even though CMS is
1310 smaller than ATLAS (21 m long, 15 m in diameter) it is much heavier,
1311 weighting 14×10^3 tonnes. The bulk of its weight is the steel yoke that
1312 confines the 4 T magnetic field of its superconducting solenoid. The

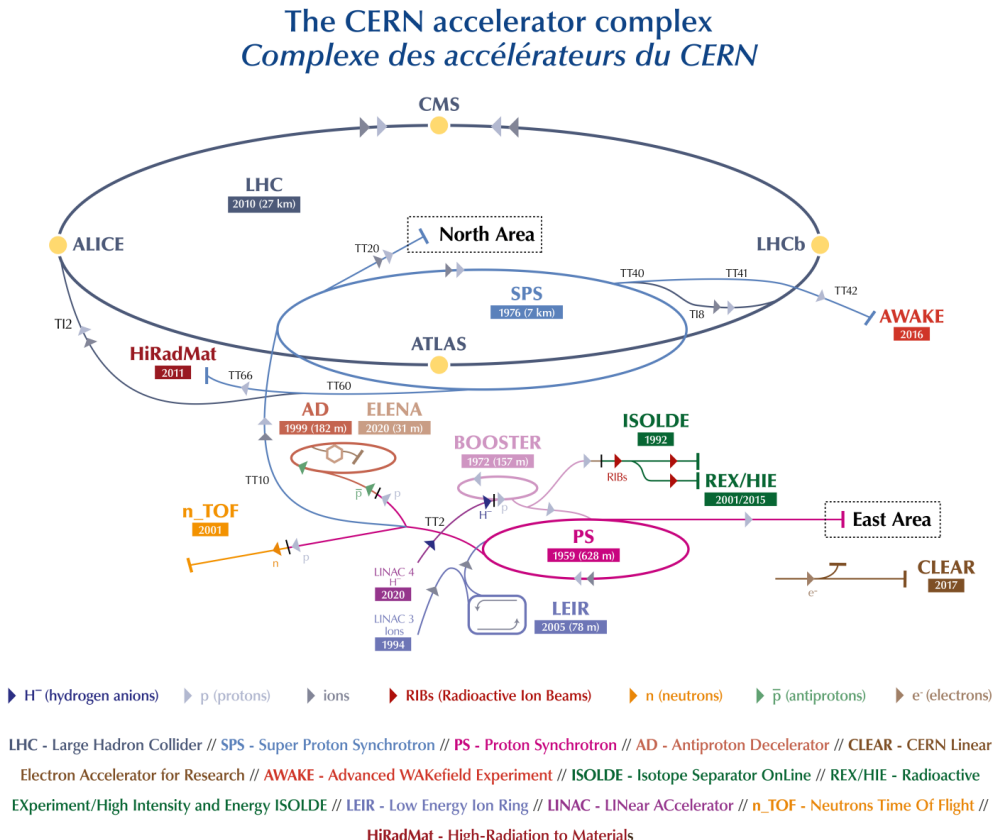


Figure 2.4: Scheme of CERN accelerator complex. Protons are injected from the LINAC2 into the PS Booster, then the PS, followed by the SPS, before finally reaching the LHC.

design of CMS emphasises magnificent electron/photon energy and momentum resolution. The role of coexistence of CMS and ATLAS is fundamental so that one can verify and confirm the experiments of the other independently.

- **Large Hadron Collider beauty (LHCb)** [119]: Hosted at IR2, it is a lower luminosity experiment designed to study the small asymmetries between matter and antimatter through \mathcal{CP} violation using rare decays of b -quark based hadrons. The detector is arranged as a succession of planar sub-detectors since most of the b -flavoured mesons follow the beam pipe direction when created in the proton-proton collision. LHCb delivers remarkable low-momentum track reconstruction and particle identification.
- **A Large Ion Collider Experiment (ALICE)** [120]: It is a low luminosity experiment in IR8 that focuses on QCD, the strong-

1327 interaction sector of the SM. The main feature of ALICE is a general-
 1328 purpose detector that it uses heavy-ion collisions to study matter in-
 1329 teracting at extreme densities and temperatures, thus reproducing the
 1330 quark-gluon plasma. This detector provides highly efficient track re-
 1331 construction in an environment full of heavy ions. Besides running
 1332 with Pb ions, the physics programme includes collisions with lighter
 1333 ions, lower energy collisions and a dedicated proton-nucleus run.

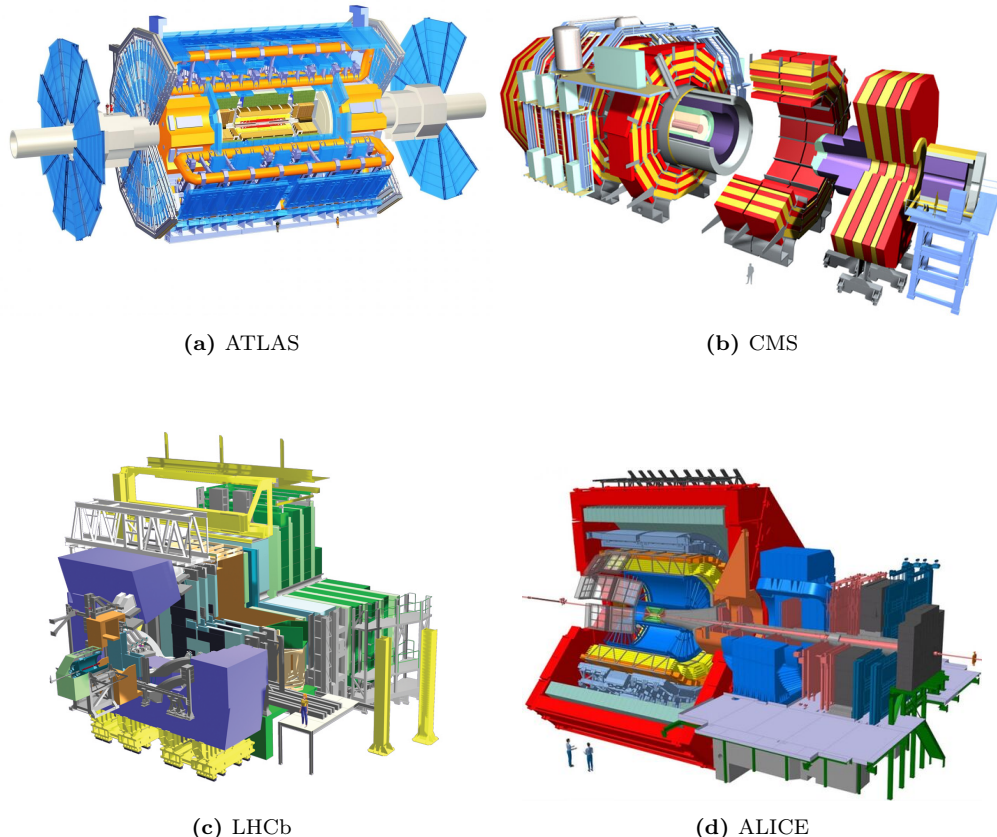


Figure 2.5: Scheme of LHC main experiments. Note that the images are not equally scaled.

1334 Along the LHC machine, there are other experiments much more smaller
 1335 than ATLAS, CMS, LHCb and ALICE, typically sharing the cavern with
 1336 the major projects. The most relevant among the minor experiments are:

- 1337 • **The Large Hadron Collider forward (LHCf)** [121]: Uses
 1338 particles thrown forward by collisions in the Large Hadron Collider
 1339 as a source to simulate cosmic rays in laboratory conditions. It shares
 1340 its cavern with the ATLAS detector [122].

- **The Massive Timing Hodoscope for Ultra Stable neutrAL pArticles (MATHUSLA)** [123]: Is dedicated large-volume displaced vertex detector for the HL-LHC on the surface above ATLAS or CMS for the search for neutral long-lived particles.
- **MilliQan** [124][125]: Consists on a small-scale detector experiment aiming to detect millicharged particles, i.e., particles with charges much smaller than that of the electron.
- **Monopole and exotic particle detector at the LHC (MoEDAL)** [126]: Deployed at LHCb cavern, it is optimised to detect highly ionising particles such as magnetic monopoles, dyons and multiple-electrically charged stable massive particles predicted in a number of theoretical scenarios.
- **TOTEM** [127]: Aims to measure the total cross-section of $p\bar{p}$ interaction using a luminosity-independent method and study elastic and diffractive scattering at the LHC. As CERN longest experiment, TOTEM detectors are spread across almost half a kilometre around the CMS interaction point.
- **ForwArd Search ExpeRiment (FASER)** [128][129]: Designed to search for new, yet undiscovered, light and weakly-interacting particles and study the interactions of high-energy neutrinos.

2.2.4 LHC Computing grid

The data collected by the different LHC experiments is stored, processed and, then, made available for all the researchers of each collaboration². This is possible thanks to the last piece of the LHC, its computing model and infrastructure: the LHC Computing Grid (LCG). It consists of several computing farms distributed around the world and interconnected. Figure 2.6 shows the geographical distribution of the different facilities that comprise the LCG. Just as the WWW enables access to information, the Grid enables access to computer resources. Employing a grid certificate, is possible for any user to run jobs on the grid and to access the data stored. The implementation of the grid model implies an effective coordination among all LHC collaboration centres [130].

Different types of computing centres have been defined and classified in Tiers [132]:

²Within the grid context, each collaboration is known as Virtual Organisation (VO).



Figure 2.6: Worldwide LHC Computing Grid geolocalisation of sites [131].

- **Tier-0:** This facility is located at CERN and it is responsible for archiving (first copy) and distributing the raw data received from the Event Filter, i.e., the data emerging from the Data Acquisition systems (DAQ) after the trigger. It provides prompt reconstruction and distributes a copy of the raw data to the Tier-1 centres.
- **Tier-1:** These facilities archive the raw data permanently and provide the computational capacity for reprocessing and for physical analysis. It also stores the simulated and reprocessed data. Currently, there are thirteen large computer centres serving as Tier-1 (see Figure 2.7). These make data available to their Tier-2 centres [133].
- **Tier-2:** Typically located at universities and other scientific institutes, there are more than 150 Tier-2 sites. The derived datasets produced by the physics groups are copied to the Tier-2 facilities for further analysis. The MC simulations for event production are executed at this level.
- **Tier-3:** The local computing resources, from local clusters to even just an individual PC are referred to as Tier-3. There is no formal engagement between worldwide LCG and the Tier-3.

This system provides near real-time access to LHC data. The LCG collaboration spreads out over 42 countries with 170 computing centres and 1 million computer cores, being the world's largest computer grid. It deals with over two million tasks daily. These specifications make the LCG the most sophisticated system for data taking and analysis ever built for science.

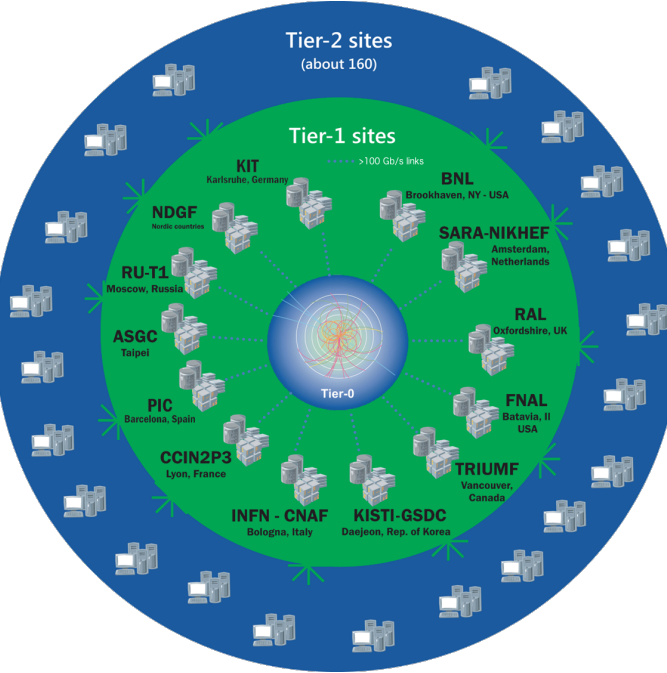


Figure 2.7: LCG Tiers [133].

1398 2.2.5 Energy, Luminosity and Cross section

1399 Energy

1400 Another name to refer to the field of Particle Physics is “high energy phys-
1401 ics”. Particles such as the Higgs boson or the top quark are more than 100
1402 times heavier than the proton so, in order to produce them, huge energies
1403 are required. The energy of the interaction, \sqrt{s} , allows the production of
1404 physical effects. The greater the energy is, the bigger is the range of the
1405 different processes that can be produced by the accelerator.

The four-vector, $\mathbf{p} = (E, \vec{p})$, of a particle of mass m describes its kinematics with its energy E and \vec{p} . The square of the four-vector, \mathbf{p}^2 , corresponds to the particle mass:

$$\mathbf{p}^2 = E^2 - \vec{p}^2 = m^2 \quad (2.2)$$

When two particles of mass m_1 and m_2 and momentums \vec{p}_1 and \vec{p}_2 collide, the center of mass energy, \sqrt{s} , can be expressed as:

$$s = E_{CM}^2 = (\mathbf{p}_1 + \mathbf{p}_2)^2 = (E_1 + E_2)^2 - (\vec{p}_1 + \vec{p}_2)^2 \quad (2.3)$$

For symmetric colliding beams, such those of LHC, the collision point is at rest in the laboratory frame ($\vec{p}_1 = -\vec{p}_2$) and, hence, the energy is

$$s = E_{CM}^2 = (E_1 + E_2)^2 \quad (2.4)$$

¹⁴⁰⁶ Since the energy of each beam is 650 GeV during Run-2, the center of mass
¹⁴⁰⁷ energy of LHC collisions is

$$\sqrt{s} = E_{CM} = (E_{beam1} + E_{beam2}) = 650 \text{ GeV} + 650 \text{ GeV} = 13 \text{ TeV} \quad (2.5)$$

When LHC is used for fix target experiments, one of the particles in the collision is at rest ($\vec{p}_2 = 0$) and the equation 2.3 writes as:

$$E_{CM}^2 = (m_1^2 + m_2^2 + 2m_2 E_{1,lab}) \quad (2.6)$$

Then, the energy for a proton-proton fix target collision with one beam at 650 GeV is

$$\begin{aligned} E_{CM}^2 &= (m_p^2 + m_p^2 + 2m_p E_{beam}) \\ &= 2(0.938 \text{ GeV})^2 + 2 \cdot 0.938 \text{ GeV} \cdot 650 \text{ GeV} = 1221.2 \text{ GeV}^2 \quad (2.7) \\ E_{CM} &= 34.9 \text{ GeV} \end{aligned}$$

¹⁴⁰⁸ This shows why colliding beams are essential to achieve high center of mass
¹⁴⁰⁹ energies.

¹⁴¹⁰ **Luminosity**

¹⁴¹¹ Besides \sqrt{s} , the luminosity is the most relevant parameter in an experiment,
¹⁴¹² especially in searches for events with small cross section. It measures the
¹⁴¹³ ability of the particle accelerator to produce enough events of the desired
¹⁴¹⁴ type.

The luminosity, \mathcal{L} , is the ratio of events detected in a certain period of time for a given cross section (σ):

$$\mathcal{L} = \frac{1}{\sigma} \frac{dN}{dt} = \frac{1}{\sigma} R \quad (2.8)$$

¹⁴¹⁵ where N is the number of the events and t the time. $R = \frac{dN}{dt}$ is known as
¹⁴¹⁶ reaction rate. It can be understood as number of particle collision per unit
¹⁴¹⁷ area (typically expressed in cm^2) and per second, therefore it is measured
¹⁴¹⁸ in $\text{cm}^2 \text{s}^{-1}$ [134]. For instance, for LEP was $\mathcal{L}_{LEP} = 1.0 \times 10^{32} \text{ cm}^2 \text{s}^{-1}$
¹⁴¹⁹ and the LHC is designed to achieve $\mathcal{L}_{LHC_{pp}} = 2.1 \times 10^{34} \text{ cm}^2 \text{s}^{-1}$ in pp
¹⁴²⁰ collisions and $\mathcal{L}_{LHC_{PbPb}} = 6.1 \times 10^{27} \text{ cm}^2 \text{s}^{-1}$ for heavy ion collisions.

For two beams colliding, the instantaneous luminosity is proportional to the number of bunches per beam (n_1 and n_2), the revolution frequency (f) with which the bunches are crossing and the number of proton bunches in

the machine (n_b), and it is and inversely proportional to the beams effective transverse area in which the collision takes places (Area = $4\pi\sigma_x\sigma_y$)

$$\mathcal{L} = f \cdot \frac{n_1 n_2 n_b}{4\pi\sigma_x\sigma_y} \cdot F(\theta_c, \sigma_x, \sigma_z) \quad (2.9)$$

where $F(\theta_c, \sigma_x, \sigma_z)$ is a factor accounting for the luminosity reduction due to the beam crossing angle (θ_c). At the LHC, assuming that the particles travel at the speed of light, for its 27 km, the bunch crossing frequency is $f = 11245.5$ Hz. The maximum number of proton bunches in the machine with 25 ns slots is³ $n_b = 2808$. In each bunch there are $n_1 \approx n_2 \approx 1.15 \times 10^{11}$ particles. Finally, characterising the optics of the collision at the interaction point (IP), the RMS transverse beam width in the horizontal and vertical directions are $\sigma_x \approx \sigma_y \approx 12, \dots, 50 \mu\text{m}$. The expression 2.9 assumes that the particles in the beam are Gaussian distributed. According to equation 2.9 the instantaneous luminosity only depends on the machine and its beam parameters [135][136].

The integrated luminosity over time is given by

$$L = \int \mathcal{L} dt \quad (2.10)$$

and it is used to determine the number of events, N , that have taken place during that time: $N = \sigma \times L$. The ability to observe low cross-section events is

$$N_{events}^{obs} = \sigma_{process} \times \text{efficiency} \times L \quad (2.11)$$

, where the efficiency of the detection is to be optimised by the experimental physicist, the integrated luminosity (L) is delivered by LHC and the cross section of the process ($\sigma_{process}$) is given by nature.

On one hand, several factors can limit the maximum luminosity that can be achieved at LHC [134]:

- **Beam-beam effect:** The bunches of two beams or the particles in the same bunch can interact electromagnetically, this leads to distortions from the orbit and results in an increase of the emittance, ϵ .
- **Crossing angle:** Often used to avoid unwanted collisions in machines with many bunches, due to the crossing angle θ_c , the luminosity is reduced by a factor $F(\theta_c, \sigma_x, \sigma_z) = \sqrt{1 + (\theta_c \sigma_z / 2\sigma x)^2}$.
- **Beam offset:** Originated from the beam-beam effects or misalignments in the quadrupole magnets, the beams can collide with small

³The theoretical maximum of 3564 bunches cannot be reached due to space needed between bunch trains and for the beam dump kicker magnets.

Year		2015	2016	2017	2018
Peak instantaneous luminosity ($\times 10^{33}$ cm 2 s $^{-1}$)	5	13	16	19	
Total delivered integrated luminosity (fb $^{-1}$)	4.0	38.5	50.2	63.4	

Table 2.2: Peak luminosity and total integrated luminosity delivered by the LHC at $\sqrt{s} = 13$ TeV in Run-2 per year [138].

1445 transverse offset. Such beams' offsets induce a loss of \mathcal{L} at the interaction point.
 1446

- 1447 • **Hourglass effect:** Appears when beams collide in a point away from
 1448 the IP.

1449 On the other hand, there are diverse strategies to maximise the luminosity delivered by a machine [135]:
 1450

- 1451 • **Maximise the total beam current:** Improvements in beam col-
 1452 limation, cryogenics vacuum and background protection could extend
 1453 the limit on the maximum beam current.
 1454 • **Compensate reduction factor:** The hourglass effect may be re-
 1455 duced by shorter bunches at the expense of a higher longitudinal pileup
 1456 density (see Section 2.2.6).

1457 The cumulative luminosity delivered by LHC to ATLAS during the Run-
 1458 2 per year is shown in Figure 2.8. In Figure 2.9, the total Run-2 cumulative
 1459 luminosity is presented differentiating between the delivered and recorded
 1460 luminosity and showing that almost all delivered events are considered to
 1461 be good data quality. The delivered luminosity accounts for the luminosity
 1462 given from the start of stable beams until the LHC requests ATLAS to
 1463 put the detector in a safe standby mode to allow a beam dump or beam
 1464 studies. The recorded luminosity reflects the DAQ inefficiency, as well as
 1465 the inefficiency of the so-called “warm start”: when the stable beam flag is
 1466 raised, the tracking detectors undergo a ramp of the high-voltage and, for
 1467 the pixel system, turning on the preamplifiers. The All Good Data Quality
 1468 criteria require all reconstructed physics objects to be of good data quality
 1469 [137].

1470 Cross section

1471 The cross section is a metric of the likely is a particular reaction to occur.
 1472 The higher the cross section is for a process, the more probable is for it to

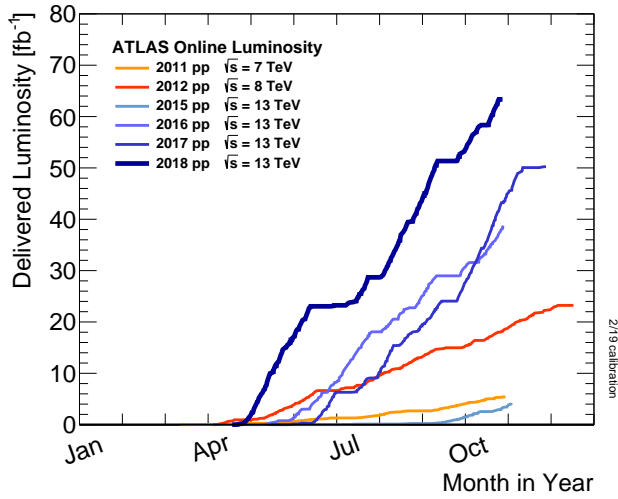


Figure 2.8: Cumulative luminosity versus day delivered to ATLAS during stable beams and for high energy pp collisions.

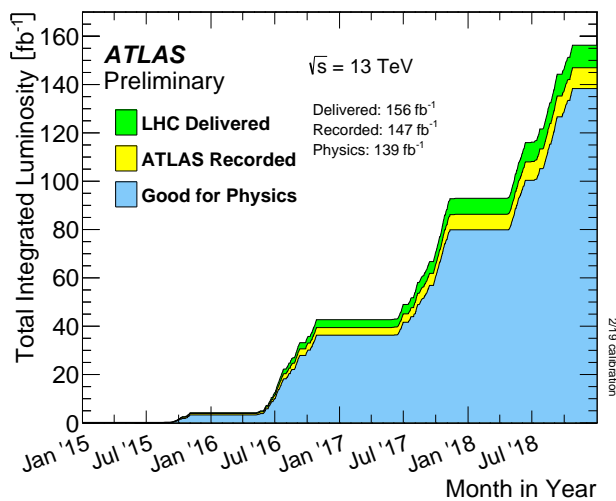


Figure 2.9: Total cumulative luminosity versus time delivered to ATLAS (green), recorded by ATLAS (yellow) and certified to be good quality data (blue) during stable beams for pp collisions at $\sqrt{s} = 13 \text{ TeV}$.

¹⁴⁷³ take place. Denoted by σ , it is measured in units of area named barns: 1
¹⁴⁷⁴ barn = $b = 10^{-24} \text{ cm}^2$. For instance, for the LHC energy:

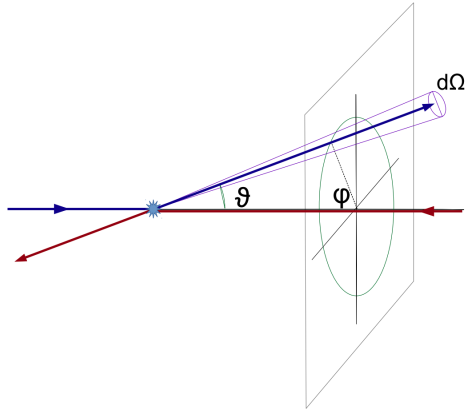
- ¹⁴⁷⁵ • $\sigma(pp \rightarrow X) \approx 0.1 \text{ b}$
- ¹⁴⁷⁶ • $\sigma(pp \rightarrow X + H) \approx 1 \times 10^{-11} \text{ b}$
- ¹⁴⁷⁷ • $\sigma(pp \rightarrow X + H; H \rightarrow \gamma\gamma) \approx 50 \times 10^{-15} \text{ b}$

¹⁴⁷⁸ In experiments with rotational symmetry, such as ATLAS, it is usual to
¹⁴⁷⁹ define the differential cross section ($\frac{d\sigma}{d\Omega}$) as the cross section per solid angle.
¹⁴⁸⁰ If the differential cross section is integrated over corresponding the angular
¹⁴⁸¹ range, the cross-section for a specific region (σ_ϑ) is obtained:

¹⁴⁸²

$$\sigma_\vartheta = \int_0^\vartheta \int_0^{2\pi} \frac{d\sigma}{d\Omega} \sin(\vartheta) d\phi d\vartheta$$

¹⁴⁸² with $\vartheta \in [0, \pi]$ is the coverage of
the scattering angle.



The total cross section is determined by the matrix element \mathcal{M} , which is independent of the experimental setup. The \mathcal{M} , also known as scattering amplitude, relates the initial state and the final state of a physical system undergoing a scattering process. Using \mathcal{M} , the total cross section for a process is determined by:

$$\sigma_{tot} = \int \frac{d\sigma}{d\Omega} d\Omega = \int \frac{1}{\Phi} |\mathcal{M}|^2 dQ$$

¹⁴⁸³ being Φ the incident particle flux in the process and the parameter dQ
¹⁴⁸⁴ describes the kinematic phase space.

¹⁴⁸⁵ 2.2.6 The Pile-up effect

¹⁴⁸⁶ Pile-up is a challenging matter among detectors and for the acquisition
¹⁴⁸⁷ and analysis of the data. In particle physics, pile-up is called to the situation
¹⁴⁸⁸ where the detector is being affected by several events at the same time.

¹⁴⁸⁹ Even though the bunches are composed by $\sim 10^{11}$, there are only around
¹⁴⁹⁰ 30 collisions per crossing with nominal beam currents. The mean number

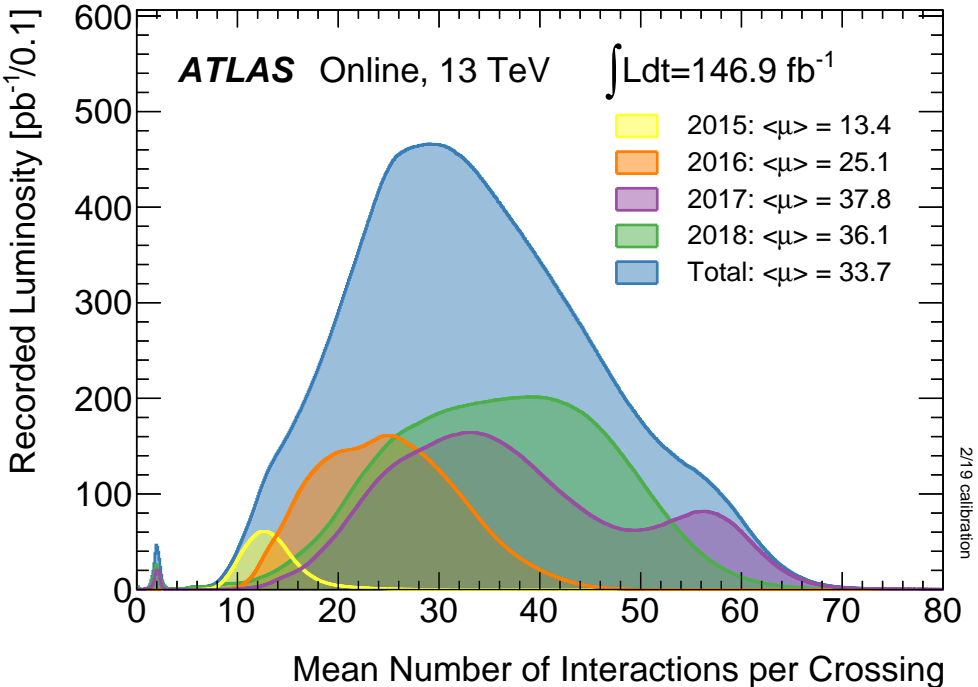


Figure 2.10: Luminosity-weighted distribution of the mean number of interactions per crossing $\langle \mu \rangle$ for Run-2 with pp collisions data.

of interactions per bunch crossing is presented in Figure 2.10 for each year of Run-2. The data shown in Figure 2.10 is recorded by ATLAS during stable beams at $\sqrt{s} = 13$ TeV. The mean number of interactions per crossing corresponds to the mean of the poisson distribution of the number of interactions per crossing calculated for each bunch. It is calculated from the instantaneous per bunch luminosity as $\langle \mu \rangle = \mathcal{L}_{bunch} \times \sigma_{inel}/f_r$ where \mathcal{L}_{bunch} is the instantaneous luminosity per bunch, $\sigma_{inel} = 80$ mb is the inelastic cross section of pp collisions at 13 TeV and $f_r = 11.245$ kHz is the LHC revolution frequency.

Work in progress

2.2.7 Phenomenology of proton-proton collisions

During LHC Run-2 data taking period, the protons were colliding at a center-of-mass energy $\sqrt{s} = 13$ TeV. The pp total cross section at this energy is measured to be $\sigma_{tot} = (110.6 \pm 3.4)$ mb [139]. The luminosity-independent method used to measure σ_{tot} allows to split the cross section into elastic and inelastic cross sections, $\sigma_{el} = (31.9 \pm 1.7)$ mb and $\sigma_{inel} = (79.5 \pm 1.8)$ mb respectively.

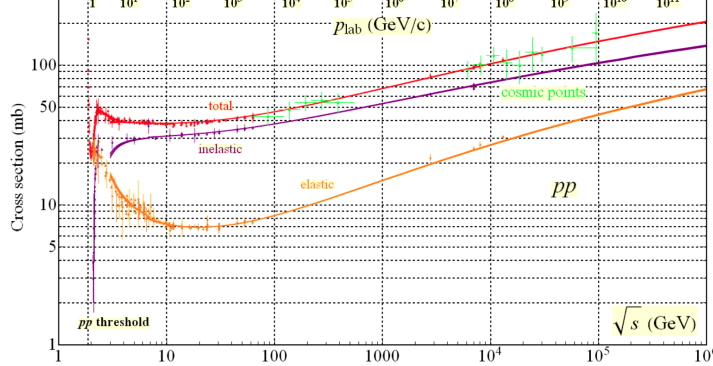


Figure 2.11: Total and elastic cross section for pp collisions as a function of the laboratory momentum and the \sqrt{s} [140].

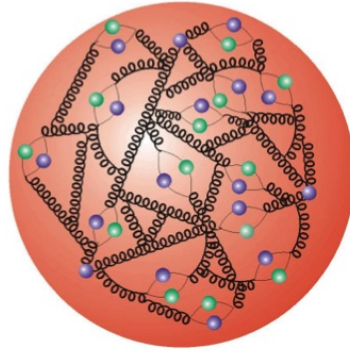
1508

Work in progress

1509

2.2.7.1 Proton structure

1510



The parton model for hadrons describes these non-fundamental particles as a composite of a number of point-like constituents named partons. The proton is not only simply made of three quarks ($u u d$, these are the so called “valence” quarks) but also, there is a “sea” of gluons and short-lived quark and anti-quark pairs. The sea partons are continuously interacting with each other and can have any flavour.

1511

The parton distribution functions (PDFs) are density functions that describe probability to find a parton carrying a fraction x of the total proton momentum at a squared energy scale Q^2 . The PDFs are essential to describe the pp interactions because these collisions cannot be understood as point-like particles crashing. Instead, all the constituents of the protons are taken into account [64].

1517

The momentum distribution function of the partons within the proton is obtained by a fit on a large number of cross section data points over a grid of x and Q^2 values obtained from many experiments. There are various global fitting collaborations (ABM, CT, MMHT, NNPDF), each taking different approaches to this fitting procedure. The PDF $f_{a/A}(x, Q^2)$ is defined as the probability of finding a parton a within the hadron A carrying a fraction $x = p_a/p_A$ of its momentum at Q^2 energy scale.

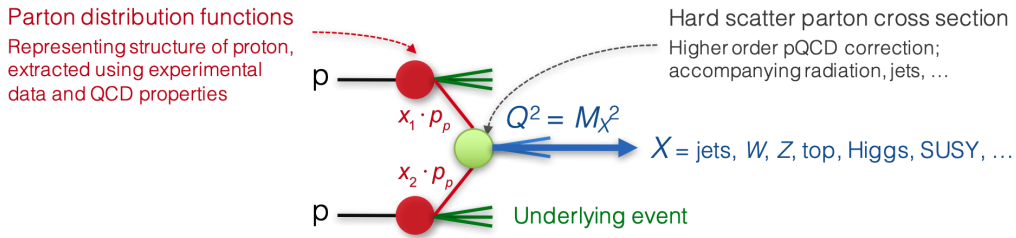


Figure 2.12: Simplified view of a pp collision [135].

1524 **Work in progress**

1525 2.3 ATLAS

1526 Installed in its experimental cavern at point 1, ATLAS is the largest de-
 1527 tector ever constructed for a particle collider with its 46 metres long and 25
 1528 metres in diameter. It is designed to record events of high-energy colliding
 1529 particles at high luminosities. The thousands of millions of interactions that
 1530 take place at the centre of the ATLAS detector are recorded and processed
 1531 by the different sub-detectors, which are composed by more than 100 mil-
 1532 lion sensitive electronic channels. Each ATLAS sub-detector is sensible to a
 1533 different type of particle and to different properties. Therefore, the layered
 1534 structure allows for effective particle identification, as well as enables accu-
 1535 rate measurements of energy and momentum. Figure 2.13 shows an overall
 1536 layout of the ATLAS detector and identifies its different sub-detectors. In
 1537 the picture can be appreciated that the cylindrical shape of ATLAS is di-
 1538 vided into two parts: the barrel (curved parts) and the end-caps (bases).
 1539 In the barrel region, the sub-detectors are built as coaxial layers around the
 1540 beam pipe (see memo 2.14). As one moves away from the axis, it finds the
 1541 Inner Detector (ID), the solenoid magnet, the Electromagnetic (ECAL) and
 1542 Hadronic (HCAL) Calorimeters, and the Muon Spectrometer (MS) in the
 1543 outermost layer. The technical details of these sub-detectors are presented
 1544 in the coming sections.

1545 ATLAS is able to explore a wide range of phenomena with high pre-
 1546 cision, including new physics events. Even though it is a general-purpose
 1547 experiment, it was designed taking into account the Higgs searches that
 1548 were carried out at LHC. This is why, since the mass of the Higgs was not
 1549 known at that time, its performance requirements cover a large mass range
 1550 for the Higgs decay products.

1551 The stone for the foundations of ATLAS was laid in March 1992 at
 1552 the critical ‘Towards the LHC Experimental Programme’ meeting, where

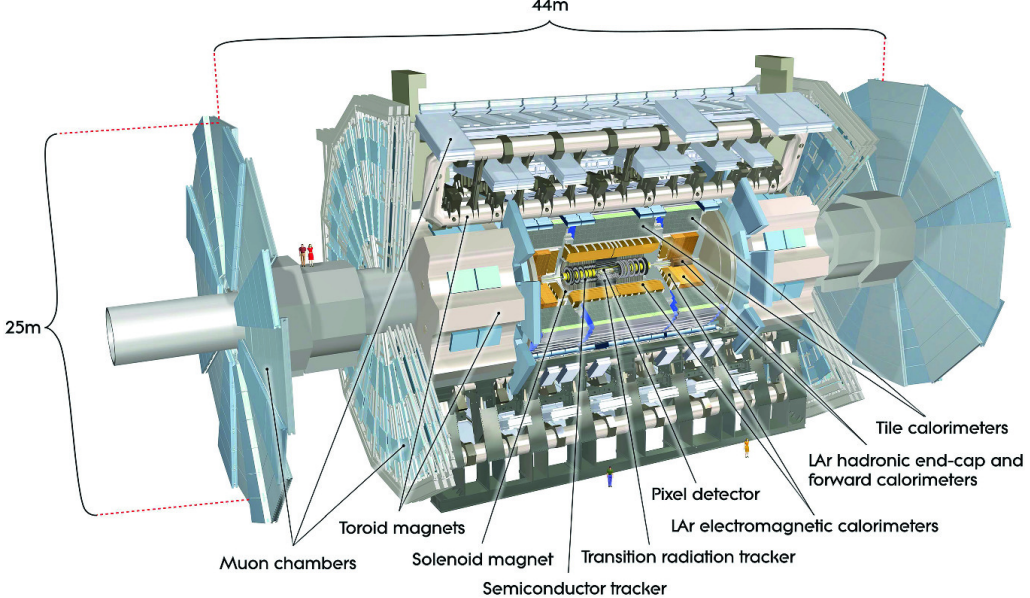


Figure 2.13: Simulated schematic view of the ATLAS detector.

1553 physicists proposed several possible experiments for the LHC [142]. Two
 1554 projects based on large toroidal magnet systems were proposed EAGLE and
 1555 ASCOT. By the summer of that year, both experiments merged into ATLAS.
 1556 In October 1992, the letter of intent of the ATLAS Collaboration was sent to
 1557 the LHC Experiments committee and, in 1994, the technical proposal [143].
 1558 In 1997 the formal approval of the ATLAS experiment arrived and one
 1559 year later the excavation on the cavern began. The cavern was inaugurated
 1560 five years later and the construction of the ATLAS detector ended in 2008.
 1561 Later, in 2009, at $\sqrt{s} = 2.36$ TeV, ATLAS records its first collisions [144].

1562 One of the most important milestones for ATLAS (and for all science
 1563 in the last decades) was the observation of a particle consistent with the
 1564 Higgs boson in July 2012 (see 1.3.2). In 2016, the combination of ATLAS
 1565 and CMS measurements for Higgs boson production on decay rates with
 1566 Run-1 data was published [145]. After that, the physics programme at 13
 1567 TeV allowed precision studies of the Higgs boson and other SM particles, as
 1568 well as the search for new particles with higher masses.

1569 Other relevant items in ATLAS timeline are the observation and rate
 1570 measurement of $t\bar{t}$ events [146] or the evidence for rare electroweak $W^\pm W^\pm$
 1571 production [147]. The first evidence of light-by-light scattering at high
 1572 energy was also found with ATLAS [148]. The first $t\bar{t}H$ associate production
 1573 [149] and $H \rightarrow b\bar{b}$ decays [150] were observed for first time by ATLAS too.

1574 The physics programme of ATLAS include precise measurements of the
 1575 SM [151], super-symmetry studies [152], sources of \mathcal{CP} -violation [153], large

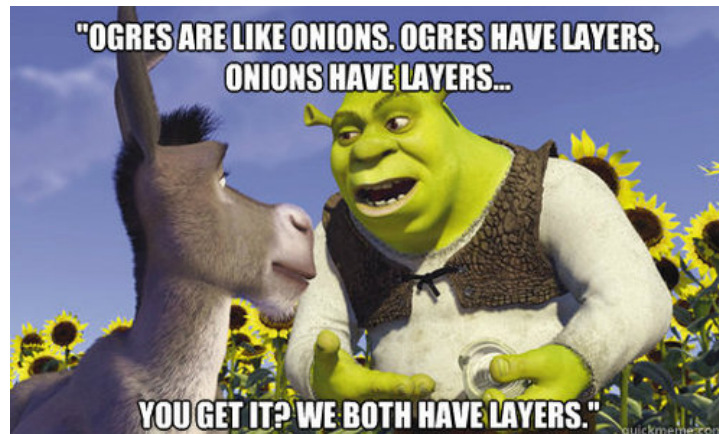


Figure 2.14: Due to its coaxial-layered structure ATLAS can be understood as cylindric onion: “*ATLAS have layers, onions have layers*” [141].

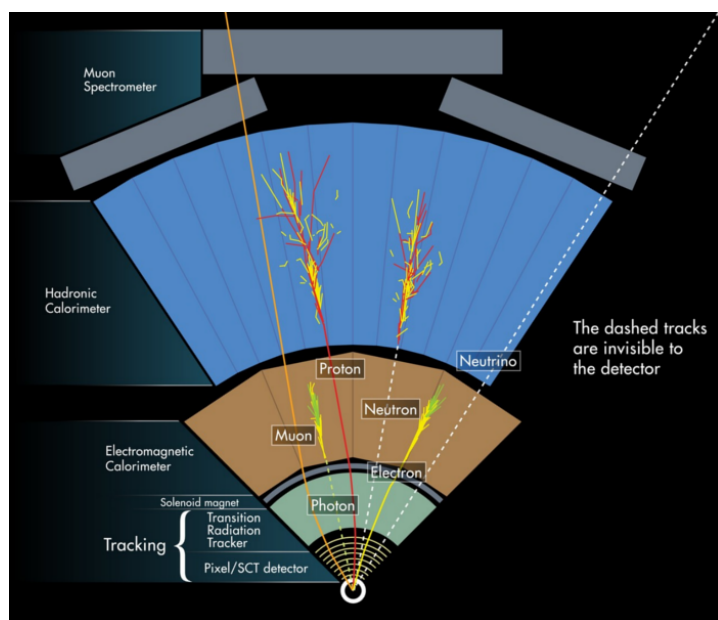


Figure 2.15: Fraction of the transversal plane of ATLAS. Each particle leaves a different signature in each layer.

1576 E_T^{miss} dark matter searches [154], astroparticle physics [155], extra dimen-
 1577 sions [156] and others.

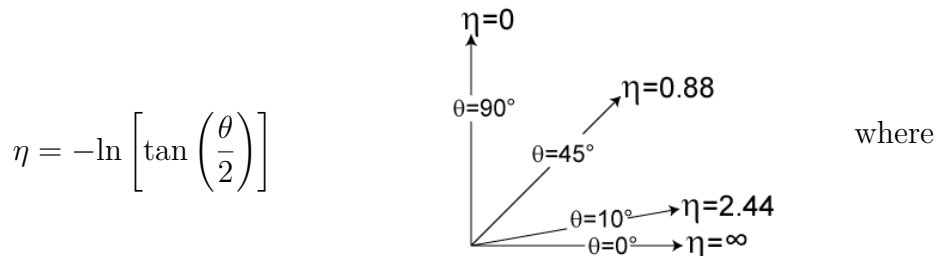
1578 ATLAS is not only a detector but also a collaboration of people com-
 1579 posed of more than 5000 members including physicists, engineers, techni-
 1580 cians, doctoral students and support staff. Working at CERN or at any
 1581 of the 181 institutions that constitute ATLAS, the different teams work
 1582 collaboratively to achieve success. Any output by any of the teams com-
 1583 prising ATLAS is shared with the rest of the collaboration and subjected
 1584 to a strict review process before making the results public, ensuring high-
 1585 quality standards.

1586 2.3.1 Objective and physics programme

1587 **Esto queda comentado en la introducción a ATLAS pero mover**
 1588 **a esta sección y extenderlo-reestructurarlo**

1589 2.3.2 Coordinate system

1590 Due to its cylindrical structure, ATLAS uses a right-handed system with
 1591 its origin at the IP where the collisions take place. On one side, there are the
 1592 (x , y , z) Cartesian coordinates. The x -axis is pointing towards the centre
 1593 of the ring circumference, the y -axis is perpendicular to the plane defined
 1594 by the LHC ring and it points to the surface, and the z -axis is defined by
 1595 the direction of the beam. On the other side, it is more frequent to employ
 1596 the cylindrical coordinates (r, ϕ, z) or the system defined by the azimuthal
 1597 angle ϕ and the pseudorapidity η :



θ is the polar angle⁴. As the polar angle approaches zero, pseudorapidity tends towards infinity. The change in pseudorapidity $\Delta\eta$ is Lorentz invariant under boosts along the beam axis. The use of η is preferred over θ because the distribution of events typically looks flat with respect to η . In therms

⁴Defined as the angle between the particle three-momentum, \vec{p} and the positive direction of the beam axis.

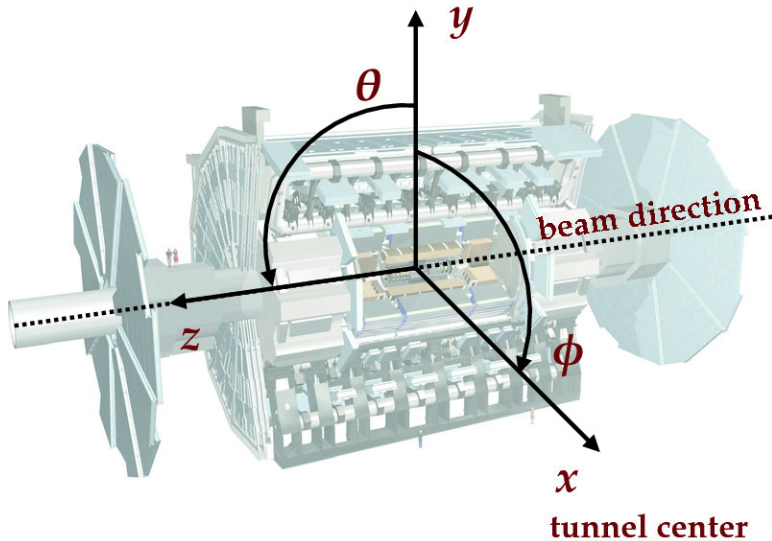


Figure 2.16: Coordinate system of the ATLAS detector.

of the momentum, the above equation can be expressed as:

$$\eta = -\ln \left(\frac{|\vec{p}| + p_z}{|\vec{p}| - p_z} \right)$$

being p_z the momentum along the beam direction. The rapidity is used when dealing with massive particles and it can be expressed as $y = \frac{1}{2} \log[(E + p_z)(E - p_z)]$, being E the energy projection of the momentum in the z -axis. Note that when the particles approach the speed of light, they are in the limit $E \approx |\vec{p}|$ and the values for rapidity and pseudorapidity converge. The angular distance is measured in units of $\Delta R = \sqrt{(\Delta\eta)^2 + (\Delta\phi)^2}$, which is invariant under a boost along the z -axis⁵. Figure 2.16 shows the coordinate system of ATLAS.

The transverse magnitudes such as the transverse momentum (p_T) and transverse energy (E_T) are defined in the x - y plane. Knowing the momentum p_T , and the pseudorapidity η and azimuthal ϕ angles, the cartesian momentum (p_x, p_y, p_z) can be derived from:

$$\begin{aligned} p_x &= p_T \cos(\phi) & p_y &= p_T \sin(\phi) \\ p_z &= p_T \sinh(\eta) & |\vec{p}| &= p_T \cosh(\eta) \end{aligned}$$

⁵ $\Delta\eta = \eta_2 - \eta_1$ and $\Delta\phi = \phi_2 - \phi_1$.

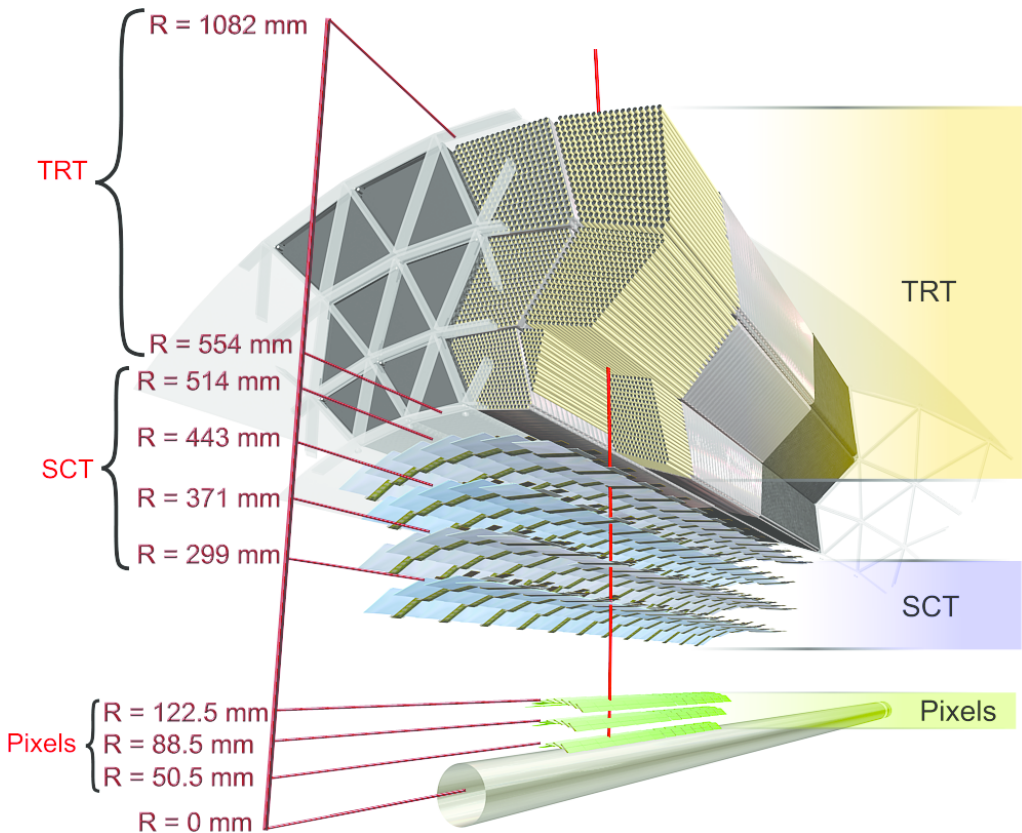


Figure 2.17: Barrel part of ID of the ATLAS experiment with the Pixel, SCT and TRT sub-detectors. The IBL is not shown here.

1606 2.3.3 Inner Detector

1607 The ATLAS ID [157][158][117] is the closest sub-detector to the beam
 1608 pipe. Its layout is shown in Figures 2.17 and ???. The charged particles
 1609 follow a curved trajectory inside the ID due to the magnetic field of the
 1610 ATLAS bending magnet. The different pieces that comprise the ID can
 1611 reconstruct the traces of these particles with great accuracy allowing, thus,
 1612 to measure its momentum (this is done using the Saggitta method [ref to](#)
 1613 [sec 3](#)). For particles coming from the IP, the geometric acceptance of the
 1614 ID is $|\eta| < 2.5$ for pseudorapidity and full ϕ coverage in the azimuthal
 1615 angle. The ID provides p_T resolution of $\sigma_{p_T}/p_T = 0.05\% \text{ GeV} \oplus 1\%$ and a
 1616 transverse impact parameter resolution⁶ of $10 \mu\text{m}$ for particles in the central
 1617 η region. It is designed to provide excellent momentum resolution, pattern
 1618 recognition and measurements of both primary and secondary vertex for
 1619 charged particles above the p_T threshold (nominally 0.5 GeV).

⁶The impact parameter determine the distance of a reconstructed track from a charged particle to the perigee (the closest point of the track to the global z -axis)

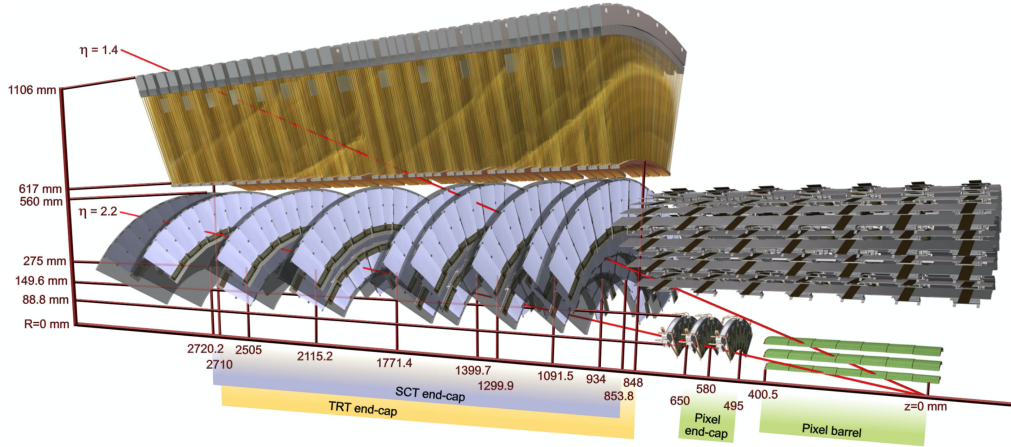


Figure 2.18: End-cap of the ID.

1620 The ID is composed of four complementary sub-detectors: The Insertable
 1621 B-Layer (IBL), the Pixel Detector, the Semiconductor Tracker (SCT)
 1622 and the Transition Radiation Tracker (TRT). In the sections that follow, a
 1623 description of each sub-system is provided.

1624 Depending on the $\eta = 1.4$ that a particle has, it will interact with some
 1625 elements of the detector. Figure ?? shows the end-cap elements transversed
 1626 by two charged particles with $\eta = 2.2$ and 1.4 . The track with $\eta = 1.4$
 1627 traverses first the beryllium beam-pipe, then the three cylindrical silicon
 1628 pixels and the four disks with double layers of the SCT. Finally, this particle
 1629 travels across approximately 40 tubes in the TRT wheels. In contrast, the
 1630 particle with $\eta = 2.2$ encounter the first of the cylindrical silicon-pixel layers
 1631 after leaving the beryllium pipe. Then, the two end-cap pixel disks and the
 1632 four last disks of the end-cap SCT.

1633 2.3.3.1 Insertable B-Layer

1634 The IBL [159] is the innermost component of the ID. It is located
 1635 between the beam pipe and the pixel detector. Added after Run-1, it
 1636 provides the closest-to-IP measurements that improve the robustness and
 1637 performance of the ATLAS tracking system. It plays a fundamental role
 1638 for b -tagging efficiency because this tagging relies on precise vertex recon-
 1639 struction. The IBL provides redundancy in the measurements of tracks in
 1640 order to control the fake rate arising from random combinations of clusters
 1641 in events with a high pile-up background.

1642 With a hit resolution of $8 \mu\text{m}$ in $r - \phi$ and $40 \mu\text{m}$ along z , the IBL covers
 1643 the $|\eta| < 2.7$ and the entire ϕ range.

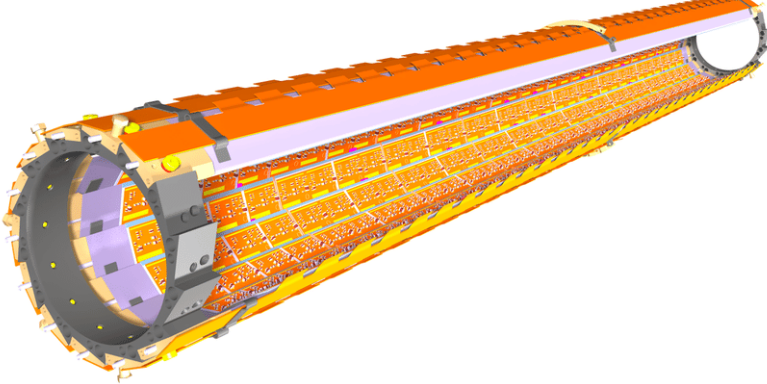


Figure 2.19: Schematic drawing of the ATLAS IBL Detector [159].

1644 The barrel structure if the IBL has a radius of 3.2 cm and is composed
 1645 by 14 carbon fibre staves as it is shown in Figure 2.19. Each stave has
 1646 incorporated cooling CO₂ circuits and has 32 or 16 modules and uses two
 1647 types of photodetectors: ATLAS pixel planar sensors and 3D pixel sensors.
 1648 The used pixels have a size of $50 \times 400 \mu\text{m}^2$. Due to the high luminosity of
 1649 the LHC, the IBL is built with radiation-tolerant sensors.

1650 2.3.3.2 Pixel Detector

1651 The ATLAS Pixel Detector [160] consists of a strip detector in the out-
 1652 ermost layers and a pixel detector in the region which is closer to the IBL.
 1653 Along with the IBL, it aims to reconstruct the trajectories of the particles
 1654 traversing it. It provides a full coverage of the azimuthal angle ϕ and a
 1655 pseudorapidity range of $|\eta| < 2.5$ as well as a resolution of $10 \mu\text{m}$ in $r - \phi$
 1656 and $115 \mu\text{m}$ in the z .

1657 The Pixel Detector and the IBL combined contain 92×10^6 pixels with
 1658 its respective electronic channels, which cover an area of approximately 1.9
 1659 m^2 of silicon consuming 15 kW . The barrel region consists of four concentric
 1660 layers equipped with 1736 sensor modules and each of the two end-caps has
 1661 three disks with 2888 modules [161].

1662 Hits in a pixel are read out if the signal exceeds a tunable threshold. The
 1663 pulse height is measured using the Time-over-Threshold (ToT) technique.

1664 2.3.3.3 Semiconductor Tracker

1665 The SCT consists of 4088 modules tiling four coaxial cylindrical layers
 1666 in the barrel region and two end-caps each containing nine disk layers, all

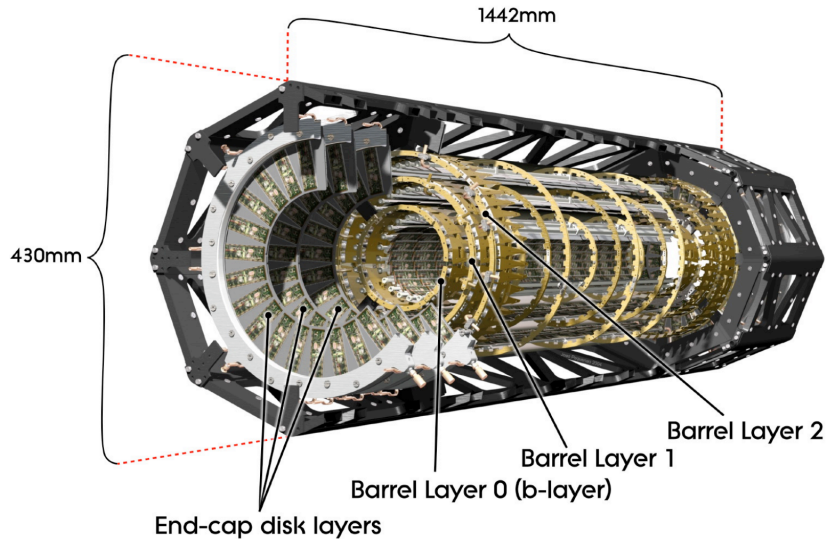


Figure 2.20: Schematic view of the ATLAS pixel detector consisting of individual barrel and end-cap layers [117].

of this surrounding the Pixel Detector and providing additional precision tracking. The main difference with the Pixel Detector is that the SCT uses microstrip sensor technology, which is very similar to that of a pixel but being much larger (6 cm). The reason to use microstrips instead of pixels is that the strips are more cost-effective than traditional pixels and a good spatial resolution can be obtained as well if the strips are arranged with an angular offset. Therefore, each SCT detector unit consists on two back-to-back silicon-microstrip planes with a relative angle of 40 mrad. Eight strip layers (i.e. four space points) are crossed by each track in the SCT providing valuable tracking information with resolution of $17\mu\text{m}$ in $r - \phi$ and $580\mu\text{m}$ in the z coordinate. The SCT covers the entire ϕ range and up to 2.5 in η .

Figure 2.21 shows an exploded view of the different components of an SCT module, including the high thermal conductivity spine, the polyimide hybrids and readout chips.

2.3.3.4 Transition Radiation Tracker

The TRT is used in conjunction with the Pixel Detector and silicon micro strip (SCT) to extend the η range in which the tracks can be reconstructed to $|\eta| = 2$. This part of the ID is formed by a large number of 4mm straw tubes filled with gas. This part of the ID relies both on the collection of primary ionisation charge and the collection of secondary ionisation charge arising from the transition radiation to measure the the track of charged particles. The tube surface functions as a cathode while the wire in the

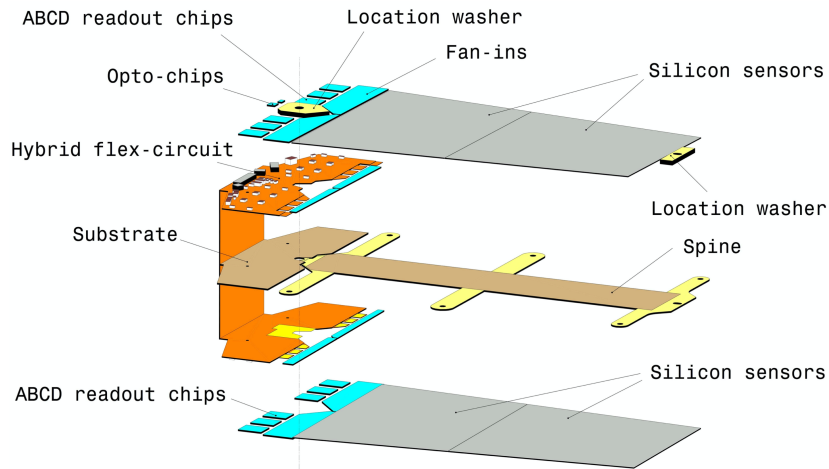


Figure 2.21: Schematic view of an SCT detector module [117].

center as a cathode. When a charged particle passes through the gas in the tube, it ionises the gas and the freed electrons drift towards the anode, generating an electrical current. This detector provides a single hit resolution of $170\ \mu\text{m}$ in $r - \phi$ but does not have sensitivity in z . The TRT also provides discrimination between electrons and pions since the latter generate a much smaller signal than the former. When the electrons pass, they produce x-ray photons that lead to strong avalanches within the tubes and, thus, a great signal.

1697 2.3.4 Calorimeters

1698 After the ID, the next layer of detectors in ATLAS correspond to the
 1699 calorimeters (Figure 2.22) [162]. Their purpose is to measure the energy
 1700 of the particles (neutral or charged), as well as to help to reconstruct the
 1701 path followed by them. Most particles initiate a shower (Section 2.3.4.1)
 1702 when they enter into the calorimeter. Part of the energy of these particles is
 1703 deposited in the device, then collected and measured by it. Most of calorimeters
 1704 in particle physics are segmented transversely to provide information
 1705 about the direction of the particles. Based on how the particle shower develops,
 1706 the longitudinal segmentation can provide information for identifying
 1707 the particle (a more detailed discussion of how particles are reconstructed
 1708 within the ATLAS detector is presented in Section 3.3).

1709 In general, calorimeters can be classified as sampling, when are made of
 1710 two types of materials, or homogeneous, built with just one type of material.
 1711 ATLAS uses sampling calorimeters, which consist of alternating layers of
 1712 different materials:

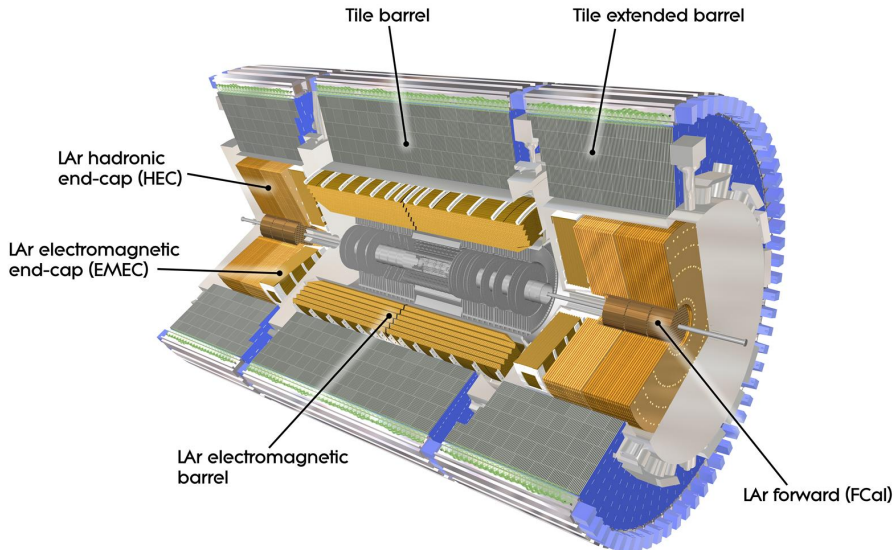


Figure 2.22: Computer generated image of the ATLAS calorimeter [161].

- **Passive material:** Also known as absorber, it is a denser material to full stop the traversing particles. When a particle interacts with the passive material it produces the shower (Figures 2.23 and 2.24). For the absorber layers in ATLAS, lead is used for the ECAL and steel for the HCAL.
- **Active material:** This material detects the particles from the shower originated in the absorber. The liquid Argon (LAr) is used as active material for ECAL and plastic scintillator for HCAL.

In the homogeneous calorimeters, the material used combines the features of an absorber and a detector, performing both tasks.

Since each type of particle interacts differently, there are two main types of calorimeters: the electromagnetic calorimeter (ECAL), which measures the energy of electrons/positrons and photons, and the hadronic calorimeters (HCAL), which registers the energy of the strongly-interacting particles. Both classes are covered in the next sections.

2.3.4.1 Particle showering

A particle shower is a cascade of secondary particles produced when a high-energy particle interacts with matter. The first particle interacts producing a secondary particle with less energy than the first one. The

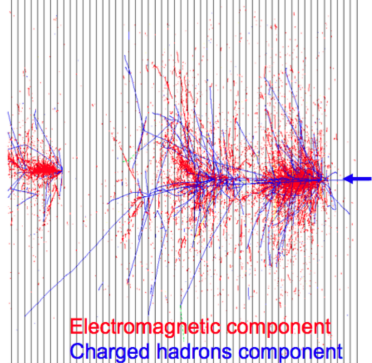


Figure 2.23: EM and hadronic cascades.

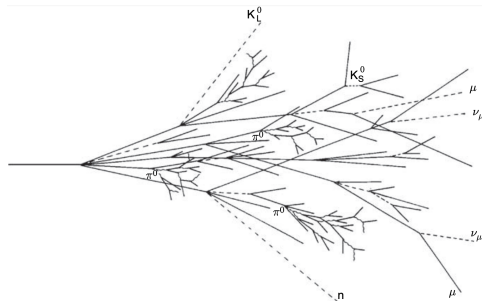


Figure 2.24: Sketch of a hadronic cascade [163].

1732 second particle does the same and, in each step, the particles produced are
 1733 less and less energetic. For a single incoming particle, this iterative process
 1734 can continue for thousands of periods [163]. An illustration of the EM and
 1735 hadronic particle cascades is shown in Figure 2.23.

1736 **Electromagnetic shower**

1737 The electromagnetic (EM) shower is initiated by a e^- , e^+ or γ , these
 1738 three particles are the sole components of this type of shower. At energies
 1739 higher than 100 MeV, the EM showering is based on two main processes:
 1740 Bremsstrahlung and pair creation. The electrons lose their energy almost
 1741 exclusively by bremsstrahlung radiation, a process in which the lepton radiates
 1742 thousands of soft photons because of its interaction with another
 1743 charged particle. The photons lose their energy by the production of an
 1744 $e^- - e^+$ pair. At lower energy scales, other processes contribute. In the MeV
 1745 range, the Compton scattering⁷ and photoelectric effect⁸ are the dominant
 1746 interactions for energy loss for photons, while the ionisation and excitation
 1747 are for the charged particles (e^- and e^+).

1748 **Hadronic shower**

1749 When a hadron interacts with the passive material, this shower is initialised.
 1750 Both strong and EM interactions are involved in the development of this
 1751 type of shower and they present a larger variety of particle components.
 1752 Therefore, the hadronic showers are significantly more complex than the
 1753 EM. Figure 2.24 shows the processes leading to a hadronic cascade.

⁷Scattering of a photon after interacting with a charged particle, usually an electron.

⁸Emission of photoelectrons when the EM radiation interacts with matter.

1754 The production of neutral pions represents about a third of the energy
 1755 loss of hadronic interactions. These pions decay 98.8% of times to two
 1756 photons [164] that are starting the EM showers. The rest of hadronic inter-
 1757 actions consist of the production of charged mesons, nuclear fragments and
 1758 protons, soft neutrons and photons or unpredictable loss through undetect-
 1759 able processes.

1760 2.3.4.2 Electric calorimeter

1761 The ECAL [162] absorbs the energy of the e^- , e^+ or a γ covering a
 1762 pseudorapidity range of $|\eta| < 1.475$ in the barrel. It is made of a lead
 1763 absorber and LAr detector following an accordion shape, as can be seen
 1764 in Figure 2.25a, where the different layers are clearly visible. The shower
 1765 originated at the absorber layer ionise the LAr producing a measurable
 1766 current proportional to the energy of the original particle. The LAr layer
 1767 operates at 87 K.

1768 The barrel part is split into two identical half-barrels separated by a
 1769 small gap at $z = 0$. Each end-cap calorimeter is composed of two coaxial
 1770 wheels that cover $|\eta| < 1.475$.

1771 The total amount of material in the ECAL corresponds to 25-35 radi-
 1772 ation lengths, X_0 , and 2-4 nuclear interaction lengths, λ , over the entire η
 1773 range. Characteristic of each material, the ration length is the mean dis-
 1774 tance over which a high-energy electron lose all but $1/e$ of its energy by
 1775 bremsstrahlung. The radiation length is the mean free path between inter-
 1776 actions required to reduce the number of relativistic charged particles by
 1777 the factor $1/e = 0.37$ as they pass through matter.

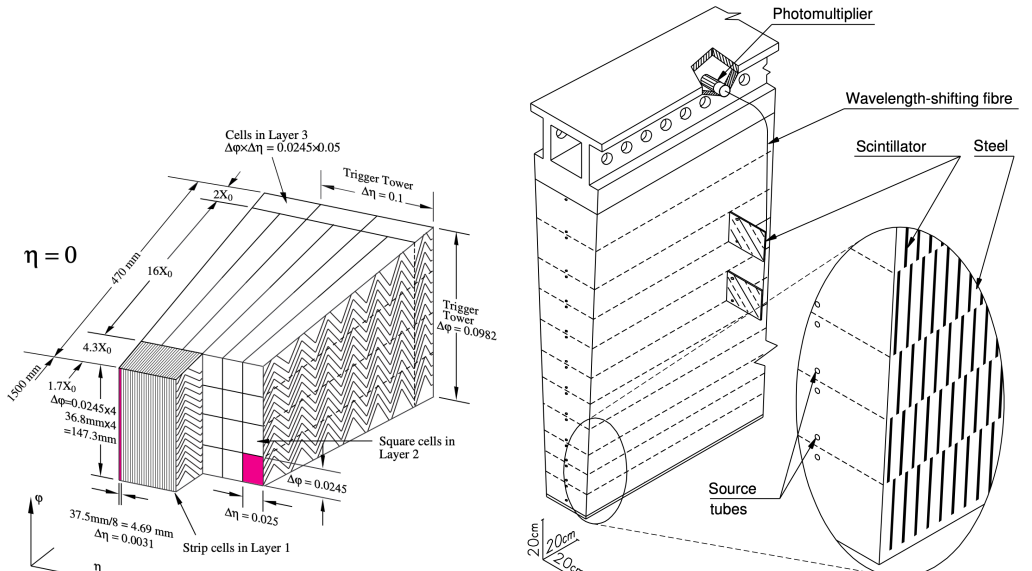
The energy resolution of a calorimeter can be parametrised as:

$$\frac{\sigma_E}{E} = \frac{a}{\sqrt{E}} \oplus \frac{b}{E} \oplus c = \frac{10\%}{\sqrt{E}} \oplus \frac{170 \text{ MeV}}{E} \oplus 0.7\%$$

1778 Where a is the stochastic term, b the electronic noise and c a constant that
 1779 includes detector instabilities and increases with E [165].

1780 2.3.4.3 Hadronic calorimeter

1781 The ATLAS HCAL [162] is made of a sampling calorimeter of steel and
 1782 plastic scintillator tiles covering the pseudorapidity region of $|\eta| < 1.7$ in
 1783 the barrels. The end-caps are made of copper and LAr, covering $1.5 < |\eta| <$
 1784 3.2, and are emended in the end-caps of the ECAL. This calorimeter uses
 1785 9800 electronic channels in the barrel and 5600 in the end-cap. With 2900



(a) Sketch of section of the LAr EM barrel were the different layers are visible [117]. (b) Mechanical assembly and optical readout of the tile calorimeter of the HCAL.

Figure 2.25: Sketch of a section of the ATLAS (a) ECAL and (b) HCAL [117].

1786 tones, the HCAL is the heaviest part of the ATLAS detector. It has 420000
1787 scintillator tiles and 9500 photomultiplier tubes. The plastic scintillators
1788 turn the particles that the shower originated in the steel layer into photons,
1789 which are converted into an electric current whose intensity is proportional
1790 to the original particle's intensity [161]. All these elements are shown in
1791 Figure 2.25b, where the tiles, the fibres and the photomultipliers are visible.

The contribution of the electronic noise is negligible, therefore, the energy resolution for the tile calorimeter is [162]:

$$\frac{\sigma_E}{E} = \frac{5.9\%}{\sqrt{e}} \oplus 5.7\%$$

1792 2.3.4.4 Forward calorimeter

In addition to the ECAL and HCAL, a smaller calorimeter is placed in the end-caps surrounding the beam pipe in order to cover the forward region ($3.1 < |\eta| < 4.9$), the forward calorimeter (FCAL). This calorimeter is a sampling calorimeter based on LAr as active medium and copper as absorber. The thickness of the FCAL is optimised to achieve high absorption, approximately, $10 X_0$ [165].

$$\frac{\sigma_E}{E} = \frac{100\%}{\sqrt{e}} \oplus 10\%$$

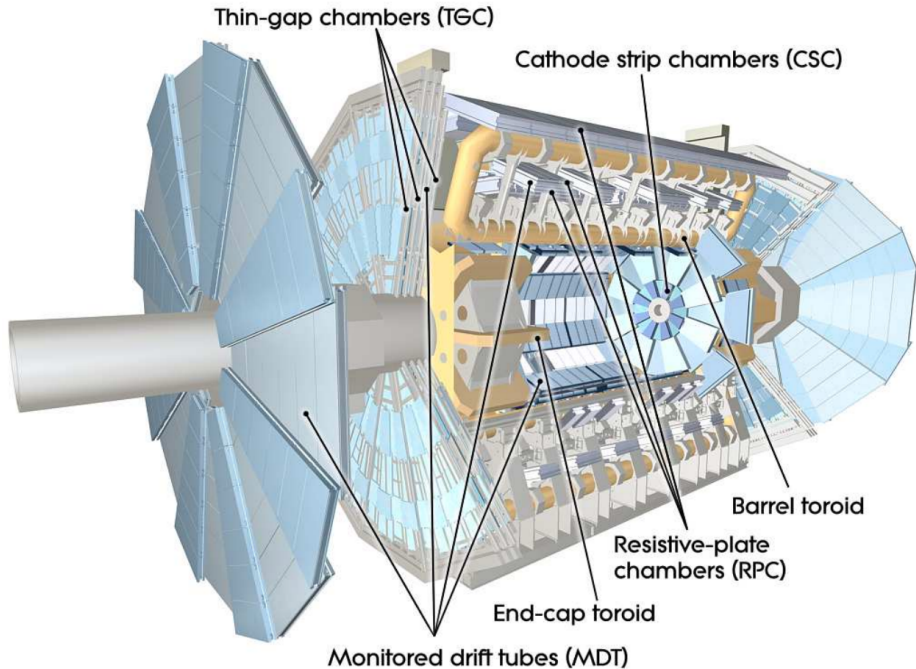


Figure 2.26: Conceptual layout of the MS (blue). The magnet system (yellow) is also shown [117].

1793 2.3.5 Muon Spectrometer

1794 The muons can penetrate through calorimeters and reach the last layer
 1795 of the ATLAS detector, the MS [166].

1796 Figure 2.26 shows a cut-away view of the ATLAS muon system.

1797 The MS surrounds the calorimeters and measures the trajectories of
 1798 muons to determine their direction and momentum with excellent tracking
 1799 precision as well as their electric charge in a pseudorapidity coverage of
 1800 $|\eta| < 2.7$. To bend the particle tracks after they exit the HCAL, the MS
 1801 uses eight large superconducting air-core toroid magnets in $|\eta| < 1.4$ region.
 1802 For the $1.6 < |\eta| < 2.7$, the tracks are bent by magnets inserted in the
 1803 end-caps. In the transition region, $1.4 < |\eta| < 1.6$, the magnetic field
 1804 responsible of bending the particles is provided by both the air-core toroid
 1805 magnets and the smaller end-cap magnets. These fields are perpendicular
 1806 to the trajectory of the muons originated in the IP.

1807 The MS instrumentation is based, on one hand, on precision chambers
 1808 for the coordinate measurements in the bending plane: Monitored Drift
 1809 Tube chambers (MDT) and Cathode-Strip Chambers (CSC), and, on the
 1810 other hand, on trigger chambers: Resistive Plate Chambers (RPC) and

Type	Purpose	Location	Coverage
MDT	Tracking	Barrel + end-cap	$0.0 < \eta < 2.7$
CSC	Tracking	End-cap layer 1	$2.0 < \eta < 2.7$
RPC	Trigger	Barrel	$0.0 < \eta < 1.0$
TGC	Trigger	End-cap	$1.0 < \eta < 2.4$

Table 2.3: ATLAS MS sub-detectors [167].

1811 Thin Gap Chambers (TGC). Table 2.3 gives a summary of the MS detector
 1812 components. In 2.28 the distribution of the MS detectors is described.

- 1813 • **Monitored Drift Tube chambers (MDTs)** [168]: The MDT chambers
 1814 provide precise momentum measurements by determining with
 1815 high accuracy the curve of the tracks. This part of the MS cover a
 1816 pseudorapidity range of $|\eta| < 2$. The MDTs are designed to have
 1817 stand-alone measurement capability in order to safeguard against any
 1818 unanticipated background and to ensure good discovery potential in
 1819 the scenario of unexpected topologies. In the barrel region, the MDTs
 1820 are arranged in three cylindrical stations coaxial to the beam axis and
 1821 in the end-cal, the MDTs are vertically installed in three layers. An
 1822 MTD chamber consists of six layers of drift tubes (as depicted in Figure
 1823 2.27), each of them with 3 cm of diameter, filled with gas. A tube
 1824 can achieve a single wire resolution of $80 \mu\text{m}$ [167]. In the entire MDT
 1825 system, there are 1 171 chambers with a total of 354 240 tubes.
- 1826 • **Cathode-Strip Chambers (CSC)**: It is the innermost tracking
 1827 layer of the MS. Due to its higher rate capability and time resolution,
 1828 it is located close to the beam axis, where the particle fluxes
 1829 are higher. This component of the muon detector system covers the
 1830 η range $2.0 < |\eta| < 2.7$. It measures with precision the coordinates at
 1831 the ends of the detector. With its 70 000 electric channel, provides a
 1832 resolution around $60 \mu\text{m}$.
- 1833 • **Resistive Plate Chambers (RPC)** [169]: This is the barrel element
 1834 of the trigger system. These chambers are located on both sides of
 1835 the central CSC and inside the outermost CSC station. The RPCs
 1836 are gaseous detectors used for triggering and for measuring the second
 1837 coordinate in the barrel region. RCPs provide a time-space resolution
 1838 of $1 \text{ cm} \times 1 \text{ ns}$. The gas gap is of the order of 2 mm and the plate
 1839 external surfaces are coated by thin layers of graphite painting. This
 1840 part of the MS is composed of 3 800 electric channels.

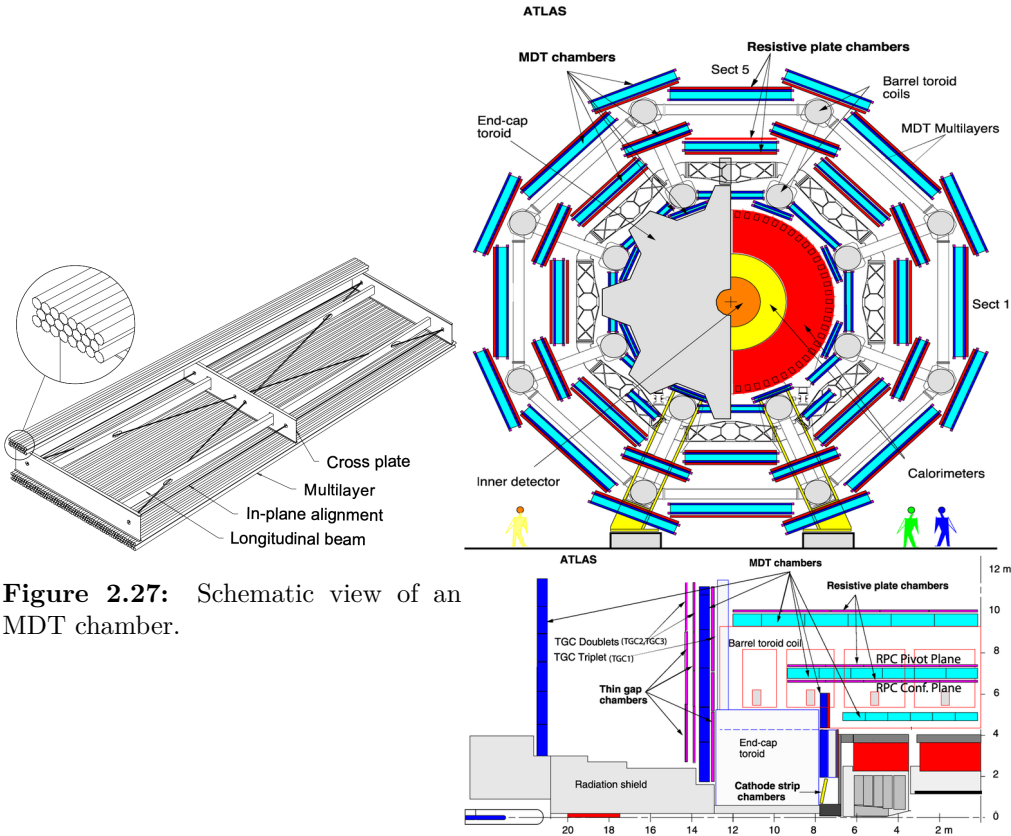


Figure 2.27: Schematic view of an MDT chamber.

Figure 2.28: ATLAS muon detectors.

- **Thin Gap Chambers (TGC)** [170]: As a first-level trigger, they have to provide high efficiency and excellent time resolution for bunch-crossing tagging in a high-background environment. The particle flux received by the TCG is higher than that of the RPC. The three TGCs are located near the middle end-cap MDT station, in the forward regions. TGCs measure the second coordinate in the non-bending direction with its circa 440 000 electrical channels.

2.3.6 Magnet system

The curvature in the track of the particles is fundamental to measure the transverse momentum and the charge of the particles. To bend the path of charged particles, these are immersed in a homogeneous magnetic field which is produced by the both the toroidal and solenoid magnets. The bending power is proportional to $\int B dl$, where B is the magnetic field component orthogonal to the charged direction.

ATLAS magnetic system is divided into three subsystems: the central solenoid magnet, the barrel toroids (BT) and the end-cap toroid (ECT).

2.3.6.1 Central solenoid magnet

The ATLAS solenoid surrounds the ID providing a 2 T magnetic field at the centre of the tracking volume. This magnet is very thin, having only 4.5 cm thickness, which minimises the interaction of the particles with the magnet material. It is important to not use a lot of material here because, otherwise, the interaction of the particles with the solenoid magnet would impact negatively in the performance of the calorimeters. To achieve such a field within a small thickness, 9 km of niobium-titanium superconductor wires are strengthened, pure aluminium strips and cooled down to 4.5 K are used. The central solenoid magnet has a cylindrical shape with a diameter of 5.6 m and a length of 2.56 m, and it weights 5 tonnes.

2.3.6.2 Toroid magnets

Three large air-core toroids (one barrel and two end-caps) generate the magnetic field in the MS. The magnetic field provided by the toroid magnets is 3.5 T. Each toroid consists of eight coils assembled with cylindrical symmetry (see Figure 2.26). The coils are based on an aluminium stabilised Niobium-Titanium alloy (Al/NbTi/Cu) superconductor operating at 4.5 K. The main difference between the barrel and end-cap toroids for the cold mass is that the latter has a higher critical current and less aluminium than the former [171].

Barrel Toroid

The Barrel Toroid magnet is the largest component of the ATLAS magnet system. It generates a toroidal magnetic field which, as introduced in Section 2.3.5, is almost completely perpendicular to the track of the particles. In order to minimise the impact (i. e. reduce any interaction apart from applying magnetic field) of the magnet system with the particles, the barrel toroid is designed as an open and light structure. The barrel toroid coils are housed in eight individual cryostats, with the linking elements between them providing the overall mechanical stability. A view of the coils of the barrel toroid in their cryostats is in Figure 2.29.

The magnetic flux density delivered by this magnet is 4 T on the superconductor. For the toroid barrel, the bending power ($\int B dl$) is in the interval 1.5 Tm to 5.5 Tm in $0 < |\eta| < 1.4$. It is the largest toroidal magnet

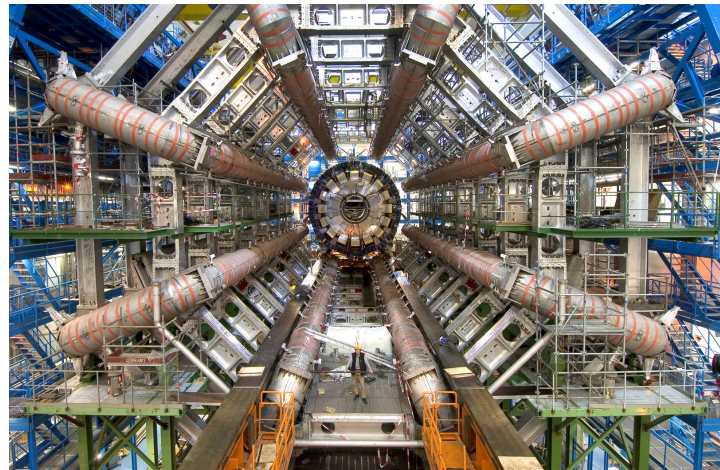


Figure 2.29: Very cool picture of the installation ATLAS calorimeters. The eight coils that compose the ATLAS barrel toroid magnets are already installed in the cryostats.

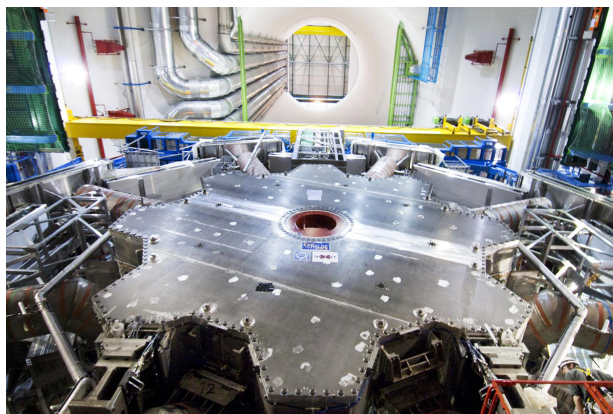


Figure 2.30: End-cap toroidal magnet.

1890 ever built (25.3 m in length), being probably the most iconic element of AT-
 1891 LAS. It weights 830 tonnes and uses more than 56 km of superconducting
 1892 wire [161].

1893 **End-cap Toroid**

1894 The end-caps extend the magnetic field of the barrel toroid to the beam pipe.
 1895 These magnets are constrained by the inner radius of the barrel toroid and
 1896 the axial length of the experiment.

1897 As well as in the barrel toroid, it has a 4 T magnetic field on the super-
 1898 conductor. For the end-cap toroid, the $\int B dl \in [4, 8]$ in the pseudorapidity
 1899 range $1.6 < |\eta| < 2.7$ [171]. In the transition region where the end-cap and
 1900 barrel toroids overlap ($1.4 < |\eta| < 1.6$) the bending power is lower. Each
 1901 end-cap (Figure 2.30) has a diameter 10.7 m and weights 240 tonnes [161].

1902 **2.3.7 Trigger and Data Acquisition System**

1903 The proton bunches cross at the center of the ATLAS detector 40 million
1904 times per second, resulting in approximately (using Run-2 $\langle \mu \rangle = 33.7$)
1905 1 200 million proton collisions per second. Reading out and storing all the
1906 information from this interactions is not feasible since it has a combined
1907 data volume of more than 60 million megabytes per second. Only some of
1908 these events are of interest to physics studies and, consequently, need to
1909 be saved into permanent storage for later analysis. In order to select only
1910 interesting data, ATLAS uses a complex and highly distributed Trigger and
1911 Data Acquisition System (TDAQ) [172] that reduces the rate of recorded
1912 data from the initial 1 200 MHz of interactions to just an average of 1 kHz.
1913 The reduction through the trigger is carried in two steps: The electronic
1914 performs an initial selection and, afterwards, a large computer farm analyses
1915 the data that pass the initial filter.

1916 The TDAQ system is an essential component of ATLAS in charge of
1917 processing the events online, selecting the relevant ones and storing them.
1918 To do so, the TDAQ verifies for each bunch crossing if at least one among the
1919 hundred conditions is satisfied. These conditions, also known as *triggers*,
1920 are based on identifying both combinations of candidate physics objects
1921 (*signatures*) and global event properties of the events [173]. Figure 2.31
1922 shows a diagram of the TDAQ system, in this figure can be seen the relevant
1923 components as well as the detector read-out and data flow.

1924 The first-level trigger (LVL1) is a hardware-based filter performed by
1925 ATLAS sub-detectors. The LVL1 uses the information of the Calorimeters
1926 and the MS to select events up to the maximum-readout rate of the detector
1927 (100 kHz) within a latency of 2.5 μ s. Additionally, the LVL1 identifies the
1928 regions of interest (RoI), which includes the position and the p_T of the
1929 candidate objects.

1930 For each event accepted by the LVL1, the Front-End (FE) detector elec-
1931 tronics read the detectors data and pass it to the ReadOut Drivers (ROD).
1932 The ROD performs the initial processing and formatting and the ReadOut
1933 Systems (ROS) buffers this data.

1934 The data from the different sub-detectors is sent from the ROS to the
1935 software-based trigger, the so called High Level Trigger (HLT), when is
1936 requested by the HLT. This system is comprised by the second-level trig-
1937 ger (LVL2) and the Event Filter (EF or third-level), both made of several
1938 farms of computers (about 40 000 CPU cores) interconnected by Ethernet
1939 networks. Using modest computing power, LVL2 provides high rejection
1940 power with fast and limited precision algorithms. With higher computing
1941 power, the EF features lower rejection power with slower but higher preci-

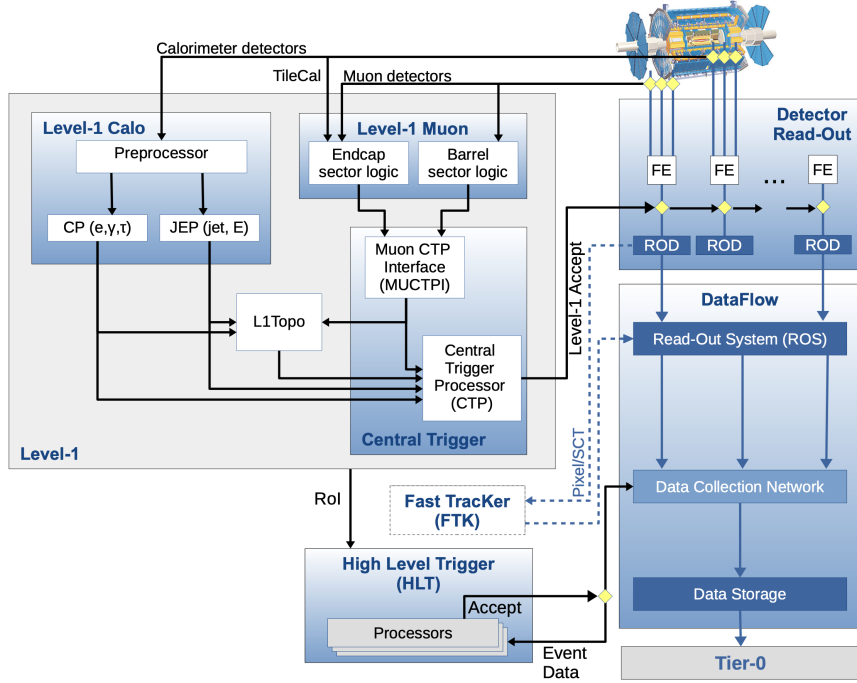


Figure 2.31: The ATLAS TDAQ system in Run-2.

1942 sion algorithms [172]. This combination is a cost-effective and flexible way
 1943 of implementing the HLT. The ID, which was not used by the LVL1, is of
 1944 key importance for the HLT because on, one hand, the LVL2 reconstruction
 1945 algorithms are specifically designed to meet strict timing requirements
 1946 and, on the other hand, the track reconstruction on the ED is less time
 1947 constrained. This is done by the ID's Fast TracKer (FTK) as the Figure
 1948 2.31 shows.

1949 An average 1.2 kHz output rare for Run-2 pass the HLT (with a latency
 1950 of just 200 μ s) and is sent by the Sub-Farm Output (SFO) to the Tier-0
 1951 facilities for permanent storage and later offline physics analysis.

1952 2.3.8 Computing resources

1953 *¿Los computing resources de ATLAS son algo a parte del LCG
 1954 descrito en la sección 2.2.4?* ATLAS Software: Athena

1955 2.3.9 ATLAS upgrade towards HL-LHC

1956 CERN has embarked on a very ambitious project, the High Luminosity
 1957 Large Hadron Collider (HL-LHC). Adding more particles to the bunches



Figure 2.32: Timeline for the LHC and LHC HL projects. The periods of data taking are named Runs and, between runs, there are the Long Shutdowns (LS) in which the different facilities are upgraded.

and focusing more the beam, would result on a grater collision rate (of about a factor 10). This provides the different analyses with better statistics, which eventually results in more precise searches and measurements. A peak instantaneous luminosity of $\mathcal{L} = 7.5 \times 10^{34} \text{ cm}^2 \text{s}^{-1}$ is expected, this corresponds to between 140 and 200 inelastic pp collisions per bunch crossing, in contrast to the current 36.1 recorded during last year of Run-2 (see Figure 2.10 to check the $<\mu>$).

In contrast to the timeline in Figure 2.32, the latest update of the schedule dates the Long Shutdown 3 (LS3) start in 2026 and the Run-4 start in 2029.

Some technologies developed to upgrade the LHC to HL-LHC are:

- Shorter bending dipole magnets are going to be installed. The current ones have a length of 15 m while the new are only 5.5 m, allowing the insertion of the collimators of Figure 2.33. The new niobium-tin dipole magnets will generate an 11 T magnetic field compared with the current 8.3 T.
- Brand new and more powerful superconducting quadrupole magnets (up to 12 T) made of niobium and tin will substitute the current ones (8 T). These magnets will be located at the sides of the ATLAS and CMS detectors

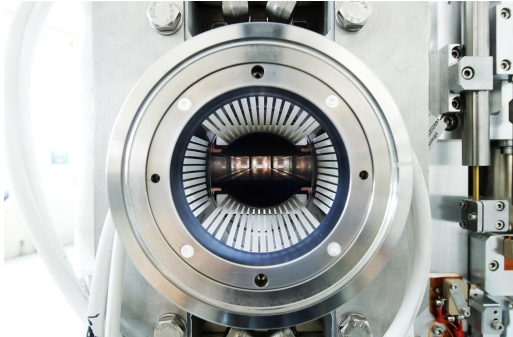


Figure 2.33: HL-LHC Collimator.

- New Beam optics. At present, as bunches cross, the protons collide and disappear and, hence, the luminosity decreases. For the Run-4, in order to keep the luminosity at the same level, the beam focusing is designed to keep the collision rate constant.
 - Superconducting crab cavities for giving the bunches additional transverse momentum in order to increase the probability of collisions.
 - New collimator sand injection magnets will also improve the performance of the machine.
 - Thanks to the new high-temperature superconductors, currents up to 10^5 Amperes will be carried over long distances.
 - New collimators that produce less electromagnetic interference with the beam are being installed. Collimators (Figure 2.33) are important because the machine protection is based on them. These elements of the accelerator absorb particles that stray from the beam trajectory and can harm the devices.
 - The accelerator chain is improved as well with the use of the linear accelerator LINAC4 and with upgrades in the PSB, PS and PSP.
- Although increasing the collision rate of the beams is a crucial goal for CERN, improving the accelerator is not enough. The current detectors have been designed for LHC and not the HL-LHC and, thus, can not handle the increased luminosity. By increasing the luminosity while keeping the same bunch spacing, a much higher rate of collisions per bunch crossing is achieved and this implies a higher pile-up. For Run-2, the pile up peaked around $\mu_{max} \approx 70$ and that was already quite taxing for the system in terms of tracking and reconstruction, and for Run-4 it may start around 140 and increase to 200.

2004 Inner Tracker The elements in the ID receive a lot of radiation damage
 2005 due the huge rate of particles hitting the detector. This radiation environ-
 2006 ment will be even more daunting in the HL project. Therefore, the design
 2007 of ATLAS (as well as all other main detectors of LHC) has to be reviewed,
 2008 especially for more central the parts of the detector.

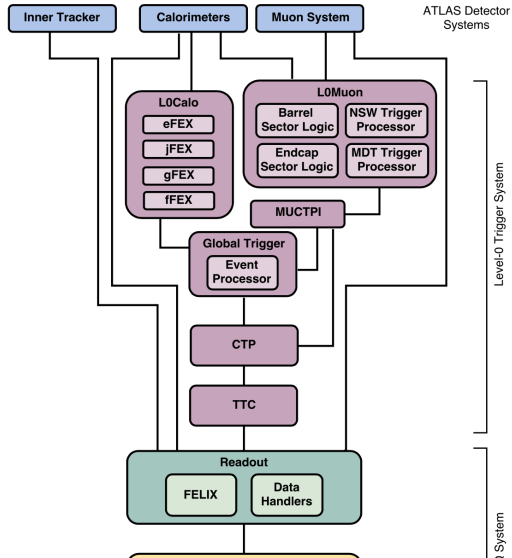
2009 To deal with this, ATLAS needs much more capable trackers, therefore,
 2010 the entire ID is going to be replaced with a new “inner tracker” (ITk).
 2011 This new detector consist on cylinder and end-caps equipped with silicon
 2012 detectors covering a geometrical acceptance of $|\eta| < 4$. This expanded
 2013 pseudorapidity range introduces many advantages in terms of object recon-
 2014 struction and pile-up mitigation by linking objects to the primary vertex
 2015 corresponding to the hard-scatter of interest. The new pixels sensors will
 2016 be placed very close to the the interaction region, where the high fluencies
 2017 ($2 \times 10^{16} n_{eq} \text{cm}^{-2}$ in the HL vs the current $10^{15} n_{eq} \text{cm}^{-2}$) have to be tolerated
 2018 while maintaining a 96% efficiency of particle detection [160].

2019 As well as the ID, the ITk is divided in two subsystems mounted in
 2020 the pixel support tube: the pixel detectors and the strip detectors that
 2021 surrounds the pixels. For the strips, there are four barrel layers and xix
 2022 end-cap petals and for the pixels, five layers are used.

2023 Calorimeters Due to radiation tolerance limits, the electronics for the
 2024 ECAL and HCAL have to be updated. The on-detector FE electronics
 2025 cannot operate with the trigger rates and latencies required for the HL-
 2026 LHC luminosities. The FCAL will remain the same as in Run-2.

2027 Muon Spectrometer The upgrades for the MS for the HL-LHC are fo-
 2028 cused on the muon trigger chambers. The Level-0 trigger electronics of the
 2029 RPC and TCG will be upgraded and for the RPC the pseudorapidity cov-
 2030 erage will be significantly increased. The front-end of the MDT is going to
 2031 be replaced as well to address the trigger rate and latency requirements.

2032 Trigger and Data Acquisition
2033 system To reconstruct the events
 2034 offline, they have to be recorded in
 2035 the first place, otherwise, it makes
 2036 no sense to have that huge pp col-
 2037 lision rate. This is why while the
 2038 detector hardware is being heavily
 2039 upgraded, a lot of effort is being put
 2040 into the trigger systems. The new



2041 trigger system is a multistage sys-
2042 tem that progressively takes more
2043 and more detailed information and
2044 each step has more time to make
2045 this decision. It starts with 40 MHz
2046 input rate (40^6 input events per
2047 second). The triggering process
2048 starts by the Level-0 (Figure 2.34
2049 in purple) and makes very quick
2050 decisions ($10\ \mu\text{s}$ latency), reducing
2051 the rate from 40 to 1 MHz. Af-
2052 terwards it passes to the event fil-
2053 ter (Figure 2.34 in orange) which
2054 takes the 1 MHz down to 10 kHz
2055 that sends to permanent storage.
2056 The key part is that these 10 kHz
2057 are really the most useful 10 kHz
2058 [174]. For doing so, the perform-
2059 ance of the tracking is fundamental
2060 for things like particle flow identifi-
2061 cation, $E_{\text{T}}^{\text{miss}}$ measurements, jet tag-
2062 ging or tau identification.

2063

2064 **From ATLAS Digest: weekly news – 11 February 2022** "Con-
2065 cerning the High Luminosity LHC, with the new schedule, LS3 will start in
2066 2026 and the Run 4 would start in 2029. A new HL-LHC running paramet-
2067 ers baseline is under discussion, which leads to new projections foreseeing
2068 715/fb of pp data collected in Run 4. The beam energy for HL-LHC has
2069 also been discussed and several scenarios to reach 7 TeV per beam have been
2070 discussed. The high risk of warm-ups is a main concern and the decision
2071 will likely be postponed to the end of Run 3. Options to stay at 6.8 TeV or
2072 even backing off to 6.5 TeV to further avoid warm-ups are still on the table.
2073 Concerning the Nb3Sn inner triplets, full scale preseries prototypes are in
2074 production."

2075 **2.3.9.1 Performance**

2076 **2.3.9.2 Challenges**

2077 **2.4 Alignment of the inner detector**

2078 **2.4.1 Alignment requirements**

2079 **2.4.1.1 Local coordinate frame**

2080 **2.4.1.2 Track parameters**

2081 **2.4.1.3 Residuals**

2082 **2.4.2 Track based alignment**

2083 **2.4.2.1 Global χ^2 algorithm**

2084 **2.4.2.2 Weak modes**

2085 **2.4.2.3 Alignment levels and degrees of freedom**

2086 **2.4.3 Alignment results during Run-2**

2087 [**Preguntar a Paolo sobre esto**](#)

2088 **2.4.4 Alignment towards Run-3**

2089 [**Preguntar a Paolo sobre esto**](#)

2090 **2.4.4.1 Pseudo-real-time-online monitoring**

2091 **Chapter 3**

2092 **Data and simulated events and
2093 object reconstruction**

2094 [175]

2095 **3.1 Data**

2096 Datasets

2097 **3.2 Monte Carlo**

2098 <https://inspirehep.net/literature/856179> In this section I
2099 should describe the generalities of the MC generators and in the
2100 Section4 the specifics for this analysis

2101 From ATLAS Digest: weekly news – 11 March 2022 (use
2102 to write some comments) Reducing negative weights in Sherpa
2103 (Frank Siegert) With the expected very large increase in size of samples
2104 in future runs, Monte Carlo samples will not be able to scale with the accu-
2105 mulated data, as needed for physics performance, without strong develop-
2106 ments in several areas of the simulation. The event generation is projected
2107 to take approximately 20% of the CPU resources and is the single largest
2108 component in CPU consumption of the simulation. It is therefore extremely
2109 important that strategies, that are not just to produce more since it is not
2110 a computationally viable solution to improve on the statistical uncertainty
2111 of the samples, be pursued. Frank discussed the importance of reducing the

2112 fraction of negative weights to improve the effective statistical uncertainty
2113 of weighted samples in Sherpa.

2114 He described a three-fold solution he has proposed in collaboration with
2115 Sherpa co-authors (available here) to reduce the fraction of negative weights.
2116 The three proposed methods correspond to approximations done for (i) the
2117 generation of events with soft emissions (S), (ii) the generation of events
2118 with hard emissions (H) and (iii) the use of a differential K-factor for leading
2119 order Matrix Elements with large numbers of emissions. Reducing negative
2120 weights necessarily leads to approximations and possible biases. Frank de-
2121 scribed in detail a comparison of the three methods. Differences are within
2122 the systematic uncertainties of the produced samples. These methods show
2123 that an improvement in equivalent statistics of a factor of approximately
2124 two can be achieved. **end of ATLAS Digest**

2125 **3.2.1 MC simulations**

2126 The generation of the simulated event samples includes the effect of
2127 multiple pp interactions per bunch crossing, as well as the effect on the
2128 detector response due to interactions from bunch crossings before or after
2129 the one containing the hard interaction.

2130 **3.2.1.1 Parton shower simulation**

2131 **3.2.1.2 Hadronisation simulation**

2132 **3.2.1.3 Underlying decay simulation**

2133 **3.2.1.4 Hadron decay simulation**

2134 **3.2.1.5 Pile-up simulation**

2135 **3.2.2 MC generators**

2136 **3.3 Object reconstruction and identification**

2137 **3.3.1 Tracking**

2138 **Highlight the importance of the alignment for the object defin-**
2139 **ition and its reconstruction. Link this section with ??**

₂₁₄₀ **3.3.2 Vertices**

₂₁₄₁ **3.3.3 Electrons and photons**

₂₁₄₂ **3.3.4 Muons**

₂₁₄₃ **3.3.5 Jets**

₂₁₄₄ **3.3.6 Bottom quark induced jets**

₂₁₄₅ **3.3.7 Missing transverse energy**

₂₁₄₆ **3.3.8 Overlap removal**

2147 **Chapter 4**

2148 **Probing the top-quark
2149 polarisation in the single-top
2150 *t*-channel production**

2151 The polarisation paper: [https://atlas-glance.cern.ch/atlas/
2152 analysis/papers/details.php?id=13286](https://atlas-glance.cern.ch/atlas/analysis/papers/details.php?id=13286)

2153 **4.1 Introduction**

2154 Apart from the studies of the associated production of a top quark and
2155 a Higgs boson, in this thesis is also presented a simultaneous measurement
2156 of the three components of the top-quark and top-antiquark polarisation
2157 vectors in *t*-channel single-top-quark production.

2158 The single-top-quark production and decay via the Wtb vertex, provides
2159 a unique way to study the coupling between the top-quark, the W boson
2160 and the b quarks. This vertex is studied through the measurement of the
2161 polarisation observables for events produced in pp collisions.

2162 Importance of signal selection: In the polarisation analysis we look at an-
2163 gular distributions. The use of a BDT or NN as it is done on the tHq studies
2164 can introduce bias on this angular distribution. This studies are extremely
2165 sensible to any bias introduced on the angular distributions, therefore a
2166 count and cut method for the signal selection is the safest option.

2167 **4.2 Top quark polarisation observables**

2168 **4.3 Simulated event samples**

2169 **4.4 Object reconstruction**

2170 **4.5 Trigger requirements and event preselection**

2171

2172 **Chapter 5**

2173 **Search for rare associate tHq
2174 production**

2175 **5.1 Introduction**

2176 **Describe the strategy for the $2\ell + 1\tau_{\text{had}}$ analysis**

2177 **5.2 Data and simulated events**

2178 the tH samples were done with MadGraph5_aMC @
2179 NLO++Pythia8+EvtGen

2180 The underlying event is generally done with Pythia8 in ATLAS. In the
2181 tHq samples we used MadGraph5_aMC@ NLO for the calculation of the
2182 matrix element and Pythia8 for the hadronisation and parton showering.
2183 We are also working on alternative samples with Herwig7 as parton shower
2184 generator. **While in section 3 I describe how the events and samples**
2185 **are generally generated and simulated, in this section I should**
2186 **describe what is specifically used in this analysis**

2187 **5.3 Object definition and reconstruction**

2188 **5.4 Signal**

2189 **5.4.1 Signal generation and validation**

2190 **rivet**

2191 **5.4.2 Parton-level truth validation**

2192 **5.4.3 Lepton assignment**

2193 must talk about:

- 2194 • The importance of knowing the lepton origin to define discriminating variables
- 2195
- 2196 • Lepton assignment in the OS scenario
- 2197 • Lepton assignment in the SS scenario
 - 2198 – Labelling the SS with the reconstruction-level and truth-level matching
 - 2199
 - 2200 – ROOT:TMVA BDTG

2201 **5.5 Background estimation**

2202 The main source of background in the $2\ell + 1\tau_{\text{had}}$ channel is due to jets
2203 faking τ_{had} **poner las figuras de oleh**

2204 **5.5.1 Fakes estimation**

2205 **This is taken from the intNote. I have to reorganise and rephe-**
2206 **rase this information** The requirements for the objets defined in section
2207 (ref ref) provide significant suppression of events with jets wrongly selec-
2208 ted as leptons is achieved by asking electrons and muons to pass the tight
2209 requirement that combines `tightLH` ID for leptons and `medium` for muons
2210 and `PLImprovedTight` isolation working points

2211 Similarly, the hadronic taus are required to pass the `medium` require-
2212 ment of the RNN-based discriminator. Even so, the selected data sample
2213 is expected to be contaminated with such type of reducible background. It
2214 is also expected that the simulation of jets faking leptons (electron, muon,
2215 hadronic tau) in ATLAS detector is imprecise or unreliable. Therefore, an
2216 important step of the analysis is to estimate this background in data.

2217 D

2218 **Light lepton fakes** Particles in the Feynman diagram are referred as
2219 ‘prompt’ or ‘real’. Acceptance, quality and isolation requirements are ap-
2220 plied to select these leptons Non-prompt leptons and non-leptonic particles
2221 may satisfy these selection criteria, giving rise to so called ‘non-prompt and
2222 fake’ lepton backgrounds. Fake electrons/muons will not be explicitly dis-
2223 tinguished and are referred as fake leptons. The mis-identified lepton back-
2224 ground arises from heavy-flavour (HF) decay leptons and electrons from
2225 γ -conversions. These leptons are mainly produced in $t\bar{t}$, $Z + \text{jets}$ and tW
2226 events.

2227 The estimation of the fake/non-prompt lepton background is done with
2228 the template fit method or via the matrix method

2229 The fake and real lepton efficiencies (fake/real rates) are defined as the
2230 probabilities of a fake or real electron or muon to pass the nominal elec-
2231 tron/muon requirements. They are given by the tight over loose ratio

2232 - Get some ideas from here: [https://cds.cern.ch/record/1951336/
2233 files/ATLAS-CONF-2014-058.pdf](https://cds.cern.ch/record/1951336/files/ATLAS-CONF-2014-058.pdf)

2234 **Tau fakes** In the analysis channels involving hadronic taus, all meth-
2235 ods used for fake background estimation rely on MC-based templates.
2236 These are splits of simulation according to a type of object mimicking the
2237 lepton of interest. Construction of MC templates related to the electron
2238 and muon fakes is based on `IFFTruthClassifier` tool. **Describe the**
2239 **IFFTruthClassifier**

- 2240 • counting method
2241 • template fit method

2242 The extracted SFs are then applied to the simulated background com-
2243 ponent in the region with taus passing I

2244 5.5.2 Prompt backgrounds

2245 All the processes whose signature is the same as the process of interest
2246 are known as prompt backgrounds as in contrast to the fake or non-prompt
2247 backgrounds described in Section 5.5.1.

2248 5.6 Event selection**2249 5.6.1 Preselection****2250 5.6.2 BDT**

2251 Since a BDT is going to be used for both the lepton assign-
2252 ment al region definition, it may be interesting to describe the
2253 technicalities of the BDT in an appendix

2254 5.6.2.1 Performance**2255 5.6.2.2 Ranking of variables****2256 5.6.2.3 Hyperparameter optimisation****2257 Grid search****2258 Genetic algorithm****2259 5.6.2.4 Negative-weights strategy****2260 5.6.2.5 k-Folding****2261 5.6.3 Signal Region****2262 5.6.4 Control Region****2263 5.7 Systematic uncertainties**

2264 Alternative samples are produced to evaluate the systematics: - Herwig7
2265 -> parton shower - asdfas. -> modelling

2266 **5.7.1 Theoretical uncertainties**

2267 **5.7.2 Modelling uncertainties**

2268 **5.7.3 Experimental uncertainties**

2269 **5.8 Fit results**

2270 **5.8.1 Strategy**

2271 **5.8.2 Fit with Asimov data**

2272 **5.8.2.1 Post-fit**

2273 **5.8.2.2 Pruning**

2274 **5.8.2.3 Nuisance Parameters**

2275 **5.8.2.4 Correlation matrix**

2276 **5.8.2.5 Ranking**

2277 **5.8.3 Fit to data**

2278 **5.8.3.1 Post-fit**

2279 **5.8.3.2 Pruning**

2280 **5.8.3.3 Nuisance Parameters**

2281 **5.8.3.4 Correlation matrix**

2282 **5.8.3.5 Ranking**

2283 **5.8.4 Results**

2284 **5.8.5 Data fit**

2285 **5.9 Combination results**

2286 **Discuss results, compare them with CMS, future perspectives**

²²⁸⁷ **5.10 Conclusions**

2288 Chapter 6

2289 Conclusion

2290

Bibliography

- 2291 ¹Particle Data Group Web Page, *top-quark Mass (Direct Measurements)*,
2292 (2022) <https://pdglive.lbl.gov/DataBlock.action?node=Q007TP> (visited
2293 on 22/01/2022) (cit. on pp. vii, 30).
- 2294 ²Particle Data Group Web Page, *Higgs-boson Mass*, (2022)
2295 <https://pdglive.lbl.gov/DataBlock.action?node=S126M> (visited
2296 on 22/01/2022) (cit. on pp. vii, 39).
- 2297 ³Online Etymology Dictionary, "Physics", (2022)
2298 <https://www.etymonline.com/word/physics> (visited on 20/01/2022)
2299 (cit. on p. 1).
- 2300 ⁴Perseus Digital Library, "fusiko", (2022)
2301 <https://www.perseus.tufts.edu/hopper/text?doc=Perseus:text:1999.04.0057:entry=fusiko/s> (visited on 20/01/2022) (cit. on p. 1).
- 2303 ⁵C Singer, *A Short History of Science to the Nineteenth Century*, p. 35.
2304 (Streeter Press, 2008) (cit. on p. 1).
- 2305 ⁶C. C. W. Taylor et al., *The atomists, leucippus and democritus: fragments: a text and translation with a commentary*, Vol. 5
2306 (University of Toronto Press, 2010) (cit. on p. 1).
- 2308 ⁷O. Leaman, *Key concepts in eastern philosophy* (Routledge, 2002)
2309 (cit. on p. 1).
- 2310 ⁸A. Einstein, *The Foundation of the General Theory of Relativity*,
2311 [Annalen Phys. 49 \(1916\) 769–822](https://doi.org/10.1002/andp.19160490106), edited by J.-P. Hsu and D. Fine
2312 (1916) (cit. on p. 2).
- 2313 ⁹P. A. M. Dirac, *On the theory of quantum mechanics*,
2314 Proceedings of the Royal Society of London. Series A, Containing
2315 Papers of a Mathematical and Physical Character **112** (1926) 661–677
2316 (1926) (cit. on p. 3).
- 2317 ¹⁰R. Aaij et al., *Observation of a narrow pentaquark state, $P_c(4312)^+$, and*
2318 *of two-peak structure of the $P_c(4450)^+$* ,
2319 *Phys. Rev. Lett. 122 (2019) 222001* (2019) (cit. on p. 4).

- ²³²⁰¹¹A. Pich, ‘The Standard model of electroweak interactions’,
 2006 European School of High-Energy Physics (2007) 1
 (cit. on pp. 4, 17).
- ²³²³¹²E. Noether, *Invariante variationsprobleme*, ger,
 Nachrichten von der Gesellschaft der Wissenschaften zu Göttingen,
 Mathematisch-Physikalische Klasse **1918** (1918) 235–257 (1918)
 (cit. on p. 6).
- ²³²⁷¹³C. A. Moura and F. Rossi-Torres, *Searches for Violation of CPT Symmetry and Lorentz Invariance with Astrophysical Neutrinos*,
Universe **8** (2022) 42 (2022) (cit. on p. 10).
- ²³³⁰¹⁴J. S. Bell, *Time reversal in field theory*,
Proc. Roy. Soc. Lond. A **231** (1955) 479–495 (1955) (cit. on p. 10).
- ²³³²¹⁵R. F. Streater and A. S. Wightman,
PCT, spin and statistics, and all that (1989) (cit. on p. 10).
- ²³³⁴¹⁶T. D. Lee and C.-N. Yang,
Question of Parity Conservation in Weak Interactions,
Phys. Rev. **104** (1956) 254–258 (1956) (cit. on p. 10).
- ²³³⁷¹⁷C. S. Wu, E. Ambler, R. W. Hayward, D. D. Hoppes and R. P. Hudson,
Experimental Test of Parity Conservation in β Decay,
Phys. Rev. **105** (1957) 1413–1414 (1957) (cit. on p. 10).
- ²³⁴⁰¹⁸R. L. Garwin, L. M. Lederman and M. Weinrich,
Observations of the failure of conservation of parity and charge conjugation in meson decays: the magnetic moment of the free muon,
Phys. Rev. **105** (4 1957) 1415–1417 (1957) (cit. on p. 10).
- ²³⁴⁴¹⁹J. H. Christenson, J. W. Cronin, V. L. Fitch and R. Turlay,
Evidence for the 2π Decay of the K_2^0 Meson,
Phys. Rev. Lett. **13** (1964) 138–140 (1964) (cit. on p. 11).
- ²³⁴⁷²⁰L.-L. Chau and W.-Y. Keung,
Comments on the Parametrization of the Kobayashi-Maskawa Matrix,
Phys. Rev. Lett. **53** (1984) 1802 (1984) (cit. on p. 11).
- ²³⁵⁰²¹J. Hardy and I. Towner, $|V_{ud}|$ from nuclear β decays,
PoS CKM2016 (2017) 028 (2017) (cit. on p. 12).
- ²³⁵²²²D. Pocanic et al.,
Precise measurement of the $\pi^+ \rightarrow \pi^0 e^+ \nu$ branching ratio,
Phys. Rev. Lett. **93** (2004) 181803 (2004) (cit. on p. 12).
- ²³⁵⁵²³R. E. Shrock and L.-L. Wang,
New, generalized cabibbo fit and application to quark mixing angles in the sequential weinberg-salam model,
Phys. Rev. Lett. **41** (25 1978) 1692–1695 (1978) (cit. on p. 12).

- ²³⁵⁹²⁴N. Cabibbo, E. C. Swallow and R. Winston,
²³⁶⁰*Semileptonic hyperon decays and CKM unitarity,*
²³⁶¹*Phys. Rev. Lett.* **92** (2004) 251803 (2004) (cit. on p. 12).
- ²³⁶²²⁵S. Aoki et al.,
²³⁶³*FLAG Review 2019: Flavour Lattice Averaging Group (FLAG),*
²³⁶⁴*Eur. Phys. J. C* **80** (2020) 113 (2020) (cit. on p. 12).
- ²³⁶⁵²⁶J. P. Lees et al.,
²³⁶⁶*Measurement of the $D^0 \rightarrow \pi^- e^+ \nu_e$ differential decay branching fraction*
²³⁶⁷*as a function of q^2 and study of form factor parameterizations,*
²³⁶⁸*Phys. Rev. D* **91** (2015) 052022 (2015) (cit. on p. 12).
- ²³⁶⁹²⁷D. Besson et al., *Improved measurements of D meson semileptonic*
²³⁷⁰*decays to π and K mesons*, *Phys. Rev. D* **80** (2009) 032005 (2009)
²³⁷¹(cit. on p. 12).
- ²³⁷²²⁸A. Kayis-Topaksu et al.,
²³⁷³*Measurement of topological muonic branching ratios of charmed hadrons*
²³⁷⁴*produced in neutrino-induced charged-current interactions,*
²³⁷⁵*Phys. Lett. B* **626** (2005) 24–34 (2005) (cit. on p. 12).
- ²³⁷⁶²⁹P. del Amo Sanchez et al., *Measurement of the Absolute Branching*
²³⁷⁷*Fractions for $D_s^- \rightarrow \ell^- \bar{\nu}_\ell$ and Extraction of the Decay Constant f_{D_s} ,*
²³⁷⁸*Phys. Rev. D* **82** (2010) 091103, [Erratum: *Phys. Rev. D* 91, 019901
²³⁷⁹(2015)] (2010) (cit. on p. 12).
- ²³⁸⁰³⁰L. Widhalm et al., *Measurement of $D0 \rightarrow \pi l \nu$ ($Kl \nu$) Form*
²³⁸¹*Factors and Absolute Branching Fractions,*
²³⁸²*Phys. Rev. Lett.* **97** (2006) 061804 (2006) (cit. on p. 12).
- ²³⁸³³¹Y. S. Amhis et al.,
²³⁸⁴*Averages of b -hadron, c -hadron, and τ -lepton properties as of 2018,*
²³⁸⁵*Eur. Phys. J. C* **81** (2021) 226 (2021) (cit. on p. 12).
- ²³⁸⁶³²A. Abdesselam et al., *Precise determination of the CKM matrix element*
²³⁸⁷ *$|V_{cb}|$ with $\bar{B}^0 \rightarrow D^{*+} \ell^- \bar{\nu}_\ell$ decays with hadronic tagging at Belle*, (2017)
²³⁸⁸(2017) (cit. on p. 12).
- ²³⁸⁹³³J. P. Lees et al., *Study of $\bar{B} \rightarrow X_u \ell \bar{\nu}$ decays in $B\bar{B}$ events tagged by a*
²³⁹⁰*fully reconstructed B -meson decay and determination of $\|V_{ub}\|$,*
²³⁹¹*Phys. Rev. D* **86** (2012) 032004 (2012) (cit. on p. 12).
- ²³⁹²³⁴B. Colquhoun, R. J. Dowdall, J. Koponen, C. T. H. Davies and
²³⁹³G. P. Lepage,
²³⁹⁴ *$B \rightarrow \pi \ell \nu$ at zero recoil from lattice QCD with physical u/d quarks,*
²³⁹⁵*Phys. Rev. D* **93** (2016) 034502 (2016) (cit. on p. 12).
- ²³⁹⁶³⁵C. W. Bauer, Z. Ligeti and M. E. Luke,
²³⁹⁷*A Model independent determination of $|V(ub)|$,*
²³⁹⁸*Phys. Lett. B* **479** (2000) 395–401 (2000) (cit. on p. 12).

- ²³⁹⁹³⁶R Aaij et al., *Precision measurement of the B_s^0 - \bar{B}_s^0 oscillation frequency with the decay $B_s^0 \rightarrow D_s^- \pi^+$* , New J. Phys. **15** (2013) 053021 (2013) (cit. on p. 12).
- ²⁴⁰⁰
- ²⁴⁰¹
- ²⁴⁰²³⁷M. Misiak et al., *Updated NNLO QCD predictions for the weak radiative B -meson decays*, Phys. Rev. Lett. **114** (2015) 221801 (2015) (cit. on p. 12).
- ²⁴⁰³
- ²⁴⁰⁴
- ²⁴⁰⁵³⁸T. A. Aaltonen et al., *Tevatron Combination of Single-Top-Quark Cross Sections and Determination of the Magnitude of the Cabibbo-Kobayashi-Maskawa Matrix Element \mathbf{V}_{tb}* , Phys. Rev. Lett. **115** (2015) 152003 (2015) (cit. on p. 12).
- ²⁴⁰⁶
- ²⁴⁰⁷
- ²⁴⁰⁸
- ²⁴⁰⁹³⁹V. Khachatryan et al., *Search for the associated production of a Higgs boson with a single top quark in proton-proton collisions at $\sqrt{s} = 8$ TeV*, JHEP **06** (2016) 177 (2016) (cit. on pp. 12, 47).
- ²⁴¹⁰
- ²⁴¹¹
- ²⁴¹²⁴⁰V. M. Abazov et al., *Precision measurement of the ratio $B(t \rightarrow Wb)/B(t \rightarrow Wq)$ and Extraction of V_{tb}* , Phys. Rev. Lett. **107** (2011) 121802 (2011) (cit. on p. 12).
- ²⁴¹³
- ²⁴¹⁴
- ²⁴¹⁵⁴¹P. A. Zyla et al., *Review of Particle Physics*, PTEP **2020** (2020) 083C01 (2020) (cit. on p. 12).
- ²⁴¹⁶
- ²⁴¹⁷⁴²P. Q. Hung, *The Weak Eightfold Way: $SU(3)_W$ unification of the electroweak interactions*, (2021) (2021) (cit. on p. 12).
- ²⁴¹⁸
- ²⁴¹⁹⁴³A. M. Sirunyan et al., *Measurement of the weak mixing angle using the forward-backward asymmetry of Drell-Yan events in pp collisions at 8 TeV*, Eur. Phys. J. C **78** (2018) 701 (2018) (cit. on p. 15).
- ²⁴²⁰
- ²⁴²¹
- ²⁴²²
- ²⁴²³⁴⁴O. W. Greenberg, *Spin and Unitary Spin Independence in a Paraquark Model of Baryons and Mesons*, Phys. Rev. Lett. **13** (1964) 598–602 (1964) (cit. on p. 15).
- ²⁴²⁴
- ²⁴²⁵
- ²⁴²⁶⁴⁵D. D. Ryutov, *Using Plasma Physics to Weigh the Photon*, Plasma Phys. Control. Fusion **49** (2007) B429 (2007) (cit. on p. 20).
- ²⁴²⁷
- ²⁴²⁸⁴⁶F. J. Yndurain, *Limits on the mass of the gluon*, Phys. Lett. B **345** (1995) 524–526 (1995) (cit. on p. 20).
- ²⁴²⁹
- ²⁴³⁰⁴⁷M. Aaboud et al., *Measurement of the W -boson mass in pp collisions at $\sqrt{s} = 7$ TeV with the ATLAS detector*, Eur. Phys. J. C **78** (2018) 110, [Erratum: Eur.Phys.J.C 78, 898 (2018)] (2018) (cit. on p. 20).
- ²⁴³¹
- ²⁴³²
- ²⁴³³
- ²⁴³⁴⁴⁸G. Abbiendi et al., *Precise determination of the Z resonance parameters at LEP: 'Zedometry'*, Eur. Phys. J. C **19** (2001) 587–651 (2001) (cit. on p. 20).
- ²⁴³⁵
- ²⁴³⁶

- ⁴⁹J. Goldstone, A. Salam and S. Weinberg, *Broken Symmetries*, Phys. Rev. **127** (1962) 965–970 (1962) (cit. on p. 21).
- ⁵⁰D. M. Webber et al., *Measurement of the Positive Muon Lifetime and Determination of the Fermi Constant to Part-per-Million Precision*, Phys. Rev. Lett. **106** (2011) 041803 (2011) (cit. on p. 26).
- ⁵¹N. Aghanim et al., *Planck 2018 results. VI. Cosmological parameters*, Astron. Astrophys. **641** (2020) A6, [Erratum: Astron.Astrophys. 652, C4 (2021)] (2020) (cit. on p. 28).
- ⁵²M. Aaboud et al.,
Measurement of the top quark mass in the $t\bar{t} \rightarrow \text{lepton+jets}$ channel from $\sqrt{s} = 8$ TeV ATLAS data and combination with previous results, Eur. Phys. J. C **79** (2019) 290 (2019) (cit. on p. 30).
- ⁵³A. M. Sirunyan et al.,
Measurement of the Jet Mass Distribution and Top Quark Mass in Hadronic Decays of Boosted Top Quarks in pp Collisions at $\sqrt{s} = 13$ TeV, Phys. Rev. Lett. **124** (2020) 202001 (2020) (cit. on p. 30).
- ⁵⁴*Combination of CDF and D0 results on the mass of the top quark using up 9.7 fb^{-1} at the Tevatron*, (2016) (2016) (cit. on p. 30).
- ⁵⁵M. Kobayashi and T. Maskawa,
CP Violation in the Renormalizable Theory of Weak Interaction, Prog. Theor. Phys. **49** (1973) 652–657 (1973) (cit. on p. 30).
- ⁵⁶J. E. Augustin et al.,
Discovery of a Narrow Resonance in e^+e^- Annihilation, Phys. Rev. Lett. **33** (1974) 1406–1408 (1974) (cit. on p. 30).
- ⁵⁷S. W. Herb et al., *Observation of a Dimuon Resonance at 9.5-GeV in 400-GeV Proton-Nucleus Collisions*, Phys. Rev. Lett. **39** (1977) 252–255 (1977) (cit. on p. 30).
- ⁵⁸F. Abe et al., *Observation of top quark production in $\bar{p}p$ collisions*, Phys. Rev. Lett. **74** (1995) 2626–2631 (1995) (cit. on p. 32).
- ⁵⁹S. Abachi et al., *Observation of the top quark*, Phys. Rev. Lett. **74** (1995) 2632–2637 (1995) (cit. on p. 32).
- ⁶⁰M. Czakon and A. Ferroglio, Chinese Physics C () 083104 (cit. on p. 32).
- ⁶¹P. Kant et al., *HatHor for single top-quark production: Updated predictions and uncertainty estimates for single top-quark production in hadronic collisions*, Comput. Phys. Commun. **191** (2015) 74–89 (2015) (cit. on p. 35).

- ²⁴⁷⁴⁶²M. Aliev et al.,
²⁴⁷⁵*HATHOR – HAdronic Top and Heavy quarks crOss section calculatoR*,
²⁴⁷⁶*Comput. Phys. Commun.* **182** (2011) 1034–1046 (2011) (cit. on p. 35).
- ²⁴⁷⁷⁶³J. A. Aguilar-Saavedra,
²⁴⁷⁸*Single top quark production at LHC with anomalous Wtb couplings*,
²⁴⁷⁹*Nucl. Phys. B* **804** (2008) 160–192 (2008) (cit. on p. 36).
- ²⁴⁸⁰⁶⁴J. Butterworth et al., *PDF4LHC recommendations for LHC Run II*,
²⁴⁸¹*J. Phys. G* **43** (2016) 023001 (2016) (cit. on pp. 37, 68).
- ²⁴⁸²⁶⁵A. D. Martin, W. J. Stirling, R. S. Thorne and G. Watt,
²⁴⁸³*Parton distributions for the LHC*, *Eur. Phys. J. C* **63** (2009) 189 (2009)
²⁴⁸⁴(cit. on p. 37).
- ²⁴⁸⁵⁶⁶A. D. Martin, W. J. Stirling, R. S. Thorne and G. Watt,
²⁴⁸⁶*Uncertainties on α_S in global PDF analyses and implications for*
²⁴⁸⁷*predicted hadronic cross sections*, *Eur. Phys. J. C* **64** (2009) 653–680
²⁴⁸⁸(2009) (cit. on p. 37).
- ²⁴⁸⁹⁶⁷H.-L. Lai et al., *New parton distributions for collider physics*,
²⁴⁹⁰*Phys. Rev. D* **82** (2010) 074024 (2010) (cit. on p. 37).
- ²⁴⁹¹⁶⁸R. D. Ball et al., *Parton distributions with QED corrections*,
²⁴⁹²*Nucl. Phys. B* **877** (2013) 290–320 (2013) (cit. on p. 37).
- ²⁴⁹³⁶⁹M. Aaboud et al., *Measurement of the Higgs boson mass in the*
²⁴⁹⁴ *$H \rightarrow ZZ^* \rightarrow 4\ell$ and $H \rightarrow \gamma\gamma$ channels with $\sqrt{s} = 13$ TeV pp collisions*
²⁴⁹⁵*using the ATLAS detector*, *Phys. Lett. B* **784** (2018) 345–366 (2018)
²⁴⁹⁶(cit. on p. 39).
- ²⁴⁹⁷⁷⁰A. M. Sirunyan et al.,
²⁴⁹⁸*A measurement of the Higgs boson mass in the diphoton decay channel*,
²⁴⁹⁹*Phys. Lett. B* **805** (2020) 135425 (2020) (cit. on p. 39).
- ²⁵⁰⁰⁷¹F. Englert and R. Brout,
²⁵⁰¹*Broken symmetry and the mass of gauge vector mesons*,
²⁵⁰²*Phys. Rev. Lett.* **13** (9 1964) 321–323 (1964) (cit. on p. 39).
- ²⁵⁰³⁷²P. W. Higgs, *Broken symmetries and the masses of gauge bosons*,
²⁵⁰⁴*Phys. Rev. Lett.* **13** (16 1964) 508–509 (1964) (cit. on p. 39).
- ²⁵⁰⁵⁷³G. S. Guralnik, C. R. Hagen and T. W. B. Kibble,
²⁵⁰⁶*Global conservation laws and massless particles*,
²⁵⁰⁷*Phys. Rev. Lett.* **13** (20 1964) 585–587 (1964) (cit. on p. 39).
- ²⁵⁰⁸⁷⁴D. de Florian et al., *Handbook of LHC Higgs Cross Sections: 4. Deciphering the Nature of the Higgs Sector*, **2/2017** (2016) (2016)
²⁵⁰⁹(cit. on pp. 41, 42).

- 2511 ⁷⁵G. Aad et al., *Observation of a new particle in the search for the*
2512 *Standard Model Higgs boson with the ATLAS detector at the LHC,*
2513 *Phys. Lett. B* **716** (2012) 1–29 (2012) (cit. on pp. 41, 50).
- 2514 ⁷⁶S. Chatrchyan et al., *Observation of a New Boson at a Mass of 125*
2515 *GeV with the CMS Experiment at the LHC,*
2516 *Phys. Lett. B* **716** (2012) 30–61 (2012) (cit. on pp. 41, 50).
- 2517 ⁷⁷T. Aaltonen et al., *Combined search for the standard model Higgs boson*
2518 *decaying to a bb pair using the full CDF data set,*
2519 *Phys. Rev. Lett.* **109** (2012) 111802 (2012) (cit. on p. 43).
- 2520 ⁷⁸V. M. Abazov et al., *Combined Search for the Standard Model Higgs*
2521 *Boson Decaying to b̄b Using the D0 Run II Data Set,*
2522 *Phys. Rev. Lett.* **109** (2012) 121802 (2012) (cit. on p. 43).
- 2523 ⁷⁹A. Pich, *Electroweak Symmetry Breaking and the Higgs Boson,*
2524 *Acta Phys. Polon. B* **47** (2016) 151, edited by M. Praszalowicz (2016)
2525 (cit. on p. 43).
- 2526 ⁸⁰M. Farina, C. Grojean, F. Maltoni, E. Salvioni and A. Thamm,
2527 *Lifting degeneracies in Higgs couplings using single top production in*
2528 *association with a Higgs boson,* *JHEP* **05** (2013) 022 (2013)
2529 (cit. on pp. 43, 44).
- 2530 ⁸¹S. Biswas, E. Gabrielli and B. Mele, *Single top and Higgs associated*
2531 *production as a probe of the Htt coupling sign at the LHC,*
2532 *JHEP* **01** (2013) 088 (2013) (cit. on p. 43).
- 2533 ⁸²T. Appelquist and M. S. Chanowitz,
2534 *Unitarity Bound on the Scale of Fermion Mass Generation,* *Phys. Rev.*
2535 *Lett.* **59** (1987) 2405, [Erratum: *Phys.Rev.Lett.* 60, 1589 (1988)] (1987)
2536 (cit. on p. 44).
- 2537 ⁸³M. Aaboud et al., *Observation of Higgs boson production in association*
2538 *with a top quark pair at the LHC with the ATLAS detector,*
2539 *Phys. Lett. B* **784** (2018) 173–191 (2018) (cit. on p. 44).
- 2540 ⁸⁴K. Skovpen, ‘First observation of the t̄H process at CMS’,
2541 11th International Workshop on Top Quark Physics (2018)
2542 (cit. on p. 44).
- 2543 ⁸⁵G. Aad et al.,
2544 *Search for H → γγ produced in association with top quarks and*
2545 *constraints on the Yukawa coupling between the top quark and the Higgs*
2546 *boson using data taken at 7 TeV and 8 TeV with the ATLAS detector,*
2547 *Phys. Lett. B* **740** (2015) 222–242 (2015) (cit. on p. 44).

- ²⁵⁴⁸⁸⁶V. Khachatryan et al., *Search for the associated production of the Higgs*
²⁵⁴⁹*boson with a top-quark pair,*
²⁵⁵⁰*JHEP* **09** (2014) 087, [Erratum: *JHEP* 10, 106 (2014)] (2014)
²⁵⁵¹(cit. on p. 44).
- ²⁵⁵²⁸⁷F. Demartin, F. Maltoni, K. Mawatari and M. Zaro,
²⁵⁵³*Higgs production in association with a single top quark at the LHC,*
²⁵⁵⁴*Eur. Phys. J. C* **75** (2015) 267 (2015) (cit. on pp. 45–47).
- ²⁵⁵⁵⁸⁸T. M. P. Tait and C. P. Yuan, *Single top quark production as a window*
²⁵⁵⁶*to physics beyond the standard model,* *Phys. Rev. D* **63** (2000) 014018
²⁵⁵⁷(2000) (cit. on p. 47).
- ²⁵⁵⁸⁸⁹S. Biswas, E. Gabrielli, F. Margaroli and B. Mele,
²⁵⁵⁹*Direct constraints on the top-Higgs coupling from the 8 TeV LHC data,*
²⁵⁶⁰*JHEP* **07** (2013) 073 (2013) (cit. on p. 47).
- ²⁵⁶¹⁹⁰CERN Web Page, *Our Member States*, (2022)
²⁵⁶²[https://home.web.cern.ch/about/who-we-are/our-](https://home.web.cern.ch/about/who-we-are/our-governance/member-states)
²⁵⁶³*governance/member-states* (visited on 11/01/2022) (cit. on p. 50).
- ²⁵⁶⁴⁹¹T. Fazzini, G. Fidecaro, A. W. Merrison, H. Paul and A. V. Tollestrup,
²⁵⁶⁵*Electron decay of the pion,* *Phys. Rev. Lett.* **1** (7 1958) 247–249 (1958)
²⁵⁶⁶(cit. on p. 50).
- ²⁵⁶⁷⁹²F. J. Hasert et al., *Observation of Neutrino Like Interactions Without*
²⁵⁶⁸*Muon Or Electron in the Gargamelle Neutrino Experiment,*
²⁵⁶⁹*Phys. Lett. B* **46** (1973) 138–140 (1973) (cit. on p. 50).
- ²⁵⁷⁰⁹³P. M. Watkins, *Discovery of the w and 2 bosons,*
²⁵⁷¹*Contemporary Physics* **27** (1986) 291–324 (1986) (cit. on p. 50).
- ²⁵⁷²⁹⁴D. Decamp et al.,
²⁵⁷³*Determination of the Number of Light Neutrino Species,*
²⁵⁷⁴*Phys. Lett. B* **231** (1989) 519–529 (1989) (cit. on p. 50).
- ²⁵⁷⁵⁹⁵G. Baur et al., *Production of anti-hydrogen,*
²⁵⁷⁶*Phys. Lett. B* **368** (1996) 251–258 (1996) (cit. on p. 50).
- ²⁵⁷⁷⁹⁶G. D. Barr et al.,
²⁵⁷⁸*A New measurement of direct CP violation in the neutral kaon system,*
²⁵⁷⁹*Phys. Lett. B* **317** (1993) 233–242 (1993) (cit. on p. 50).
- ²⁵⁸⁰⁹⁷V. Fanti et al., *A New measurement of direct CP violation in two pion*
²⁵⁸¹*decays of the neutral kaon,* *Phys. Lett. B* **465** (1999) 335–348 (1999)
²⁵⁸²(cit. on p. 50).
- ²⁵⁸³⁹⁸R. Aaij et al., *Observation of J/ψ Resonances Consistent with*
²⁵⁸⁴*Pentaquark States in $\Lambda_b^0 \rightarrow J/\psi K^- p$ Decays,*
²⁵⁸⁵*Phys. Rev. Lett.* **115** (2015) 072001 (2015) (cit. on p. 50).

- 2586 ⁹⁹S. Maury, *The Antiproton Decelerator: AD,*
2587 *Hyperfine Interact.* **109** (1997) 43–52 (1997) (cit. on p. 50).
- 2588 ¹⁰⁰R. Alemany et al.,
2589 *Summary Report of Physics Beyond Colliders at CERN,*
2590 (2019), edited by J. Jaeckel, M. Lamont and C. Vallée (2019)
2591 (cit. on p. 50).
- 2592 ¹⁰¹R. Catherall et al., *The ISOLDE facility*, *J. Phys. G* **44** (2017) 094002
2593 (2017) (cit. on p. 50).
- 2594 ¹⁰²E. Gschwendtner et al., *AWAKE, The Advanced Proton Driven Plasma*
2595 *Wakefield Acceleration Experiment at CERN,*
2596 *Nucl. Instrum. Meth. A* **829** (2016) 76–82, edited by U. Dorda et al.
2597 (2016) (cit. on p. 50).
- 2598 ¹⁰³M. Aguilar et al.,
2599 *The Alpha Magnetic Spectrometer (AMS) on the International Space*
2600 *Station. I: Results from the test flight on the space shuttle*, *Phys. Rept.*
2601 **366** (2002) 331–405, [Erratum: *Phys.Rept.* 380, 97–98 (2003)] (2002)
2602 (cit. on p. 51).
- 2603 ¹⁰⁴T. J. Berners-Lee and R. Cailliau,
2604 *WorldWideWeb: proposal for a HyperText Project*, tech. rep.,
2605 CERN, 1990 (cit. on p. 51).
- 2606 ¹⁰⁵*CERN Council holds special session on the Large Hadron Collider*
2607 *project*, (1991) 3 p, Issued on 19 December 1991 (1991) (cit. on p. 51).
- 2608 ¹⁰⁶T. S. Pettersson and P Lefèvre,
2609 *The Large Hadron Collider: conceptual design*, tech. rep., 1995
2610 (cit. on pp. 51, 54).
- 2611 ¹⁰⁷S. Myers,
2612 *The LEP Collider, from design to approval and commissioning*,
2613 John Adams' memorial lecture, Delivered at CERN, 26 Nov 1990
2614 (CERN, Geneva, 1991) (cit. on p. 51).
- 2615 ¹⁰⁸B. Müller, J. Schukraft and B. Wyslouch,
2616 *First Results from Pb+Pb Collisions at the LHC*,
2617 *Annual Review of Nuclear and Particle Science* **62** (2012) 361–386
2618 (2012) (cit. on p. 53).
- 2619 ¹⁰⁹CERN Web Page, *The Large Hadron Collider*, (2022)
2620 [https://home.cern/science/accelerators/large-hadron-](https://home.cern/science/accelerators/large-hadron-collider)
2621 [collider](https://home.cern/science/accelerators/large-hadron-collider) (visited on 11/01/2022) (cit. on p. 53).
- 2622 ¹¹⁰R. Steerenberg et al., ‘Operation and performance of the cern large
2623 hadron collider during proton run 2’,
2624 *10th international particle accelerator conference* (2019) MOPMP031
2625 (cit. on p. 53).

- ²⁶²⁶¹¹¹by Rende Steerenberg and A. Schaeffer, *LHC Report: The LHC is full!*,
²⁶²⁷(2018) (2018) (cit. on p. 53).
- ²⁶²⁸¹¹²*8th International Conference on High-Energy Accelerators*,
²⁶²⁹CERN (CERN, Geneva, 1971) (cit. on p. 53).
- ²⁶³⁰¹¹³*LHC Machine*,
²⁶³¹*JINST* **3** (2008) S08001, edited by L. Evans and P. Bryant (2008)
²⁶³²(cit. on pp. 53, 56).
- ²⁶³³¹¹⁴*Radiofrequency cavities*, (2012) (2012) (cit. on p. 54).
- ²⁶³⁴¹¹⁵K. Long et al., *Muon colliders to expand frontiers of particle physics*,
²⁶³⁵*Nature Phys.* **17** (2021) 289–292 (2021) (cit. on p. 55).
- ²⁶³⁶¹¹⁶L Lari, H Gaillard and V Mertens,
²⁶³⁷*Scheduling the installation of the LHC injection lines*, tech. rep.,
²⁶³⁸CERN, 2004 (cit. on p. 56).
- ²⁶³⁹¹¹⁷G. Aad et al.,
²⁶⁴⁰*The ATLAS Experiment at the CERN Large Hadron Collider*,
²⁶⁴¹*JINST* **3** (2008) S08003 (2008) (cit. on pp. 56, 74, 77, 78, 82, 83).
- ²⁶⁴²¹¹⁸S. Chatrchyan et al., *The CMS Experiment at the CERN LHC*,
²⁶⁴³*JINST* **3** (2008) S08004 (2008) (cit. on p. 56).
- ²⁶⁴⁴¹¹⁹A. A. Alves Jr. et al., *The LHCb Detector at the LHC*,
²⁶⁴⁵*JINST* **3** (2008) S08005 (2008) (cit. on p. 57).
- ²⁶⁴⁶¹²⁰K. Aamodt et al., *The ALICE experiment at the CERN LHC*,
²⁶⁴⁷*JINST* **3** (2008) S08002 (2008) (cit. on p. 57).
- ²⁶⁴⁸¹²¹O. Adriani et al.,
²⁶⁴⁹*The LHCf detector at the CERN Large Hadron Collider*,
²⁶⁵⁰*JINST* **3** (2008) S08006 (2008) (cit. on p. 58).
- ²⁶⁵¹¹²²O. Adriani et al.,
²⁶⁵²*Technical design report of the LHCf experiment: Measurement of*
²⁶⁵³*photons and neutral pions in the very forward region of LHC* (2006)
²⁶⁵⁴(cit. on p. 58).
- ²⁶⁵⁵¹²³C. Alpigiani et al., *A Letter of Intent for MATHUSLA: A Dedicated*
²⁶⁵⁶*Displaced Vertex Detector above ATLAS or CMS.*, (2018) (2018)
²⁶⁵⁷(cit. on p. 59).
- ²⁶⁵⁸¹²⁴J. H. Yoo, *The milliQan Experiment: Search for milli-charged Particles*
²⁶⁵⁹*at the LHC*, PoS **ICHEP2018** (2018) 520. 4 p, proceeding for ICHEP
²⁶⁶⁰2018 SEOUL, International Conference on High Energy Physics, 4-11
²⁶⁶¹July 2018, SEOUL, KOREA (2018) (cit. on p. 59).
- ²⁶⁶²¹²⁵A. Ball et al., *Search for millicharged particles in proton-proton*
²⁶⁶³*collisions at $\sqrt{s} = 13$ TeV*, *Phys. Rev. D* **102** (2020) 032002 (2020)
²⁶⁶⁴(cit. on p. 59).

- 2665 ¹²⁶V. A. Mitsou, *The MoEDAL experiment at the LHC: status and results*,
2666 *J. Phys. Conf. Ser.* **873** (2017) 012010, edited by B. Grzadkowski,
2667 J. Kalinowski and M. Krawczyk (2017) (cit. on p. 59).
- 2668 ¹²⁷G. Anelli et al.,
2669 *The TOTEM experiment at the CERN Large Hadron Collider*,
2670 *JINST* **3** (2008) S08007 (2008) (cit. on p. 59).
- 2671 ¹²⁸A. Ariga et al., *Technical Proposal for FASER: ForwArd Search*
2672 *ExpeRiment at the LHC*, (2018) (2018) (cit. on p. 59).
- 2673 ¹²⁹A. Ariga et al.,
2674 *Letter of Intent for FASER: ForwArd Search ExpeRiment at the LHC*,
2675 (2018) (2018) (cit. on p. 59).
- 2676 ¹³⁰*LHC computing Grid. Technical design report*,
2677 (2005), edited by I. Bird et al. (2005) (cit. on p. 59).
- 2678 ¹³¹WLCG Web Page, *Resources*, (2022)
2679 <https://wlcg-public.web.cern.ch/resources> (visited on
2680 31/01/2022) (cit. on p. 60).
- 2681 ¹³²*ATLAS computing: Technical design report*,
2682 (2005), edited by G. Duckeck et al. (2005) (cit. on p. 59).
- 2683 ¹³³WLCG Web Page, *Tier centres*, (2022)
2684 <https://wlcg-public.web.cern.ch/tier-centres> (visited on
2685 31/01/2022) (cit. on pp. 60, 61).
- 2686 ¹³⁴W. Herr and B Muratori, *Concept of luminosity*, (2006) (2006)
2687 (cit. on pp. 62, 63).
- 2688 ¹³⁵A. Hoecker, ‘Physics at the LHC Run-2 and Beyond’,
2689 2016 European School of High-Energy Physics (2016)
2690 (cit. on pp. 63, 64, 69).
- 2691 ¹³⁶M. Aaboud et al., *Luminosity determination in pp collisions at $\sqrt{s} = 8$ TeV using the ATLAS detector at the LHC*,
2692 *Eur. Phys. J. C* **76** (2016) 653 (2016) (cit. on p. 63).
- 2694 ¹³⁷G. Aad et al., *ATLAS data quality operations and performance for*
2695 *2015–2018 data-taking*, *JINST* **15** (2020) P04003 (2020) (cit. on p. 64).
- 2696 ¹³⁸*Luminosity determination in pp collisions at $\sqrt{s} = 13$ TeV using the ATLAS detector at the LHC*, tech. rep., CERN, 2019 (cit. on p. 64).
- 2698 ¹³⁹F. S. Cafagna, *Latest results for Proton-proton Cross Section Measurements with the TOTEM experiment at LHC*,
2699 *PoS ICRC2019* (2021) 207 (2021) (cit. on p. 67).

- 2701 ¹⁴⁰Particle Data Group Web Page,
 2702 *Data files and plots of cross-sections and related quantities for hadrons,*
 2703 (2022) <https://pdg.lbl.gov/2021/hadronic-xsections/> (visited on
 2704 08/02/2022) (cit. on p. 68).
- 2705 ¹⁴¹*Shrek*, 2001 (cit. on p. 71).
- 2706 ¹⁴²*CERN Council holds special session on the Large Hadron Collider*
 2707 *project*, (1991) 3 p, Issued on 19 December 1991 (1991) (cit. on p. 70).
- 2708 ¹⁴³*ATLAS: technical proposal for a general-purpose pp experiment at the*
 2709 *Large Hadron Collider at CERN*, LHC technical proposal
 2710 (CERN, Geneva, 1994) (cit. on p. 70).
- 2711 ¹⁴⁴A. collaboration, ‘First 2.36 TeV Collision Events recorded by the
 2712 ATLAS experiment, December 8th and 14th, 2009’, 2009 (cit. on p. 70).
- 2713 ¹⁴⁵G. Aad et al., *Measurements of the Higgs boson production and decay*
 2714 *rates and constraints on its couplings from a combined ATLAS and*
 2715 *CMS analysis of the LHC pp collision data at $\sqrt{s} = 7$ and 8 TeV*,
 2716 *JHEP* **08** (2016) 045 (2016) (cit. on p. 70).
- 2717 ¹⁴⁶G. Aad et al., *Measurement of the top quark-pair production cross*
 2718 *section with ATLAS in pp collisions at $\sqrt{s} = 7$ TeV*,
 2719 *Eur. Phys. J. C* **71** (2011) 1577 (2011) (cit. on p. 70).
- 2720 ¹⁴⁷G. Aad et al., *Evidence for Electroweak Production of $W^\pm W^\pm jj$ in pp*
 2721 *Collisions at $\sqrt{s} = 8$ TeV with the ATLAS Detector*,
 2722 *Phys. Rev. Lett.* **113** (2014) 141803 (2014) (cit. on p. 70).
- 2723 ¹⁴⁸M. Aaboud et al., *Evidence for light-by-light scattering in heavy-ion*
 2724 *collisions with the ATLAS detector at the LHC*,
 2725 *Nature Phys.* **13** (2017) 852–858 (2017) (cit. on p. 70).
- 2726 ¹⁴⁹M. Aaboud et al., *Search for the standard model Higgs boson produced*
 2727 *in association with top quarks and decaying into a $b\bar{b}$ pair in pp*
 2728 *collisions at $\sqrt{s} = 13$ TeV with the ATLAS detector*,
 2729 *Phys. Rev. D* **97** (2018) 072016 (2018) (cit. on p. 70).
- 2730 ¹⁵⁰M. Aaboud et al., *Observation of $H \rightarrow b\bar{b}$ decays and VH production*
 2731 *with the ATLAS detector*, *Phys. Lett. B* **786** (2018) 59–86 (2018)
 2732 (cit. on p. 70).
- 2733 ¹⁵¹S. Amoroso, *Precision measurements at the LHC*, tech. rep.,
 2734 CERN, 2020 (cit. on p. 70).
- 2735 ¹⁵²H. Pacey, *EW SUSY Production at the LHC*, tech. rep., CERN, 2021
 2736 (cit. on p. 70).
- 2737 ¹⁵³S. Das Bakshi, J. Chakrabortty, C. Englert, M. Spannowsky and
 2738 P. Stylianou, *CP Violation at atlas in effective field theory*,
 2739 *Phys. Rev. D* **103** (5 2021) 055008 (2021) (cit. on p. 70).

- 2740 ¹⁵⁴B. T. Carlson, *Dark Matter searches with the ATLAS detector*, (2020)
2741 (2020) (cit. on p. 72).
- 2742 ¹⁵⁵J. L. Pinfold, *ATLAS and astroparticle physics*, Nucl. Phys. B Proc.
2743 Suppl. **175-176** (2008) 25–32, edited by K. S. Cheng et al. (2008)
2744 (cit. on p. 72).
- 2745 ¹⁵⁶N. D. Brett et al., *Discovery Reach for Black Hole Production*, (2009)
2746 (2009) (cit. on p. 72).
- 2747 ¹⁵⁷*ATLAS inner detector: Technical Design Report*, 1,
2748 Technical design report. ATLAS (CERN, Geneva, 1997) (cit. on p. 74).
- 2749 ¹⁵⁸G. Aad et al.,
2750 *The ATLAS Inner Detector commissioning and calibration*,
2751 Eur. Phys. J. C **70** (2010) 787–821 (2010) (cit. on p. 74).
- 2752 ¹⁵⁹M Capeans et al., *ATLAS Insertable B-Layer Technical Design Report*,
2753 tech. rep., 2010 (cit. on pp. 75, 76).
- 2754 ¹⁶⁰*Technical Design Report for the ATLAS Inner Tracker Pixel Detector*,
2755 tech. rep., CERN, 2017 (cit. on pp. 76, 92).
- 2756 ¹⁶¹ATLAS Experiment Web Page, *Detector and Technology*, (2022)
2757 <https://atlas.cern/discover/detector> (visited on 02/02/2022)
2758 (cit. on pp. 76, 79, 82, 87).
- 2759 ¹⁶²F. Cavallari, *Performance of calorimeters at the LHC*,
2760 Journal of Physics: Conference Series **293** (2011) 012001 (2011)
2761 (cit. on pp. 78, 81, 82).
- 2762 ¹⁶³C. Grupen and B. Shwartz, ‘Calorimetry’, *Particle detectors*, 2nd ed.,
2763 Cambridge Monographs on Particle Physics, Nuclear Physics and
2764 Cosmology (Cambridge University Press, 2008) 230–272 (cit. on p. 80).
- 2765 ¹⁶⁴Particle Data Group Web Page, π^0 Decay Modes, (2022)
2766 <https://pdglive.lbl.gov/DataBlock.action?node=Q007TP> (visited
2767 on 02/02/2022) (cit. on p. 81).
- 2768 ¹⁶⁵A. Tarek Abouelfadl Mohamed, ‘The lhc and the atlas experiment’,
2769 *Measurement of higgs boson production cross sections in the diphoton*
2770 *channel: with the full atlas run-2 data and constraints on anomalous*
2771 *higgs boson interactions*
2772 (Springer International Publishing, Cham, 2020) 61 (cit. on pp. 81, 82).
- 2773 ¹⁶⁶*ATLAS muon spectrometer: Technical design report*, (1997) (1997)
2774 (cit. on p. 83).
- 2775 ¹⁶⁷K. Ishii, *The ATLAS muon spectrometer*, PoS **HEP2001** (2001) 253,
2776 edited by D. o. Horváth, P. Lévai and A. Patkós (2001) (cit. on p. 84).
- 2777 ¹⁶⁸M Livan, *Monitored drift tubes in ATLAS*, tech. rep., CERN, 1996
2778 (cit. on p. 84).

- 2779 169 G. Cattani, *The resistive plate chambers of the ATLAS experiment:*
2780 *performance studies*,
2781 *Journal of Physics: Conference Series* **280** (2011) 012001 (2011)
2782 (cit. on p. 84).

2783 170 K. Nagai, *Thin gap chambers in ATLAS*, *Nucl. Instrum. Meth. A* **384**
2784 (1996) 219–221, edited by F. Ferroni and P. Schlein (1996)
2785 (cit. on p. 85).

2786 171 *ATLAS magnet system: Technical Design Report*, 1,
2787 Technical design report. ATLAS (CERN, Geneva, 1997)
2788 (cit. on pp. 86, 87).

2789 172 *ATLAS high-level trigger, data acquisition and controls: Technical*
2790 *design report*, (2003) (2003) (cit. on pp. 88, 89).

2791 173 G. Aad et al., *Performance of the ATLAS Trigger System in 2010*,
2792 *Eur. Phys. J. C* **72** (2012) 1849 (2012) (cit. on p. 88).

2793 174 *Technical Design Report for the Phase-II Upgrade of the ATLAS TDAQ*
2794 *System*, tech. rep., CERN, 2017 (cit. on pp. 92, 93).

2795 175 G. Aad et al., *The ATLAS Simulation Infrastructure*,
2796 *Eur. Phys. J. C* **70** (2010) 823–874 (2010) (cit. on p. 95).

²⁷⁹⁷ Summary of the results

2798 **Recerca de la producció
2799 associada de bosó de Higgs i
2800 un quark top amb dos leptons i
2801 tau hadrònic a l'estat final**

2802 **1 Marc teòric**

2803 **1.1 El Model Estàndard**

2804 Maybe, I could translate this for the SM summary:
2805 <https://www.quantamagazine.org/a-new-map-of-the-standard-model->
2806 [of-particle-physics-20201022/](https://www.quantamagazine.org/a-new-map-of-the-standard-model-of-particle-physics-20201022/)

2807 **1.2 La física del quark top**

2808 **1.3 La física del bosó de Higgs**

2809 **2 L'experiment ATLAS del LHC al CERN**

2810 **2.1 El gran col·lisionador d'hadrons**

2811 **2.2 El detector ATLAS**

2812 **3 Mesura de la polarització del quark top al
2813 canal-*t***

2814 Mesura d'observables sensibles a la polarització del quark top

2815 **3.1 Selecció d'esdeveniments**

2816 **3.2 Estimació del fons**

2817 **3.3 Fonts d'incertesa**

2818 **3.4 Resultats**

2819 **4 Recerca de processos tH amb un estat final $2\ell + 1\tau_{\text{had}}$**

2821 **4.1 Selecció d'esdeveniments**

2822 **4.2 Estimació del fons**

2823 **4.3 Fonts d'incertesa**

2824 **4.4 Resultats**

2825 **5 Conclusions**

